Comprehensive Evaluation of the Geothermal Resource Potential within the Pyramid Lake Paiute Reservation

Phase III Report

Submitted to:

U.S. Department of Energy
Recovery Act: Geothermal Technologies Program
Validation of Innovative Exploration Technologies
DE-FOA-0000109

Submitted by:

Pyramid Lake Paiute Tribe
P.O. Box 256
Nixon, NV 89424
(775) 574-1050

In collaboration with:
Desert Research Institute
University of Nevada, Reno
Optim Software and Data Solutions
Ehni Enterprises

December, 2013

THIS PAGE INTENTIONALLY LEFT BLANK

CONTENTS

LIST OF FIGURES

LIST OF TABLES

THIS PAGE INTENTIONALLY LEFT BLANK

INTRODUCTION

The Pyramid Lake area lies in the NW part of the Great Basin, which contains the greatest concentration of geothermal fields in the western U.S. (e.g., Faulds *et al.*, 2004). Geothermal exploration efforts within the Pyramid Lake Paiute Tribe (PLPT) Reservation suggest that there are numerous sites that have high geothermal potential. These include Astor Pass area, located in the northwestern portion of the PLPT Reservation, and Emerson Pass, which is located on the northeast portion of PLPT Reservation (see Figure 1). There are other sites within the Reservation that are known to have significant geothermal potential (e.g. Needles Rock), but some of these are sensitive cultural areas that are not suitable for development

This project integrated state-of-the-art exploration technologies with a geologic framework and reservoir modeling to ultimately determine the efficacy of future geothermal production within the PLPT reservation. The information gained during this study should help the PLPT to make informed decisions regarding construction of a geothermal power plant. Additional benefits included the transfer of new technologies and geothermal data to the geothermal industry and it created and/or preserved nearly three dozen jobs accordance with the American Recovery and Reinvestment Act of 2009.

In 1859, the U.S. Commissioner of Indian Affairs reserved for the PLPT 470,000 acres of land surrounding Pyramid Lake. In 1874, President Ulysses S. Grant signed an Executive Order confirming the status of the Tribal Reservation. The PLPT is organized pursuant to the provisions of Section 16 of the Indian Reorganization Act of 1934, 25 U.S.C. Section 267, and is federally recognized by the United States Government. The Tribe operates under the Indian Reorganization Act Constitution and By-Laws approved on January 26, 1936 by the Department of Interior. The PLPT facilitates a Government to Government Relationship with the Federal Government, which recognizes the federal trust responsibilities to the Tribe. Therefore, the Tribe contracts with or receives grants directly from Federal Agencies or the State of Nevada, to provide services to the tribal members and reservation residents. A separate Tribal Corporation is being developed for oversight during the development of geothermal energy with guidance from the Tribal Council. Once the resource is defined, geothermal energy development will be pursued by the PLPT through industry partnerships or internal capital investments.

A variety of tasks were conducted to achieve the above stated objectives. The following are the tasks completed within the project:

1. Permitting
2. Shallow temperature survey
3. Seismic data collection and analysis
4. Fracture stress analysis
5. Phase I reporting

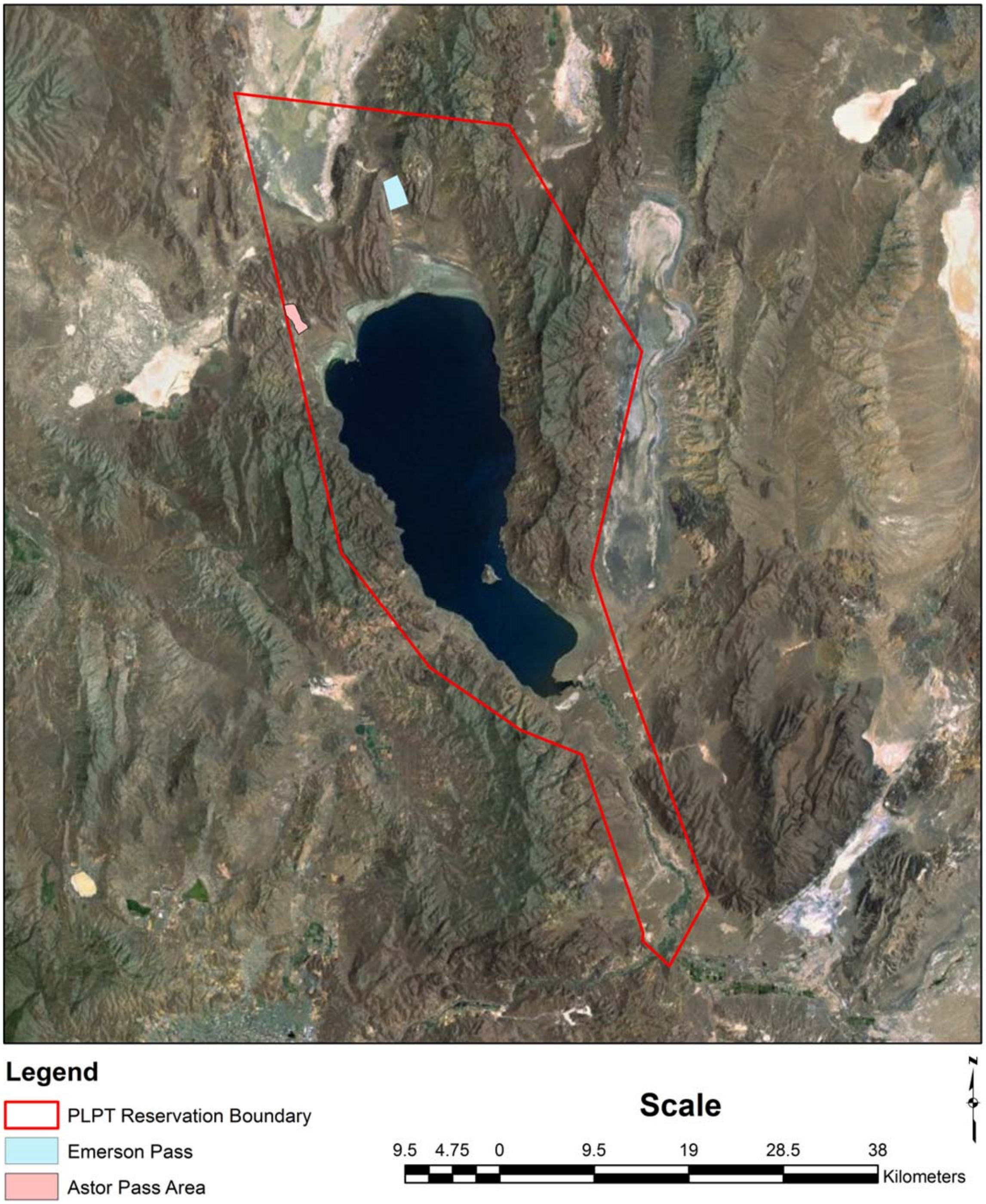

Figure 1. Pyramid Lake Paiute Tribe Reservation showing the location of the Astor Pass and Emerson Pass geothermal areas.

6. Permitting
7. Shallow temperature survey
8. Seismic data collection and analysis
9. Fracture stress analysis
10. Phase I reporting
11. Drilling two new wells
12. Borehole geophysics
13. Phase II reporting
14. Well testing and geochemical analysis
15. Three-dimensional geologic model
16. Three-dimensional reservoir analysis
17. Reservation wide geothermal potential analysis
18. Phase III reporting

Phase I consisted of tasks 1 – 5, Phase II tasks 6 – 8, and Phase III tasks 9 – 13. This report details the results of Phase III tasks. Reports are available for Phase I, and II as separate documents.

ASTOR PASS GEOTHERMAL CHARACTERIZATION

Background

Pyramid Lake, located 45 km north of Reno, Nevada, has been a location of intermittent geothermal exploration since the early 1960s (Garside and Schilling, 1979). At that time, three wells were drilled at the Needle Rocks area, located on the shore of the northern end of the lake. The Needle Rocks area is known for its tufa deposits that extend as high as 90 m above the land surface. Tufa deposits formed where high-calcium groundwater (thermal or nonthermal) discharged into the lake and mixed with dissolved carbon dioxide to precipitate calcium carbonate tufa columns (Coolbaugh *et al.*, 2009). Temperatures as high as 117°C were measured from a well in the Needle Rocks area that continues to flow at high temperature today.

The Astor Pass area is located six kilometers north of Needle Rocks, and is an area that has undergone geothermal exploration in recent years, primarily due to the discovery of a series of northwest-striking faults that cut through Miocene volcanic rocks. The presence of nearby tufa columns and the identification of outcrops of high-temperature alteration minerals kaolinite and halloysite nearby (Coolbaugh, *et al.*, 2006) suggest that hydrothermal fluids may exist below the land surface. An exploration well (APS-1) was drilled in 2007 to a depth of 558 m before circulation was lost and the well was abandoned. Two additional wells were drilled in 2010 and 2011 (APS-2 and APS-3) to depths of 1315 m and 1378 m, respectively. The slotted interval in

APS-3 (the well in which samples were collected and discussed here) is between 1069 and 1376 m below land surface. Drilling logs and samples of cuttings indicate that at APS-3, from the land surface to 113 m are unconsolidated sand, gravel, and clay, and that interbedded Tertiary volcanic rock exists between 113 m and 1272 m below the land surface. Beneath the volcanic rock are intrusive igneous rocks, primarily granodiorite.

Geochemistry

Fluid samples were collected from well APS-3 in early and mid-2011 (Table 1). The May and June samples were collected from the discharge pipe during a well test, which was begun on May 10, 2011, and are therefore representative of the reservoir (the pumping rate was approximately 450 gallons per minute during the 30-day test, and the pump was set 137 m [450 ft] below the land surface). The samples were collected from a discharge tube attached to the wellhead. The sample collected on Feb. 12 was collected during an air-lift procedure of the well. The analyses show that the TDS of the reservoir fluid is ~1600 mg/l, with a pH between 8.6 and 8.9, and is dominantly sodium, chloride, and sulfate. In comparison, water from the Needle Rocks 6 km to the south is controlled by the same ions, though in higher concentrations of sodium and chloride (Coolbaugh *et al.*, 2006, Table 1). The high sodium and chloride concentrations are probably due to evapoconcentration of ancestral Lake Lahontan.

Helium Isotopes

A single helium sample was obtained using a 3/8-inch diameter copper tube attached through a clear, flexible tube to a valve located toward the bottom of the main discharge pipe (10 inch diameter) from the well. The discharge pipe was approximately 2/3 full during discharge, and the sample valve was located approximately 30 meters from the end of the discharge pipe; in other words, the gas phase of the upper 1/3 of the pipe was most likely entirely steam from the reservoir and not atmospheric air entering from the end of the discharge pipe (located approximately 30 meters downstream). Although there were gas bubbles in the copper tube, these were most likely to be from outgassing of the fluid as the pressure dropped during the fluid rise in the wellbore, and are therefore representative of the subsurface conditions and are not atmospheric contamination. Fluid from the discharge pipe flowed through the copper pipe for approximately 10 minutes; a second flexible tube with a valve was attached to the downstream end of the copper tube to control flow and to eliminate bubbles in the flexible tubes. The copper tube was repeatedly tapped with a hard object to dislodge entrapped air bubbles located on the tube. When we were satisfied that the bubbles present were from outgassing, and not remnant atmospheric air, a pinch clamp located on the downstream end of the copper tube was tightened, followed by a similar clamp at the upstream end of the tube. The sample was then shipped to the Dissolved Gas Lab at the University of Utah for analysis of ^{3}He/^{4}He, as well as tritium. The dissolved gas was extracted from the copper tube under high vacuum and analyzed using a magnetic sector field mass spectrometer.

Table 1. Major ion chemistry (in mg/l unless otherwise noted) from well APS-3.

Parameter	Sample Date		
	2/12/2011	5/11/2011	6/10/2011
Temp, °C		90	90
SiO_2 – unfiltered	58	63.4	68.4
SiO_2 – filtered[1]			66.6
Cl	580	564	557
F	3.0		
SO_4	350	356	363
NO_3-N		<0.01	<0.01
HCO_3	17	2.3	2.3
CO_3		12.6	12.1
As	<0.005		
B	2.4		
Ca	60	65.5	64.4
CO_3	8.0	<0.1	<0.1
Cu	<0.05		
Fe	0.71		
Mg	0.04	0.1	0.1
Mn	0.048		
pH, standard units	8.57	8.9	8.9
K	13	11.6	11.0
Na	430	462	454
Total Alkalinity	27		
TDS	1600	1592	1587
EC, µS/cm		2500	2520
Charge, anions/cat		1.004	1.02
^{4}He, cc STP/g H_2O			8.67×10^{-6}
R/Ra[2]			0.28
Ar, ccSTP/g			2.5×10^{-4}
Ne, ccSTP/g			1.31×10^{-7}
Kr, ccSTP/g			6.77×10^{-8}
Xe, ccSTP/g			1.00×10^{-8}
Tritium, TU			0.09
$\delta^{18}O_{vsmow}$, ‰		-14.5	-14.5
δD_{vsmow}, ‰		-118	-118
$\delta^{13}C$, ‰			-4.6
^{14}C, pmc[3]			24.3

[1] Sample was passed through a 0.45 micron filter; both unfiltered and filtered samples underwent 1/10 field dilution.

[2] R/Ra is the ratio of $^3He/^4He$ in the sample to $^3He/^4He$ in air.

[3] percent modern carbon.

The ratio $^3He/^4He$ (also referred to as *R*) and the concentration of ^4He in a sample can be used to infer the source of fluid in a reservoir. Helium-4 is derived from radioactive decay of crustal uranium and thorium, while ^3He is derived from the mantle and from the radioactive decay of tritium. The ratio $^3He/^4He$ in the atmosphere is approximately 1.38 x 10^{-6}; often ratios are normalized to this value such that $R/Ra = 1$, such that R/Ra of recharge water is ~1. A noble gas sample from APS-3 resulted in a ^4He value of 8.67 x 10^{-6} cm^3 ^4He stp/g distilled water (2.32 x 10^{14} atoms ^4He /g distilled water). This can be compared to the concentration of ^4He in the atmosphere, and hence, recharge water. The solubility of helium at an elevation 2000 m above sea level (an estimate of recharge elevation), and between 10°C and 20°C (an estimated annual temperature of recharge), is ~10^{12} atoms He/g water (Mazor, 1991). The sample, therefore, contains over 100 times more ^4He than the atmosphere, suggesting that the excess helium is derived from the crust and/or mantle. A simple mass balance can estimate what percentage, if any, of the helium is derived from the mantle (Kennedy and van Soest, 2006). A typical value of $^3He/^4He$, or *R*, for the crust is 0.02*Ra*, while *R* for the mantle is between 8*Ra* and 9*Ra*. *R/Ra* for the sample from APS-3 is 0.28 (Figure 2). The mass balance calculation shows that perhaps 3.3 percent of the helium in the sample is derived from the mantle. The implication is that the reservoir may be heated by this same small percent of mantle derived heat, but that most of the heat is derived by deep circulating groundwater not in contact with any mantle-derived fluids, as are most of the geothermal systems in the Great Basin.

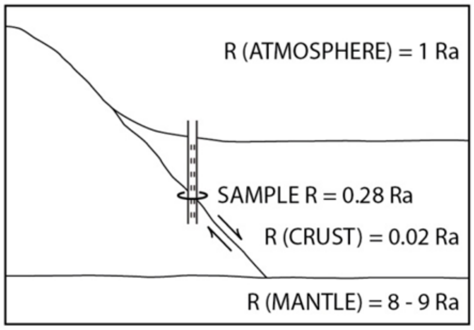

Figure 2. Distribution of *R/Ra* (=$^3He/^4He$) among the atmosphere, crust, and mantle.

^{14}C Age

Carbon-14 is a natural tracer that is used to date groundwater that has recharged within the last 30,000 to 40,000 years. Dissolved inorganic carbon in groundwater is derived primarily from two sources: (1) biogenic production of CO2 from the decay of plant and animal matter, and (2) dissolution of carbonate-containing minerals (Clarke and Fritz, 1997).

An estimate of the time since recharge ("age") of the reservoir fluid can be determined knowing the values of ^{14}C concentration (in percent modern carbon) and $\delta^{13}C$ of the reservoir fluid. The analysis assumes that, except for radioactive decay, the system is closed, and that the initial ^{14}C value is known. An analysis for both ^{14}C concentration and δ^{13}C (also required in the calculation) was done for a sample from APS-3 using the accelerator mass spectrometry facility on a filtered water sample at the University of Arizona. Isotopic ratios are reported in standard del (δ) notation as per mil (‰) deviations from the PDB standard (Faure, 1977). The δ^{13}C and ^{14}C values are -4.6 ‰ and 24.3 pmc, respectively. Age is determined by solving a differential equation for mass balance with radioactive decay of an element (Clark and Fritz, 1997),

$$t_{age} = -8270 \ln \frac{^{14}\mathrm{C}_{\mathrm{sample}}}{f\,^{14}\mathrm{C}_{\mathrm{init}}} \tag{1}$$

where ^{14}C is the concentration of the sample (as pmc) and the initial concentration (assumed here as 100 pmc), and *f* is a dilution factor that accounts for mixing with waters of different ^{14}C composition, calcite and dolomite dissolution, exchange of ^{14}C with reservoir rocks, and matrix diffusion. Many models exist for the determination of *f* (see the review by Fontes and Garnier, 1979), but several of them reduce to the following for systems with limited data,

$$f = \frac{\delta^{13}\mathrm{C}_{\mathrm{dic}} - \delta^{13}\mathrm{C}_{\mathrm{carb}}}{\delta^{13}\mathrm{C}_{\mathrm{soil\text{-}CO2}} - \delta^{13}\mathrm{C}_{\mathrm{carb}}} \tag{2}$$

Here, $\delta^{13}\mathrm{C}_{\mathrm{dic}}$ is the per mil value of the carbon-13 of the dissolved inorganic carbon in the sample, $\delta^{13}\mathrm{C}_{\mathrm{carb}}$ is the per mil value of carbonate minerals dissolved in the water, and $\delta^{13}\mathrm{C}_{\mathrm{soil\text{-}CO2}}$ is the per mil value of the soil-gas CO$_2$, which is the primary control on ^{13}C concentration (i.e., the carbon signal of precipitation is masked by reactions in the soil zone). The value of $\delta^{13}\mathrm{C}_{\mathrm{carb}}$ is usually taken as 0, but $\delta^{13}\mathrm{C}_{\mathrm{soil\text{-}CO2}}$ is more difficult to measure, due to the nature of the reactions in the soil zone. Thorstenson *et al.* (1998) measured values of $\delta^{13}\mathrm{C}_{\mathrm{soil\text{-}CO2}}$ at Yucca Mountain and determined a mean of -16 ‰. These values result in f=0.29, and a water "age" of 1500 years.

Tritium

Natural meteoric levels of tritium are 5 tritium units (TU); one TU is equivalent to five tritium atoms in 10^{18} hydrogen atoms, or 3.2 pCi/L (pico Curies per liter; a Curie is one disintegration per second). Natural production of tritium is very small when compared to the amount of tritium released during atmospheric testing of nuclear weapons, which ceased in 1963. At that time, tritium levels in groundwater were measured as high as 2200 TU.

Tritium was collected in 500-ml glass bottles with airtight caps to prevent evaporation and analyzed at the Dissolved and Noble Gas Lab at the University of Utah. This value of age is corroborated by a measurement of tritium in the APS-3 sample of 0.09 ±0.05 TU. The near absence of tritium in the sample indicates that the water was recharged more than sixty years ago. It must be stressed, however, that the age calculation is non-hydrodynamic: it assumes piston flow through a uniform-permeability reservoir with perfect mixing, and without diffusion, dispersion, or the presence of stagnant zones (Neretnieks, 1981; Sanford, 1997; Bethke and Johnson, 2002).

Stable Isotopes of Hydrogen and Oxygen

Stable isotopes were collected in glass bottles with airtight Teflon caps to prevent evaporation. The stable isotope ratios were measured on a mass spectrometer at the Nevada Stable Isotope Lab in the Geological Sciences Department at the University of Nevada, Reno. Isotopic ratios are reported in standard del (δ) notation as per mil (‰) deviations from the Standard Mean Ocean Water (SMOW) reference standard (Faure, 1977).

Two analyses of oxygen-18 and deuterium sampled one month apart gave the same values for both isotopes, $\delta^{18}O$ = -118 and δD = -14.5 (Figure 3). Also shown in the plot are two samples from a nearby thermal gradient well (NBG#3) 68 m (224 feet) in depth, one sample from a flowing well at the Needle Rocks area, and two samples from the San Emidio springs north of Astor Pass. All samples show the characteristic $\delta^{18}O$ shift, due to an oxygen exchange reaction with the host rock that is characteristic of high-temperature subsurface fluids. The greater shift for the Needle Rocks sample is characteristic of a much hotter and reactive system,

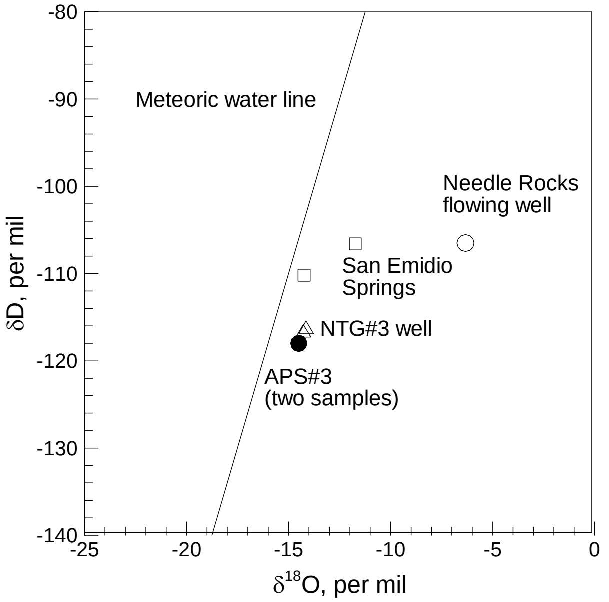

Figure 3. Relation between deuterium and oxygen-18 for two samples (the points are superimposed) from APS#3. Also shown is a single sample from a flowing well located in the Needle Rocks area 6-km south (on the shore of Pyramid Lake), two samples from a temperature gradient hole nearby APS#3, and two additional analyses from springs in the San Emidio Desert north of Astor Pass. Needle Rocks, NTG#3, and San Emidio springs date are from the Nevada Bureau of Mines and Geology *Great Basin Groundwater Geochemical Database*). MWL is the meteoric water line, $\delta D = 8\delta^{18}O + 10$.

although at the time the sample was collected the temperature of discharge was 66°C; the Na-K-Ca geothermometer (discussed below) gives a reservoir temperature of 214°C (NBMG Geothermal Database, accessed June 15, 2013).

Deuterium in the water molecule is unresponsive to temperature-dependent fractionation, and therefore can be used to delineate origins of recharge and subsurface fluid flow paths. The data are too limited to make anything other than tenuous statements that require additional data and interpretation to be of use. Deuterium and $\delta^{18}O$ ratios are nearly the same in the Astor Pass well (APS#3) and the much shallower thermal gradient well (NTG#3) sampled in 2005, highly suggestive that reservoir fluids are vertically well mixed in the Astor Pass area. This is consistent with the observation that the shallow water supply well located 0.5 mile from APS#3 might be connected to the deeper reservoir fluids because the water supply well showed a slight drawdown during the 30-day aquifer test. With respect to the flowing well at the Needle Rocks area, the less depleted δD (by 10%) water from the Needle Rocks suggests that either the two waters that they are not derived from the same source or that they are highly mixed. Additional sampling in the vicinity, including springs, is needed to make more definitive statements.

Reservoir Temperature

Wellhead temperatures can underestimate reservoir temperatures primarily for two reasons: (1) hotter fluids within the reservoir may mix with cooler fluids in uncased sections of the reservoir, and (2) fluid rising through the well can cool conductively. Geothermometry is used to estimate reservoir temperatures primarily by exploiting solubility relationships of silica dissolved in the reservoir fluid (silica geothermometry) and temperature-dependent equilibrium constants (cation geothermometry). Geothermometry relies primarily on four assumptions: that (1) the chemical reactions used in the calculations are temperature dependent, (2) the reactions are at thermodynamic equilibrium, (3) there is no re-equilibration while fluid rises to the surface, and (4) there is no mixing of geothermal water with cooler, shallower water.

Discharge temperature throughout duration of well test was 90°C. A quartz geothermometer that estimates reservoir temperature without steam loss and is valid 20 to 330°C (Fournier, 1982),

$$T^{\circ}C = K_1 + K_2 C + K_3 C^2 + K_4 C^3 + K_5 \log C \tag{3}$$

where K_1= -4.2198 x 10^1, K_2= 2.8831 x 10^{-1}, K_3 = -3.6686 x 10^{-4}, K_4= 3.1665 x 10^{-7}, and K_5= 7.7034 x 10^1, and where silica concentration C is in mg/kg, gives a reservoir temperature of 115°C. The assumptions required for silica geothermometry are probably met for its application; i.e., the silica content for the pressure-temperature conditions is in equilibrium in the reservoir, the reservoir fluid is unable to re-equilibrate as it rises to the surface in the well (reaction constants for silica are on the orders of hours to days while the circulation [lag] time in the well at 450 gpm [1.7 m^3/min] is less than 45 minutes), and there is no mixing of geothermal water with cooler subsurface water (the upper 1069 meters of formation is cased off). The geothermometer assumes silica is saturated in the reservoir. To check this, we collected two samples at 1/10 field dilution within minutes of each other, the difference being that one was passed through a 0.45 micron filter. The SiO_2 concentration is within a few percent for both samples, suggesting that there may not be precipitable SiO_2 in the reservoir and that silica is close to saturation. The total dissolved solids content of the samples was low, approximately 1600 mg/l, so that corrections for changes in enthalpy due to high TDS are unwarranted. Below 300°C, fluid pressure and dissolved solutes have little effect on silica solubility.

The problem with silica geothermometry is that silica solubility is dependent upon the mineral form in which it exists. If well-crystallized quartz controls solubility, then the quartz geothermometer may accurately estimate reservoir temperature. If, however, silica solubility is controlled by much finer-grained (and higher surface energy) chalcedony, the reservoir temperature is calculated to be lower due to the higher solubility of the chalcedony. The chalcedony geothermometer,

$$T^{\circ}C = \frac{1032}{4.69 - \log C} / -273.15 \tag{4}$$

gives a reservoir temperature of 86°C, slightly lower than the temperature at the wellhead.

In contrast, cation geothermometers are based on exchange reactions with temperature-dependent equilibrium constants. The main assumption is that activities of the dissolved species are about equal to the molal concentrations in aqueous solutions (a good assumption since the TDS of the fluids at Astor Pass is close to 1600 mg/L). The widely used Na-K-Ca geothermometer, where concentrations are in mol/L,

$$T^{\circ}C = \frac{1647}{\log(\mathrm{Na}/\mathrm{K}) + 4/3(\log \mathrm{Ca}) + 2.06} - 273.15 \tag{5}$$

gives a reservoir temperature of 155°C.

More important than determining the correct geothermometer is to determine if the error associated with chemical geothermometry, which assumes that there the reactant minerals are initially in equilibrium (so that the geothermometer can be "set"), and that there is minimal mixing or re-equilibration of water as it travels to the surface (Fournier, 1977). In a numerical study of chemical geothermometry, Ferguson *et al.* (2009) determined that maximum in situ temperatures could be under-predicted by up to 30 percent due to mixing of fluids entering a fault at depth.

Discussion and Summary

Analysis of three water samples collected from a single well located in the Astor Pass area indicate that the reservoir fluids are of a sodium, chloride, sulfate type, with a pH between 8.6 and 8.9. These three elements are absent in the fractured volcanic reservoir rocks, and are probably derived from dissolution of sodium chloride and sulfate minerals by precipitation recharging through areas that were once the bed of Lake Lahontan. Analysis of stable isotopes shows the typical shift in ^{18}O that signals oxygen-exchange reactions at high temperatures. Differences in deuterium per mil values show little relationship between reservoir fluids at Astor Pass and a flowing well 6-km south on the shore of Pyramid Lake. Carbon isotopes suggest that the "age" of the reservoir fluids is less than 1500 year old, but this value is suspect due to assumptions that may be poorly met. There is essentially no tritium in the reservoir fluid, meaning that little or no component of the reservoir fluids were recharged less than 60 years ago. As indicated by analysis of helium isotopes, the system is most certainly heated by deep circulation of groundwater, as most systems in the Basin and Range, but that there may a slight component (3.5%) of mantle-derived helium. Geothermometry suggests are reservoir temperature in the area <115°C. The reservoir appears to be vertically well mixed, as deuterium ratios from APS#3 are similar to the value for a sample obtained from a much shallower nearby thermal gradient hole.

SLIP AND DILATION TENDENCY

Fracture permeability is favored along fault segments that are critically stressed and at jogs, intersections and ramps along fault zones, where stresses are concentrated. As such, critically stressed fault segments have a relatively higher likelihood of hosting permeability and acting as conduits for geothermal fluid flow (Morris *et al.*, 1996; Sibson, 1994; Sibson, 1996). The tendency of a fault segment to slip (Morris *et al.*, 1996) or to dilate (Ferrill *et al.*, 1999) provides an indication of which faults or fault segments are critically stressed and therefore the most likely to transmit geothermal fluids. The slip tendency (T_s) of a surface is defined by the ratio of shear stress (τ) to normal stress (σ_n) on that surface:

$$T_s = \tau / \sigma_n \qquad \text{(Morris } et\ al.\text{, 1996)} \qquad (6)$$

Dilation tendency (T_d) is defined by the all the stresses acting normal to a given surface:

$$T_d = (\sigma_1 - \sigma_n) / (\sigma_1 - \sigma_3) \qquad \text{(Ferrill } et\ al.\text{, 1999)} \qquad (7)$$

Slip and dilation tendency on the modeled Astor Pass fault surfaces were calculated using 3DStress (Southwest Research Institute).

Preliminary stress field calculations based on borehole breakouts and drilling induced tensile fractures at Astor Pass indicate that the minimum horizontal stress (shmin) direction is oriented 093. This is consistent with stress field calculations based on fault kinematic data at Emerson Pass (Anderson, 2013). Additionally the magnitudes of the maximum horizontal stress (shmax) and the vertical stress (sv) are very close to one another, indicating that Pyramid Lake Paiute Reservation lies in a stress regime that is transitional between predominantly normal faulting (sv>shmax) and strike-slip faulting (sv<shmax) (Mayhew, 2013; D. McNamara written communicaton). This result is consistent with the location of the Pyramid Lake Paiute Reservation at the margin between the Basin and Range (west-northwest directed extension) and the Walker Lane (north-northwest directed dextral shear) tectonic regimes.

Whether the vertical stress (sv) magnitude is larger (a normal faulting stress regime) or the maximum horizontal stress (shmax) magnitude is larger (a strike slip faulting stress regime) has a profound effect on which fault segments will be critically stressed for slip. Under the stress conditions measured at Astor Pass and a strike-slip faulting stress regime, the north-northwest striking and near-vertical fault segments on the Pyramid Lake Paiute Reservation have the highest tendency to slip (Figure 4) and therefore generate and preserve fracture permeability. In a normal faulting stress regime, however, the north to north-northeast striking, ~60º dipping fault segments have the highest tendency to slip (Figure 5).

Whether sv or shmax has a slightly larger magnitude has very little effect on dilation tendency, which is controlled by the stresses acting normal to fault planes. Under both normal faulting and strike-slip faulting stress regimes, the north-striking, near-vertical fault segments on the Pyramid Lake Paiute Reservation have the highest dilation tendency (Figure 6).

GEOLOGIC MODEL

The Astor Pass 3D geologic model was built using EarthVision (by Dynamic Graphics Inc., Alameda, CA) utilizing methods similar to that described by Jolie *et al.* (2012) and Moeck *et al.* (2009), and Siler *et al.* (2012). The model was constructed based on 1:24,000 scale geologic maps and cross sections (Vice, 2008; Mayhew, 2013), lithologic analysis of ~9000 ft of well cuttings (Mayhew, 2013), and interpretation of 16 seismic reflection profiles, reprocessed with advanced techniques specifically designed for fault imaging (Eisses *et al.*, 2011; Louie *et al.*, 2011).

Faults were modeled based on mapped surface traces, seismic reflection interpretations, geologic cross-sections, and orientation of slickenlines, as well as the presence of fault gouge in the well cuttings and the depths of major zones of lost circulation during drilling of the three wells. Stratigraphic horizons were modeled based on geologic mapping and cross-sections (Vice, 2008) and lithologic units defined from analysis of well cuttings (Mayhew, 2013). All three wells lie in close proximity, limiting the amount of subsurface stratigraphic control throughout the area. As a result the basaltic, basaltic andesitic, and volcaniclastic units of the middle Miocene lower Pyramid sequence and Mesozoic basement rocks were assumed to retain thickness throughout the modeled area, in agreement with previous work in the Pyramid Lake region and in the Pyramid sequence rocks (e.g. Bonham and Papke, 1969; Vice, 2008). Three distinct rhyolitic bodies were interpreted from well cuttings. The modeled extents of these rhyolites were based on the surface extents of rhyolitic rocks mapped in the Astor Pass area (Figure 7 Vice, 2008).

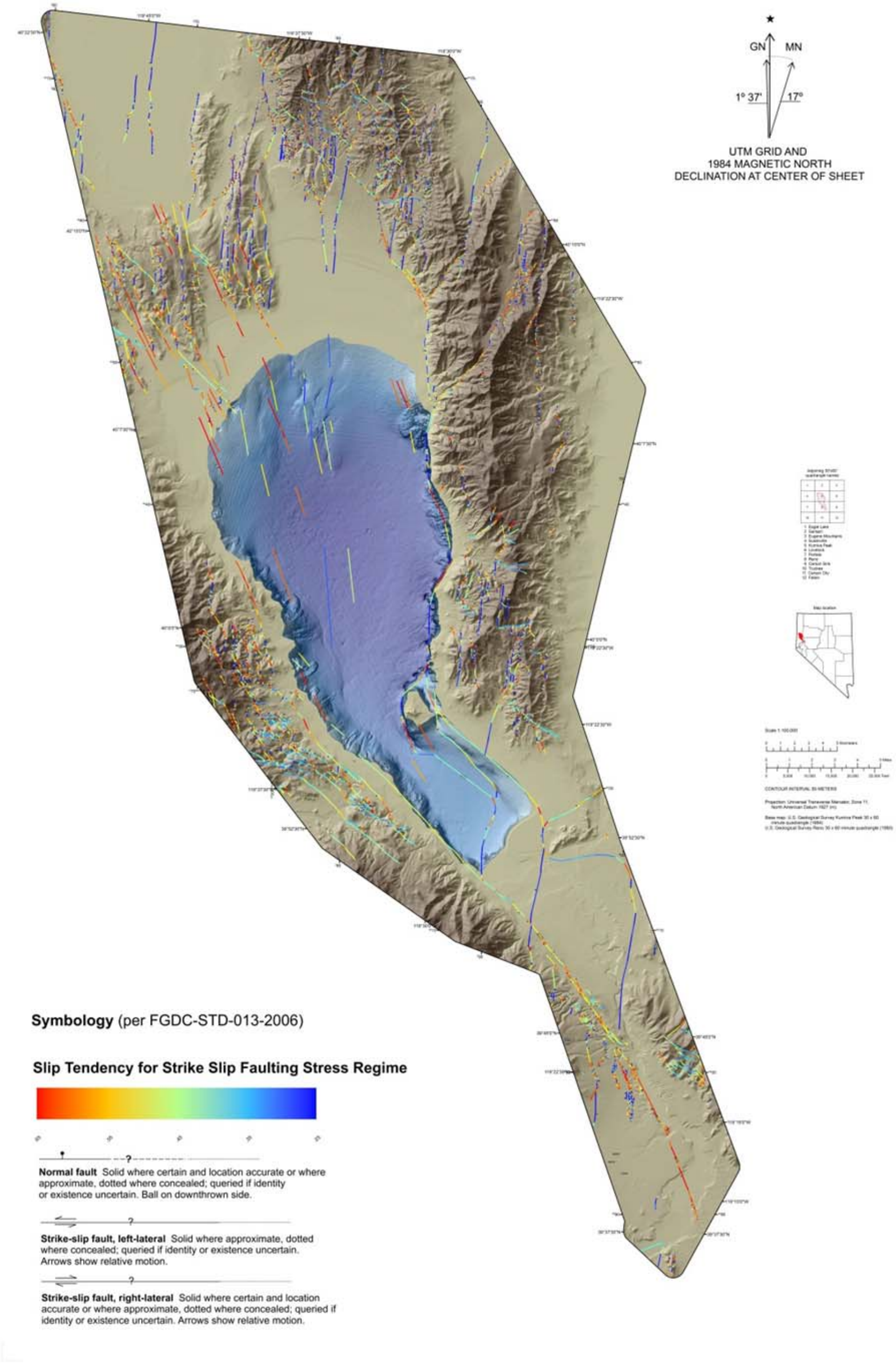

Figure 4. Map of the slip tendency of faults on the Pyramid Lake Paiute Reservation under a strike-slip faulting stress regime.

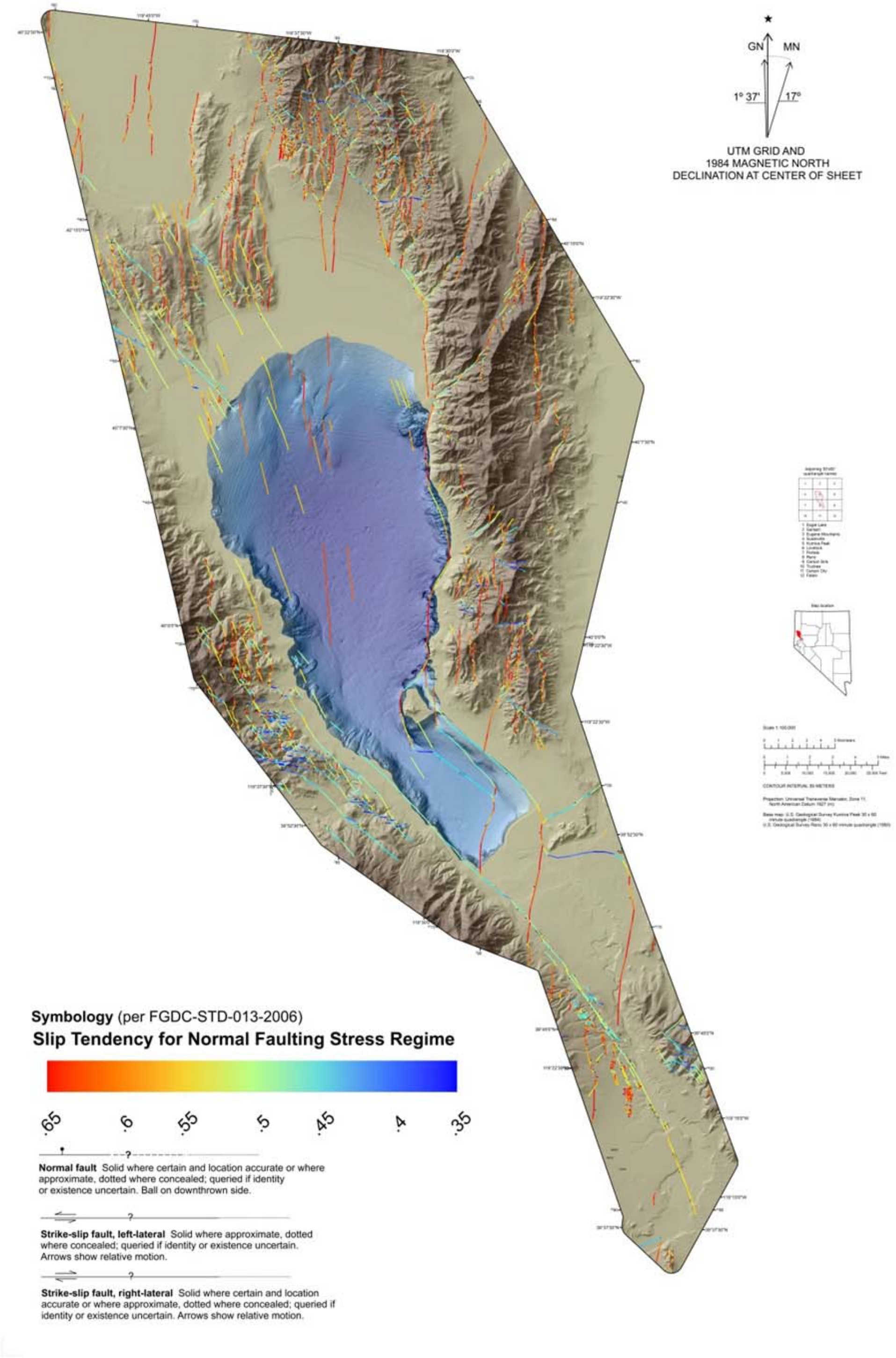

Figure 5. Map of the slip tendency of faults on the Pyramid Lake Paiute Reservation under a normal faulting stress regime.

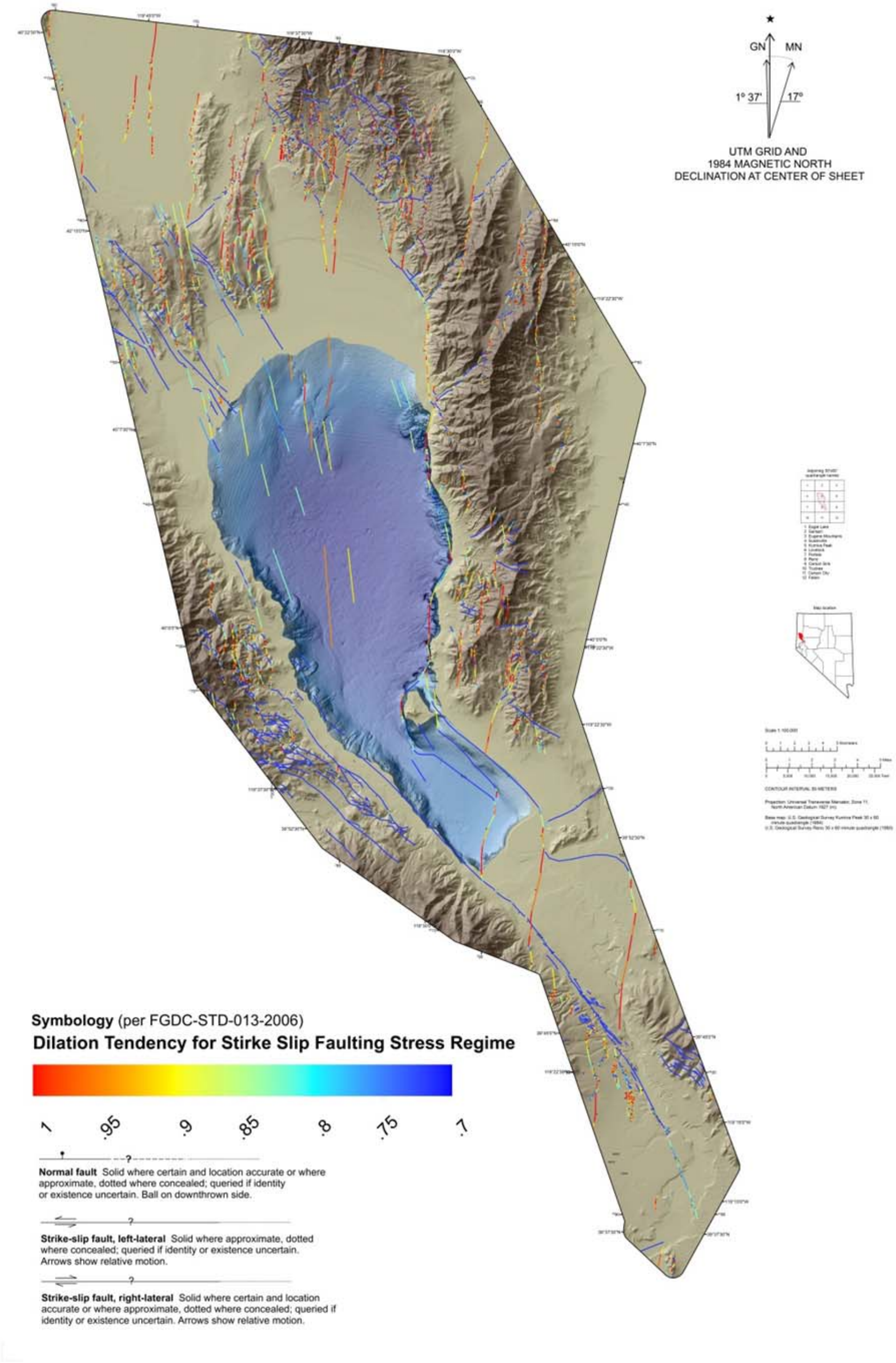

Figure 6. Map of the dilation tendency of faults on the Pyramid Lake Paiute Reservation under a strike-slip faulting stress regime.

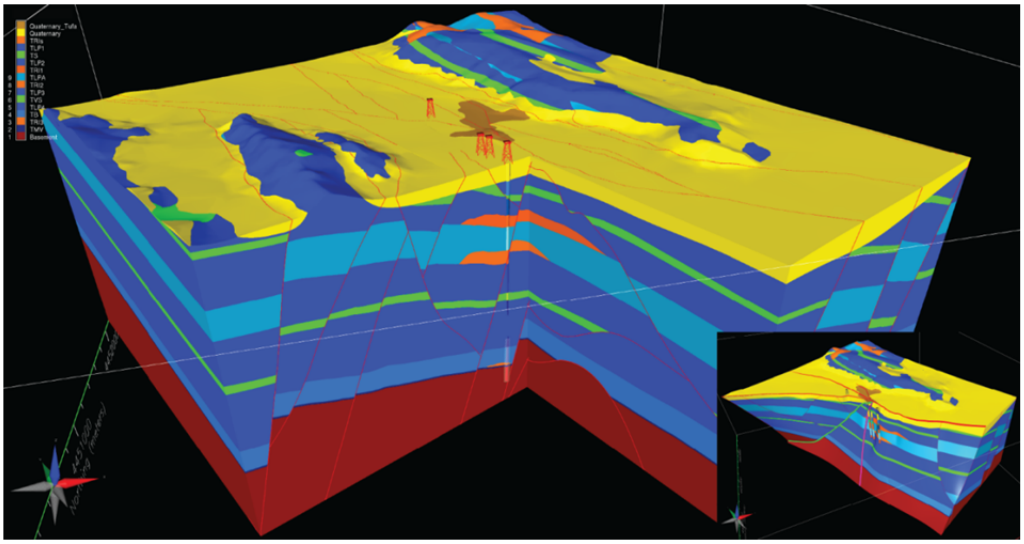

Figure 7. The Astor Pass 3D geologic model. The model is sliced at APS #3. Lithology is based on analysis of drill cuttings (Mayhew, 2013) and is shown on the well path. Gray sleeve on the well path indicates location of the slotted liner, where the well is open to flow from the formation. Look direction is north. Inset shows the discrete fault intersections interpreted by Siler *et al.* (2012), Vice *et al.* (2007) and Vice (2008) as controlling structures of the geothermal system, dipping moderately northwest (green) and steeply southwest (pink). Look direction is northeast.

The 3D geologic model of the Astor Pass geothermal prospect consists of 19 fault planes and 16 stratigraphic units. The Astor Pass graben is bounded by steeply west-dipping, anastomosing normal faults on the east side and one steeply east-dipping normal fault on the west side. The stratigraphy consists of Quaternary alluvium and Pleistocene tufa unconformably overlying a ~1 km-thick section of the middle Miocene lower Pyramid sequence. The lower Pyramid sequence at Astor Pass consists primarily of basalt to basaltic andesite lava flows with interbedded volcaniclastic and sedimentary intervals and local rhyolitic bodies (Mayhew, 2013). The lower Pyramid sequence unconformably overlies metamorphosed Mesozoic mafic lava flows and granodiorite intrusive rocks (Bonham and Papke, 1969; Vice *et al.*, 2007; Vice, 2008; Mayhew, 2013). The predominant west-dipping fault set accommodated moderate (~20-40°) east-tilting of fault blocks in the area (Figure 7).

A steeply northeast-dipping dextral-normal fault zone and a steeply west-dipping normal fault zone intersect on the surface near the Pleistocene tufa deposits. This fault intersection was originally interpreted as the primary controlling structural control of the geothermal system (Vice *et al.*, 2007; Vice, 2008; Faulds *et al.*, 2011). Our analysis is consistent with this interpretation. 3D modeling has revealed that, in addition to these two fault zones originally interpreted as controlling structures, a third, north-striking, west dipping normal fault also intersects at the Pleistocene tufa. This complex three-way fault intersection generates two discrete fault intersection zones in the subsurface, one plunging steeply southwest and one plunging moderately northwest (Figure 7; Siler *et al.*, 2012).

Fluid up-flow from depth is likely focused within these two fault intersection zones beneath the Pleistocene tufa deposits. This fluid flow is accommodated by fault controlled fracture permeability in the Mesozoic basement, where primarily lithologic permeability is very low (Reeves *et al.*, 2012). These fluids flow out into the highly interconnected, transmissive reservoir in the middle Miocene volcanic rocks. In addition to outflow into the Tertiary section, fluid upflow continues along these discrete fault intersections into the shallow subsurface, as evidenced by the concentrated shallow temperature anomaly in the vicinity of the Pleistocene tufa deposits (Reeves *et al.*, 2012). Geothermal fluid outflow into the unconsolidated Quaternary sediments mixes with the general north-northwest to south-southeast, down-valley groundwater gradient toward Pyramid Lake. This has the effect of 'smearing' out the shallow temperature anomaly to the south-southeast of the Pleistocene tufa deposits (Figure 8).

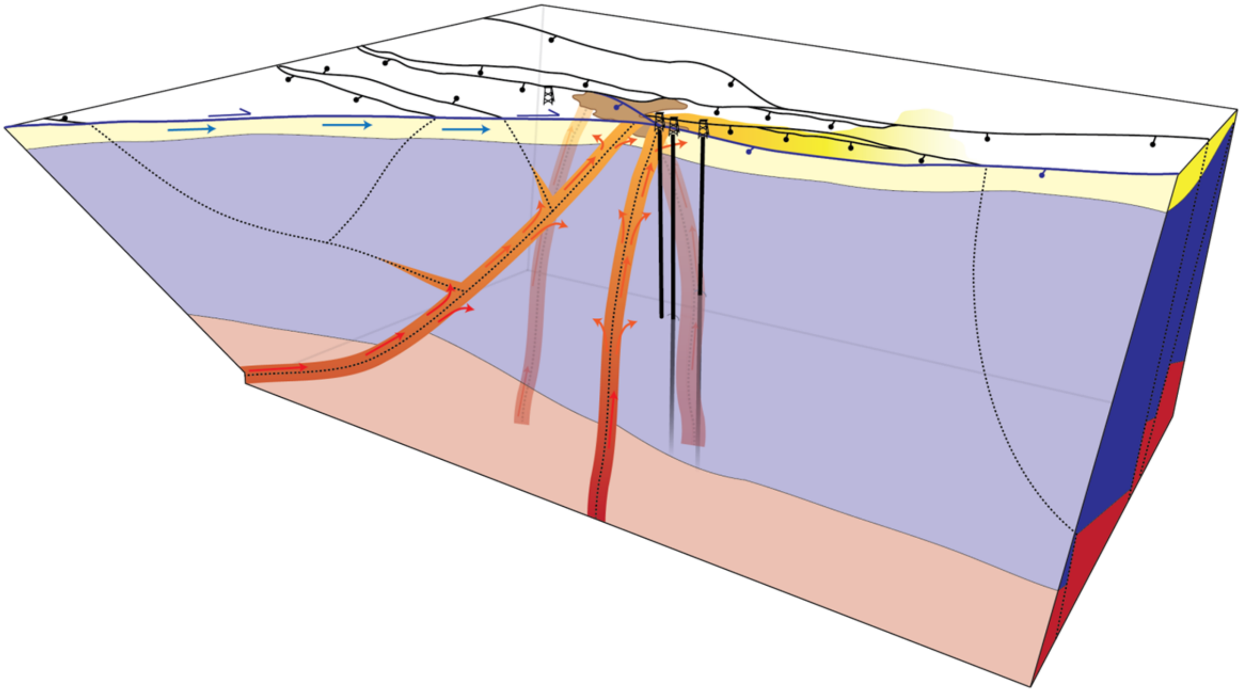

Figure 8. Conceptual model of the Astor Pass geothermal system. Fault controlled fluid up-flow through the basement (red lithology), outflows into the highly transmissive and interconnected reservoir in Miocene volcanic rocks (blue lithology). Outflow into and unconsolidated Quaternary sediment (yellow lithology) mixes with the southeastward (left-to-right) shallow ground water gradient, resulting in a smearing out of the shallow temperature anomaly to the south-southeast of the controlling fault intersections and Pleistocene tufa deposits (brown). Look direction is east northeast, with north to the left.

RESERVOIR MODEL

A state-of-the-art reservoir model was developed and calibrated for the Astor Pass geothermal system using NUFT (Nitao and Sun, 2007). NUFT (Nonisothermal Unsaturated-Saturated Flow and Transport) is a numerical model developed by Lawrence Livermore National Laboratory that simulates multi-phase, multi-component fluid flow, heat and mass transport in variably-saturated geologic media. The conceptual model proposed by Reeves *et al.* (2012) provides the basis for the development and calibration of the NUFT numerical reservoir model. Key points of the conceptual model of the Astor Pass geothermal system are:

- The Astor Pass geothermal system is a small, blind, low-entropy system with relatively isothermal temperatures at 95°C.
- Shallow temperature and magnetotelluric surveys outline a single elliptical convective plume of geothermal fluid circulation (Figure 9).
- The upwelling geothermal fluid originates from a single fault intersection or a few fault intersections in the underlying Mesozoic basement rocks.
- The geothermal reservoir exists within the faulted and jointed Miocene-age basaltic, basaltic-andesite and rhyolite rocks of the lower Pyramid sequence, which have high permeability and reservoir-scale connectivity.
- The long duration of the reservoir hydraulic test and high resolution monitoring of inflow locations along APS-1, APS-2 and APS-3 indicate that preferential flow of hydrothermal waters with temperatures significantly higher than the isothermal 95°C profile is unlikely.

This conceptual model is used to determine the numerical model domain, assign boundary conditions, and condition the permeability field. Model parameters are obtained from field data whenever possible and literature values are used when field data is unavailable. Model parameters and relevant datasets are presented in subsections specific to hydraulic, thermal, and exchange categories. The reservoir model utilizes the dual-permeability option in NUFT to assign different sets of hydraulic parameters to fractures and rock matrix. An auxiliary MODFLOW ground water flow model was developed in support of the reservoir model for inversely computing permeability values of the reservoir rocks and overlying alluvium to drawdown responses in APS-1, APS-2 and NTG4. Wells APS-1 and APS-2 are open to the reservoir at different depths and NGT4 is a water well completed in the alluvium and is located a horizontal distance of 650 m from the APS-3 pumping well. Standard values of air and water were used to parameterize phase and component properties. Geothermal modeling exercises consisted of steady-state reservoir model calibration to field measurements and observations, followed by exploitation scenarios to assess energy potential of the site. The exploitation scenarios consist of a simple dipole extraction-injection well configuration subjected to rates ranging from 15 kg/s (250 gpm) to 90 kg/s (1500 gpm).

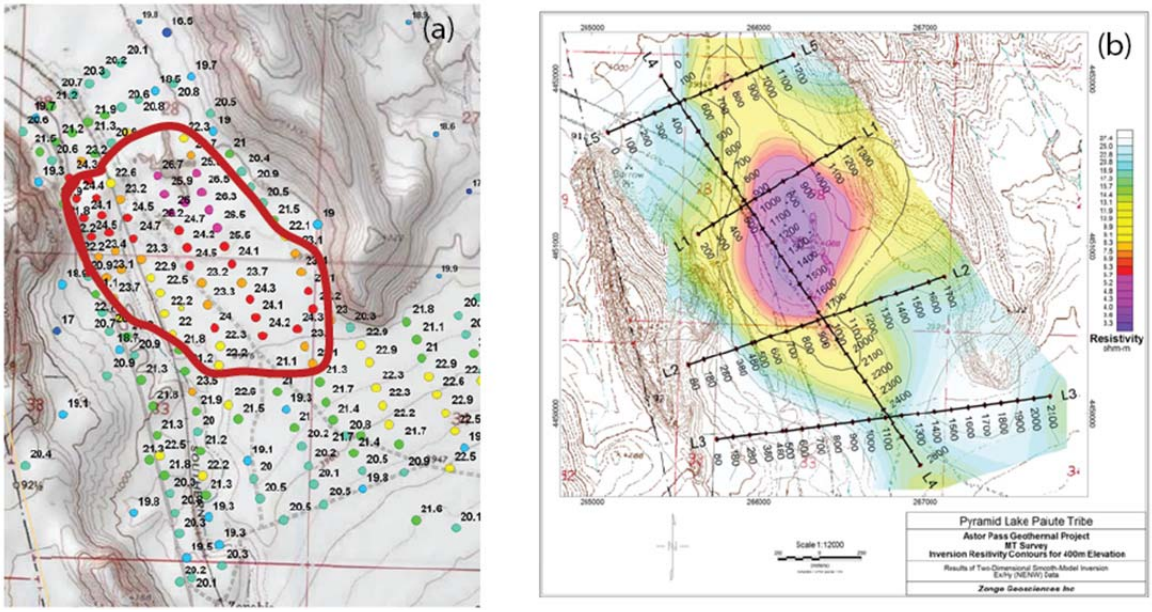

Figure 9. (a) Shallow temperature and (b) magnetotelluric surveys indicate slightly an elliptical convective plume of geothermal fluid circulation. The temperature anomaly outlined in (a) has a longitudinal extent of approximately 1.3 km.

Geologic Framework Model

The Geologic Framework Model (GFM) developed by Siler *et al.* (2012) provides a basis for model parameterization and was used to map geologic units to the reservoir model grid. The GFM can be broken into three general rock types: Quaternary alluvium, Miocene-age basaltic, basaltic-andesite and rhyolite rocks of the lower Pyramid sequence, and Mesozoic basement (primarily granodiorite). These units are shown in Figure 10 as yellow; green, orange and various shades of blue; and red, respectively. Hydraulic testing within APS-2 and APS-3 indicate that the basement rocks have low permeability and that the reservoir is considered to exist within volcanic rocks of the lower Pyramid sequence. Spinner logs in APS-1 and APS-2 and borehole geophysical surveys revealed no distinct trends in either well inflow or fracture intensity within the reservoir rocks.

Reservoir Model Domain and Boundary Conditions

The geothermal reservoir model has a rectangular domain rotated 25.6 degrees west of north to follow the natural alignment of the Astor Pass structural basin (Figure 11). The four vertices of the geothermal model given in UTM Zone 11 NAD 83 easting and northing are: 265,979 m, 4,449,541 m; 267,315 m, 4,450181 m; 265,723 m, 4,453,498 m; and 264,391 m, 4,452,860 m. This corresponds to x-, y- and z-domain lengths of 3.72 km, 1.52 km and 1.4 km, respectively. A constant cell size of 40 m on a side was used to discretize the model domain into a regularly-spaced, orthogonal grid consisting of 93 columns, 38 rows, and 35 layers.

The aerial extent of the model encompasses the region of upwelling geothermal circulation with northwest-southeast model boundaries (parallel to the longitudinal axis of the basin) located 1 km of distance away from the APS-3 extraction well and hypothetical injection well used in the exploitation scenarios (Figure 11). The northwest and southeast boundaries are assigned constant pressures of 0.5659 MPa and 0.2852 MPa at the water table, respectively, to invoke longitudinal ground water flow from northwest to southeast with a hydraulic gradient of 0.008 m. The pressure values at the water table were then scaled along the longitudinal boundaries as a linear function of depth. The side model boundaries are considered parallel to the ambient ground water flow direction and are simulated as no-flow boundaries.

The vertical dimension of the model ranges from the bottom of the Miocene volcanic rocks of the lower Pyramid sequence at an elevation of -160 m amsl to the water table located in the alluvium. The bottom model boundary is no flow, with the exception of a small circular region with an area of 4.64×10^{-2} km^2 (29 cells or 0.8% of the model area of the base layer) located just under APS-1/tufa tower that simulates the upwelling of hydrothermal fluid from faults or fault intersections in the underlying granodiorite basement. The flux of hydrothermal fluid was determined during the steady-state calibration process described in Section 2.5.6. The top model boundary has a no-flow condition.

Thermal values are assigned to the bottom and all side boundaries of the model. The longitudinal model boundaries are assigned temperatures at the water table of 20°C and 22°C based on values of ambient ground water temperature measured from the shallow temperature survey. The transverse model boundaries are assigned distance-interpolated temperatures based on the water table temperatures of the longitudinal boundary end members. A geothermal gradient of 20°C per km (www.smu.edu/geothermal/heatflow/heatflow/ThermalGradientmap.gif) is used to interpolate initial water table temperatures along all lateral boundaries as a function of depth, resulting in temperature values ranging from 20°C to 47°C along the northwest boundary and 22°C to 49°C along the southeast boundary. The bottom boundary, excluding the small 29 cell region of fluid and temperature flux, is assigned a diffusive heat flux of 100 mW/m^2 (Blackwell, 2004).The bottom flux boundary is assigned enthalpy values of 4.0×10^5 J/kg and 4.40×10^5 J/kg which correspond to constant temperatures of 95°C and 105°C. These two enthalpy values are used as lower and upper bounding cases in the exploitation simulations. Further discussion on the bottom flux boundary condition is found in Sections 2.5.6 and 2.5.7.

Hydraulic Parameters

The 30-day hydraulic test generated an excellent dataset for hydraulic parameterization of the reservoir model. Wells APS-1 and APS-2 are open to the reservoir at different depths, and water well NTG4 is completed in the overlying alluvium. These wells are located at horizontal distances of 177 m, 114 m, and 650 m from the APS-3 pumping well, respectively. APS-1, APS-2 and APS-3 are open to the reservoir through single screened intervals greater than 300 m.

A MODFLOW ground water flow model is used to determine hydraulic parameters that best match drawdown responses in APS-1, APS-2 and NTG4. MODFLOW is a single-phase, isothermal, saturated ground water flow code. Advantages of using this code to compute hydraulic parameters include simple model setup and very fast simulation times. Execution times for the MODFLOW simulation runs are approximately 1 minute, whereas execution times for the NUFT reservoir model ranges between 3-5 days. Thus, the fast execution times of the MODFLOW model facilitate an exhaustive exploration of the hydraulic parameter space that would not be possible with the reservoir model.

The MODFLOW model domain is similar to the geothermal reservoir model domain, but is smaller and has a finer cell resolution of 25 m on a side for enhanced resolution of the simulated drawdown response (Figure 12). The MODFLOW model extends 1250 m, 4600 m and 1250 m in the x-, y- and z-domains for a total of 50 columns, 92 rows, and 50 layers. The vertical extent of the MODFLOW model ranges from the water table down to the basement rocks. Consistent with the reservoir model, the MODFLOW model simulates longitudinal ground water flow from northwest to southeast according to a hydraulic gradient of 0.008. The transverse boundaries are no flow. The MODFLOW model simulates the hydraulic test by reaching steady-state conditions followed by transient simulation. Actual pumping rates at APS-3 over the 30-day duration, including times when pumping ceased, are honored in the model.

Final hydraulic parameters are assigned to the reservoir model based on the parameter combination that produces the best matches to reservoir drawdown. Two different permeability conceptualizations were used to match the reservoir trends: equivalent porous media (EPM) and discrete fault network (DFN). The two permeability field conceptualizations and best parameter sets are discussed in the subsections below. Only the EPM case is incorporated in the reservoir model.

Equivalent Porous Media

The EPM conceptualization assumes that the reservoir rock is highly fractured such that equivalent permeability tensors can be assigned to the reservoir volcanic rocks and the overlying alluvium. The EPM approach is supported by observations of long-range reservoir connectivity from water responses in APS-1 and NTG4 to pumping in APS-3, high fracture frequency observed in the borehole geophysical logging of APS-3, lack of clear changes in fracture intensity between different strata within the reservoir, and the isothermal temperature profiles observed during all temperature surveys.

The MODFLOW model was first hand-calibrated and then linked to the inverse parameter estimation code PEST (Doherty, 2000) to minimize differences between measured drawdown at APS-1, APS-2 and NTG4. PEST was allowed to change horizontal and vertical hydraulic conductivity and storage (specific storage, specific yield) values of both the alluvium and volcanic reservoir rock. Best-fit alluvium and volcanic permeability values, converted using 95°C values for fluid properties, are listed in Tables 2 and 3. The reservoir model is dual-permeability, and the reader should refer to Table 2 for permeability assigned to the matrix and

Table 2. Astor Pass geothermal reservoir model matrix continuum hydraulic properties.

Unit	Matrix Continuum Hydraulic Properties			
	kx (m2)	ky (m2)	kz (m2)	θs
Alluvium	3.64e-14	3.64e-14	7.28e-15	0.30
Reservoir	1.00e-18	1.00e-18	1.00e-18	1.0e-06

Table 3. Astor Pass geothermal reservoir model fracture continuum hydraulic properties.

Unit	Fracture Continuum Hydraulic Properties			
	kx (m2)	ky (m2)	kz (m2)	θs
Alluvium	1.00e-19	1.00e-19	1.00e-19	1.00E-06
Reservoir	2.91e-14	2.91e-14	5.83e-12	1.00E-10

Table 3 for fracture permeability. Permeability values for the inactive continua (i.e., fractures for the alluvium, and matrix for the volcanics) are set to values representative of low-permeability bedrock to restrict flow (Anderson and Woessner, 1992).

The match between observed and simulated drawdown in APS-1, APS-2 and NTG4 using the PEST-calibrated parameters is excellent (Figure 13). Strong vertical anisotropy in the volcanic reservoir rocks was found to be paramount in representing drawdown in APS-1 and APS-2. Vertical and horizontal permeability of the reservoir rocks differ by 2.3 orders of magnitude which translates to K_z being 200 times more permeable than K_x and K_y. The high vertical permeability reflects the vertical to sub-vertical orientation of the faults and fractures in the Astor Pass system, while the horizontal permeability reflects a lesser degree of horizontal interconnection between these vertical structures. An anisotropy ratio of 0.17 (K_x and K_y are 5.6 times higher than K_z) for the alluvium best reproduces observed drawdown in NTG4. This ratio is consistent with ranges reported for unconsolidated sedimentary deposits (Freeze and Cherry, 1979).

In addition to parameter estimation, the EPM MODFLOW model was used to preliminarily assess maximum extraction-injection rate used in the exploitation simulations. This involved a dipole configuration with APS-3 as the pumping well and an upgradient theoretical injection well (Figure 12). A pumping rate of 2,000 gpm producing 167 m of drawdown was identified as a potential maximum. Note that the MODFLOW model does not include thermal processes, such as fracture-matrix heat exchange, and the 2000 gpm maximum extraction-injection rate only serves as a rough estimate. More discussion on maximum extraction-injection rates for the Astor Pass geothermal system is found in Section 2.5.8.

Discrete Fault Model

The DFN approach conceptualizes that the permeability of the reservoir rock is dominated by large faults with little connectivity and permeability provided by smaller, background joints and faults. The DFN model consist of 19 faults imaged from the seismic surveys and correlated to observed slickenslides during drilling, zones of lost circulation, geologic contacts and, in some cases, the orientation of the tufa tower (Siler *et al.*, 2012). The faults from the GFM model were developed in EarthVision and are curved along both strike and dip, and contain a hierarchy that defines cross-cutting relationships of individual faults. Translation of these features to the reservoir model grid involved two steps. The first step involved the computation of best-fit planar coefficients to the EarthVision fault planes. These best-fit 19 fault planes are shown in Figure 14. The second step involved honoring the fault hierarchy for the first three hierarchy levels in the EarthVision fault tree.

The 19 faults were then mapped to the MODFLOW model grid according to the fracture continuum method of Reeves *et al.* (2008) and Parashar and Reeves (2011) that honors permeability and flow anisotropy in interconnected fault networks on a continuum grid. Calibration of the DFN fields involved shifting the permeability of the volcanic reservoir rocks from an equivalent tensor applied throughout the model to the largest faults. This was accomplished by assigning nominal values to the background permeability to represent a very small permeability contribution from small joints and faults, and orders of magnitude greater permeability values to the fault planes.

Several approaches were used in an attempt to match observed drawdown in APS-1, APS-2 and NTG4 using the DFN permeability field structure. These include: (1) assigning uniform permeability to all fault planes, (2) using fault dilation tendency computed from a stress field analysis (Figure 15) to assign three different classes of fault permeability and (3) modification of (2) where grid cells containing more than one fault (conceptualized as a fault intersection) are placed into the highest permeability class. The fault dilation tendency (DT) cases involved assigning permeability classes based upon the criteria: (1) $DT < 0.2$, (2) $0.2 \leq DT \leq 0.8$ and (3) $DT > 0.8$. The first permeability class assumes that DT values less than 0.2 are unfavorable for maintaining flow through open fault structures and the background volcanic permeability values were assigned to those grid cells. Intermediate and high fault permeability values were assigned to the other two classes, with at least one order of magnitude in permeability differentiating the intermediate and high permeability cases. All DFN approaches utilized hand-calibration rather than PEST automated calibration due to the complexity of flow through interconnected fault networks.

All DFN approaches produced reasonable matches to APS-2 and NTG4, and poorer matches to APS-1 (Figures 16 and 17). Simulated drawdown in APS-1 mimics the overall trend of the observed drawdown although the simulated magnitude of drawdown is only one-third of the observed. It is important to note that the bottom of the APS-1 screened interval is located approximately 451 m and 517 m above the top of the APS-2 and APS-3 screened intervals,

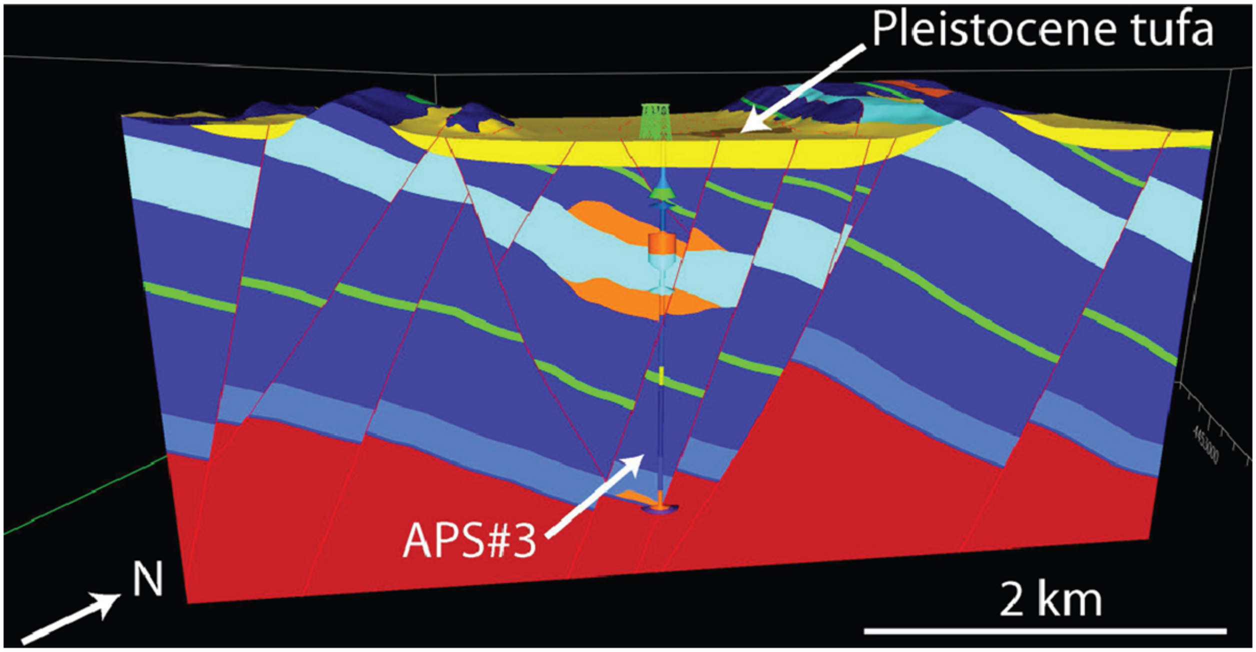

Figure 10. ENE-WSW cross-section of Astor Pass 3D geologic framework model. Quaternary alluvium is yellow. Blues, green and orange correspond to Miocene basalts and andesites, intercalated sedimentary and volcaniclastics, and rhyolitic lava flows and intrusions, respectively, of the lower Pyramid sequence. Red is the Mesozoic basement. From Siler *et al.* (2012).

respectively. This implies that a network of presumably large faults and smaller background joints and faults govern the complex interaction between pumping in APS-3 and drawdown in APS-1. It is interesting finding nonetheless that the 19 faults can reproduce the observed drawdown trend at APS-1, albeit with considerably less magnitude. As an aside, a fault connecting APS-1 and APS-3 was added to the 19 fault structures. This resulted in minimal change in simulated drawdown at APS-1. Thus, it is concluded that the connectivity structure of faults and fractures within the reservoir rocks is more sophisticated than the inclusion of the 19 large faults from the seismic surveys, and as a result, only the EPM permeability representation was used in the reservoir model.

Exchange Parameters

A dual-permeability flow field is used to model fluid flow and heat transport within the Astor Pass geothermal system. The dual-permeability framework involves the computation of fluid pressure and heat at two nodes within each grid block given that fluid flow and heat transport can occur between fracture-fracture nodes, matrix-matrix nodes, and fracture-matrix nodes. Fracture-matrix flow is simulated as an exchange term dependent on pressure and temperature gradients between the fracture and matrix continua, interfacial permeability and heat conductance of the two continua, surface area of the fracture walls relative to grid volume, and flow length of each continua (Nitao and Sun, 2007). The geothermal reservoir is saturated which does not necessitate the implementation of a dual-permeability model to accurately simulate fluid flow within the reservoir; however, the dual-permeability flow field is needed to describe the flux of heat between the fracture and matrix continua during the exploitation scenarios.

The use of the dual-permeability option in NUFT requires the computation of primary and secondary continua flow length [L] and flow area density [L^2/L^3] parameters (Table 4). These parameters are listed as L_{prim}, L_{sec}, and *flow-area-density* in NUFT terminology, respectively (Nitao and Sun, 2007). These parameters are only used in the computation of fracture-matrix flux terms. Values of L_{prim} assigned to the matrix, or primary, continuum is computed from the expression:

$$L_{prim} = \Delta / n_f \tag{8}$$

where Δ is cell size and n_f is the number of fractures in a given grid cell. Flow length in the fracture, or secondary, continuum, L_{sec}, is defined as:

$$L_{\mathrm{sec}} = b_h / 2. \tag{9}$$

The flow-area-density parameter A [L^2/L^3] is defined as:

$$A = \frac{\sum_{i=1}^{n_f} a_i}{V} \tag{10}$$

where a_i is fracture area within the volume V of a grid cell. The computation of A, L_{prim} and L_{sec} depend on fracture spacing. Two end member fracture spacings are used in the computation of these parameters for the EPM model based on wellbore geophysical logging. The end members consist of an average fracture spacing of 1.3 m for open- and partially-open fractures with apertures of 150 microns, and 15 m for open-fractures with 350 micron apertures (Reeves *et al.*, 2012) (Table 4). The actual fracture spacing for geothermal fluid conducting fractures is likely between these two end members.

Note that the exchange parameters in Table 4 primarily govern heat exchange, and any subsequent thermal drawdown characteristics, between the two continua during the exploitation scenarios. This was confirmed in the EPM model as different values of exchange parameters produced identical (or near-identical) steady-state pressure and temperature fields.

Thermal Parameters

Thermal properties for the reservoir model consisted of solid, air and liquid thermal conductivity k_T for the alluvium and volcanic reservoir rock, and specific heat capacity (Table 5). All thermal properties for the model were obtained from the engineering toolbox (www.engineeringtoolbox.com) using rock types representative of the Astor Pass geothermal

Table 4. Astor Pass geothermal reservoir model dual-domain exchange properties for reservoir rocks for the two end member fracture spacing reported in Reeves *et al.* (2012).

Fracture Spacing	**Dual-Continuum Exchange Properties**		
	Lprim (m)	**Lsec (m)**	**A (m2/m3)**
1.3 m	0.65	6.72e-05	2.50
15 m	7.50	1.73e-04	0.20

Table 5. Astor Pass geothermal reservoir model thermal and bulk properties.

Unit	**Thermal and Bulk Properties**				
	ρD (kg/m3)	**kT solid (W/m·°C)**	**kT air (W/m·°C)**	**kT liquid (W/m·°C)**	**cp (J/kg·°C)**
Alluvium	2100	0.5	3.0	4.0	500
Reservoir	2700	2.0	3.0	4.0	790

system. These values were confirmed with values reported in Robertson *et al.*, 1988. The k_T values for solid, air and liquid are required by NUFT and consist of rock or soil under a vacuum, air-filled pores, and water-filled pores, respectively.

Steady-State Reservoir Model

The primary objective of developing a reservoir model is to assess the energy potential of the Astor Pass geothermal system. The first step of any reservoir modeling exercise is to run the reservoir model to steady-state temperature and pressure conditions and calibrate model parameters to reproduce field measurements and observations. The calibration metrics for the model include: (1) an isothermal or near-isothermal temperature profile within a region defined by APS-1, APS-2 and APS-3 at 95°C, (2) elliptical temperature anomaly with a longitudinal extent of approximately 1.3 km, and (3) pressure fields supporting convective fluid circulation. The excellent fit of the EPM-derived hydraulic parameters to drawdown measured in APS-1, APS-2 and NTG4 provide confidence that the hydraulic parameters utilized in the reservoir model appropriately constrain hydrologic fluxes within the model.

The steady-state calibration process involved modifying the bottom model boundary condition used to simulate geothermal fluid circulation. Possible modifications to the bottom model boundary include total area of the boundary, hydrothermal fluid flux, and fluid temperature (input into the model as enthalpy). The final bottom model boundary configuration is circular and consists of 29 cells for an area of 4.64×10^{-2} km^2. This boundary, though circular, produces an elliptical temperature profile at the water table (Figure 18a). This elongated temperature signature at the water table arises in the reservoir model from the interaction of the circular region of upwelling geothermal fluid with ambient temperature, longitudinal ground water flow.

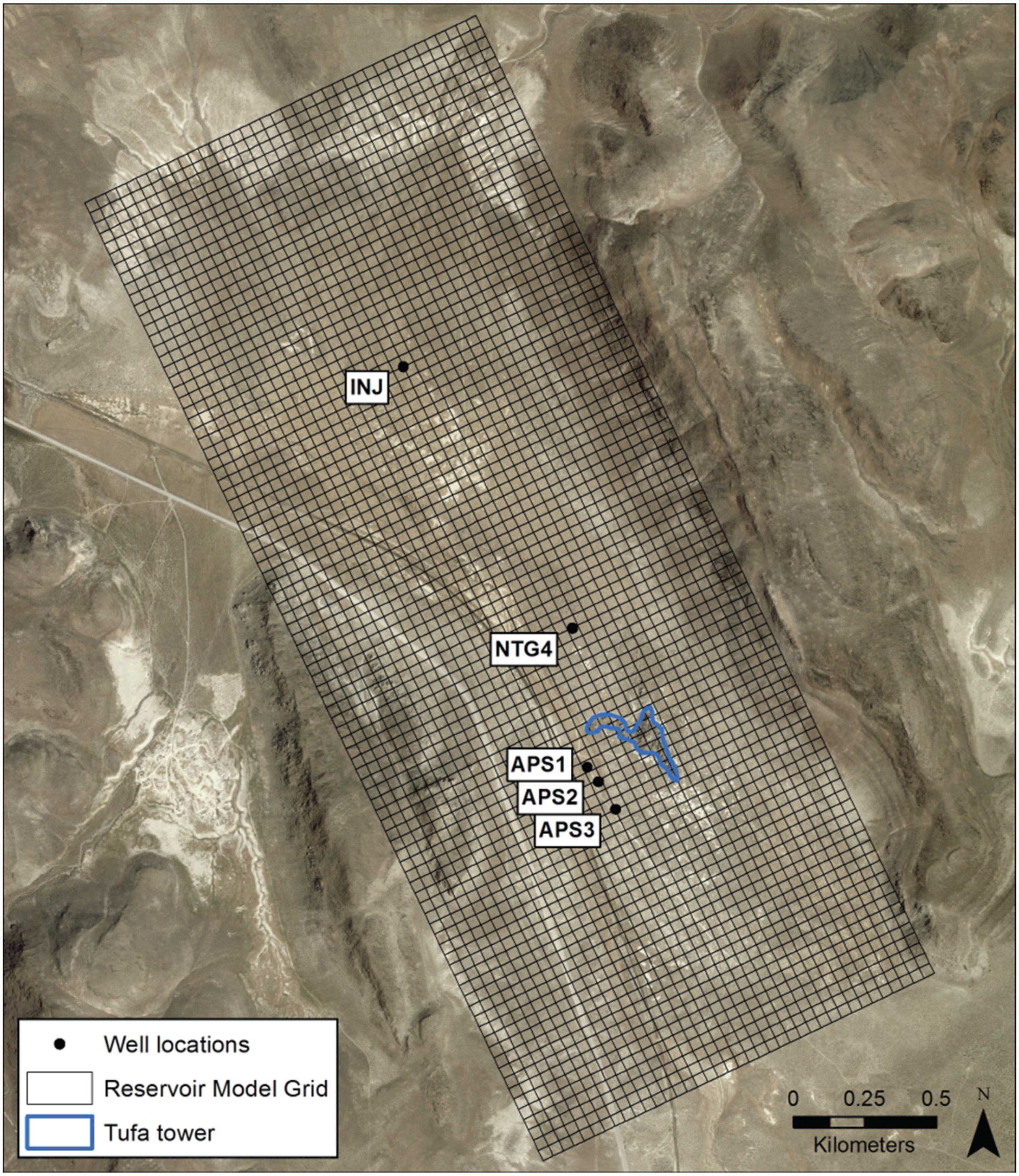

Figure 11. Astor Pass geothermal model grid showing locations of APS-1, APS-2, APS-3, NTG4, and theoretical injection well used in the exploitation scenarios for energy scaling.

The size of the ellipse at the water table was then calibrated to flux rates assigned to the bottom model boundary. Boundary fluxes of 8 kg/s and 10 kg/s were found to adequately replicate the observed temperature anomaly delineated from the shallow temperature survey (Figure 9). Note that this analysis assumes that the shallow 2 m temperatures result from heat traveling vertical upward through the unsaturated zone from the water table. Thus, only the size (not temperatures) of the shallow temperature anomaly in Figure 9 and region of elevated temperatures simulated by the model at the water table can be compared. While both 8 kg/s and 10 kg/s fluxes were found to adequately replicate the shallow temperature anomaly, the higher boundary flux of 10 kg/s produced an area of higher temperature that more closely approximated the temperature anomaly. Increasing the boundary flux to 12 kg/s was found to generate too large of an area of elevated temperature at the water table. Both the 8 and 10 kg/s boundary fluxes produce pressure fields consistent with the conceptual model of convection geothermal fluid circulation (e.g., Figure 18b).

Vertical temperature profiles within the zone of convective fluid circulation for fluid fluxes of 8 kg/s and 10 kg/s are shown in Figure 19 for a fluid temperature of 95°C assigned to the bottom boundary. Regardless of flux, the model cannot reproduce the isothermal temperature profiles from APS-1, APS-2 and APS-3 shown in Reeves *et al.* (2012). Temperature profiles are sensitive to magnitude of flux prescribed to the bottom model boundary as 8 kg/s and 10 kg/s flux correspond to temperatures of 70°C and 75°C at the water table. While not isothermal, the steeper temperature profiles produced by the 10 kg/s prescribed flux condition more closely approximate an isothermal profile. In addition, average temperatures in the model are less than 95°C. This necessitated raising the temperature of fluid entering the model at the lower boundary to 105°C for a second set of steady-state model solutions. The steady-state temperature and pressure fields for these simulations are shown in Figure 20. Vertical temperature profiles for the 105°C bottom boundary condition with fluxes of 8 kg/s and 10 kg/s in Figure 21 show similar trends to the corresponding cases shown in Figure 19, with the exception of higher temperatures. These two sets of steady-state models with boundary temperatures of 95°C and 105°C serve as lower and upper end members for the energy scaling computations.

Exploitation Scenarios and Energy Scaling

The exploitation scenarios utilize reservoir temperature and pressure fields from the steady-state reservoir models with source temperatures of 95°C and 105°C to simulate the extraction of total thermal energy. Two extraction-injection dipole configurations were used in the exploitation scenarios: (1) extraction from APS-3 and injection into the theoretical well shown in Figure 11, and (2) extraction from APS-3 and injection into APS-1. The temperature of injected water output from a theoretical geothermal power plant is set to 50°C for all exploitation scenarios. Transient temperature and pressure profiles for each dipole configuration for a 95°C source temperature and 10 kg/s flux are shown in Figures 24 and 25.

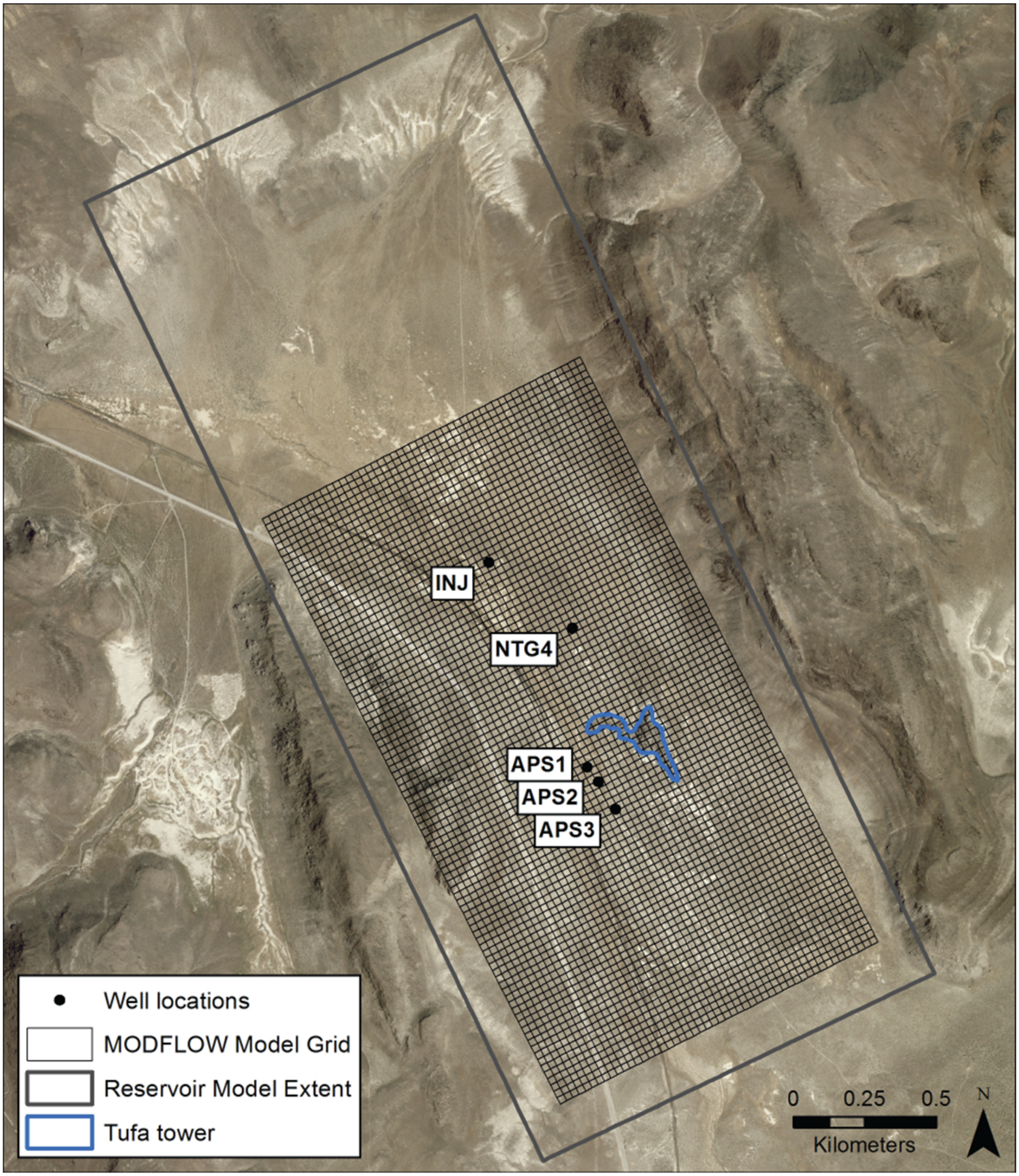

Figure 12. MODFLOW hydraulic parameter ground water model grid showing locations of APS-1, APS-2, APS-3 and NTG4. Note outline of Tufa tower, geothermal reservoir model domain, and location of theoretical injection well used for preliminary estimates of total pumping/injection rates.

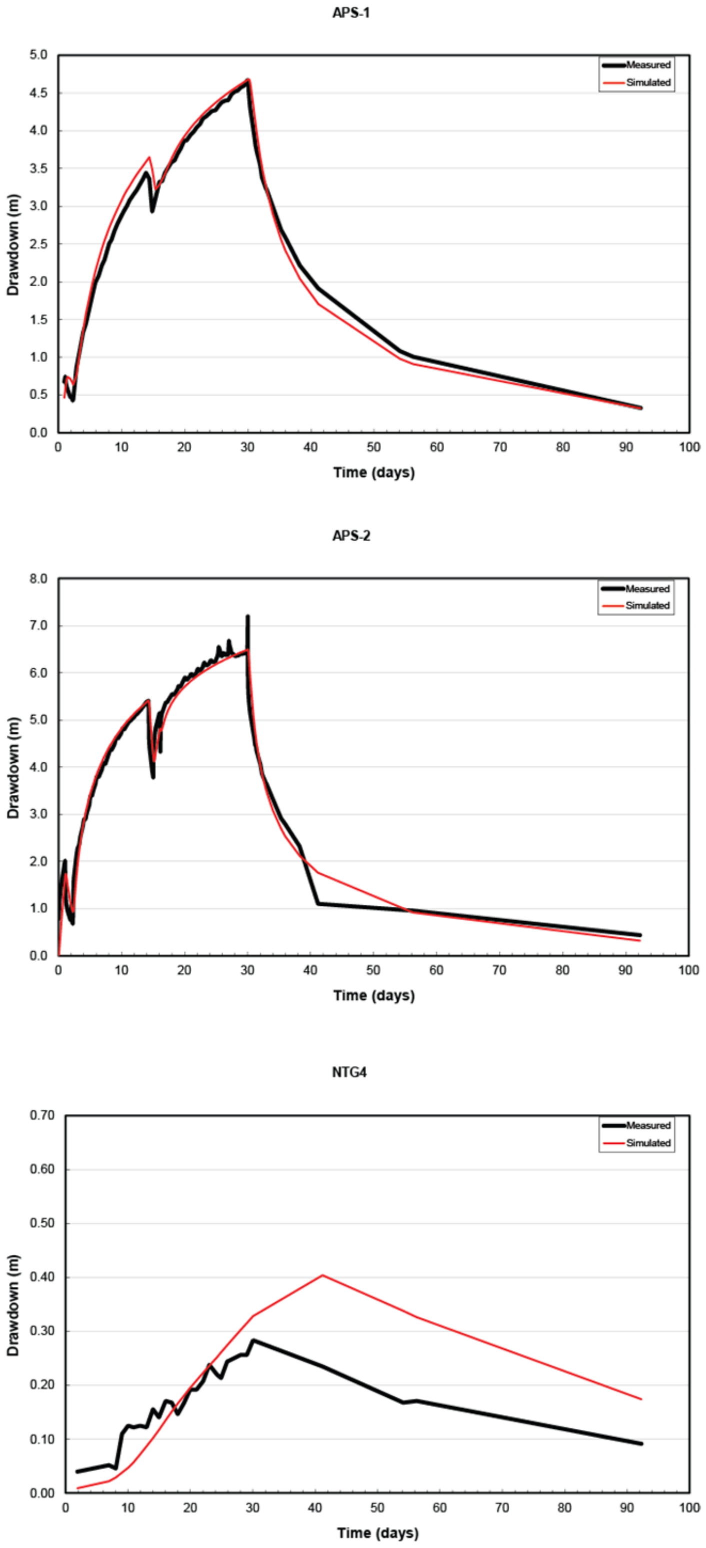

Figure 13. EPM MODFLOW model with best-fit hydraulic parameters calibrated to drawdown trends from APS-1, APS-2 and NTG4 located in the overlying alluvium.

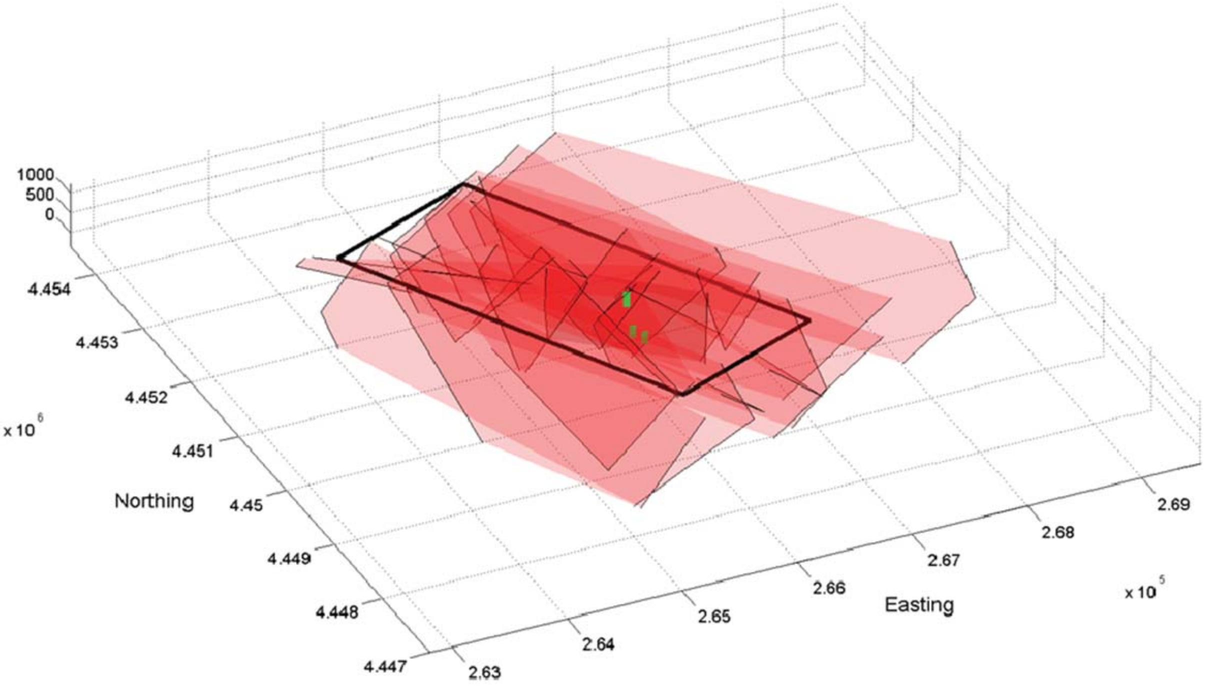

Figure 14. Best-fit planar representations of 19 faults used in the DFN permeability structure. The reservoir model outline is shown in black and the open intervals of APS-1, APS-2 and APS-3 are shown as green rectangles.

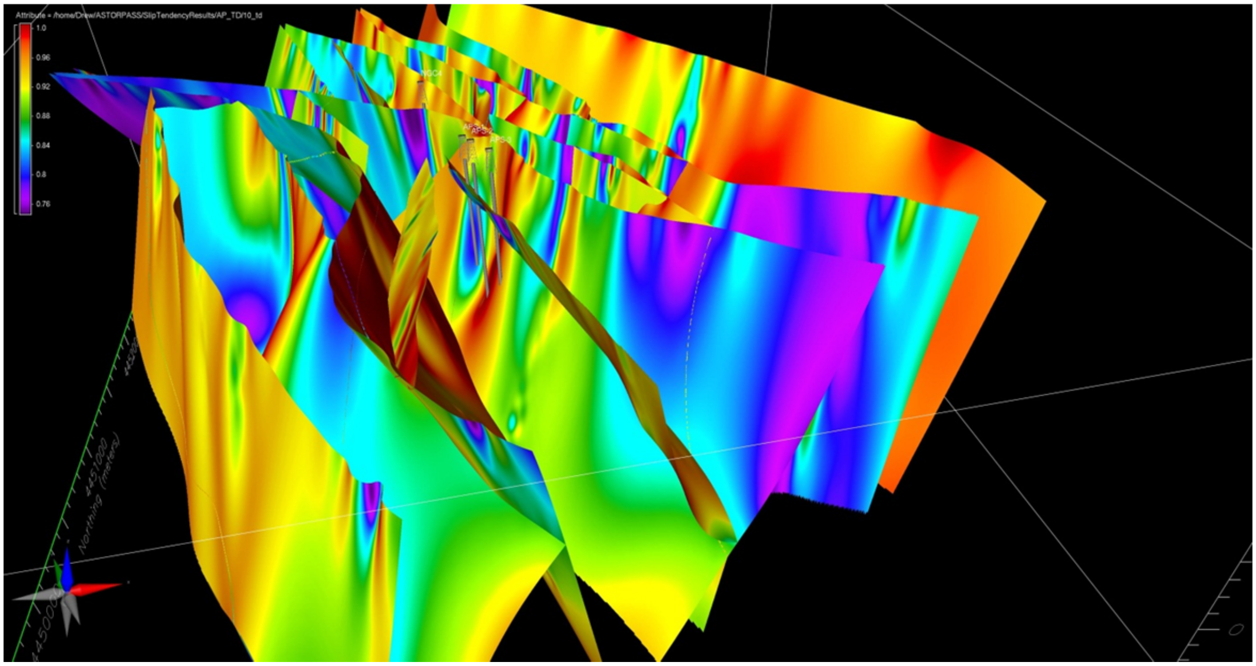

Figure 15. Dilation tendency for all 19 fault structures present within the Astor Pass geothermal model. Note that the dilation tendency value is truncated at 0.75 to emphasize areas with higher dilation tendency.

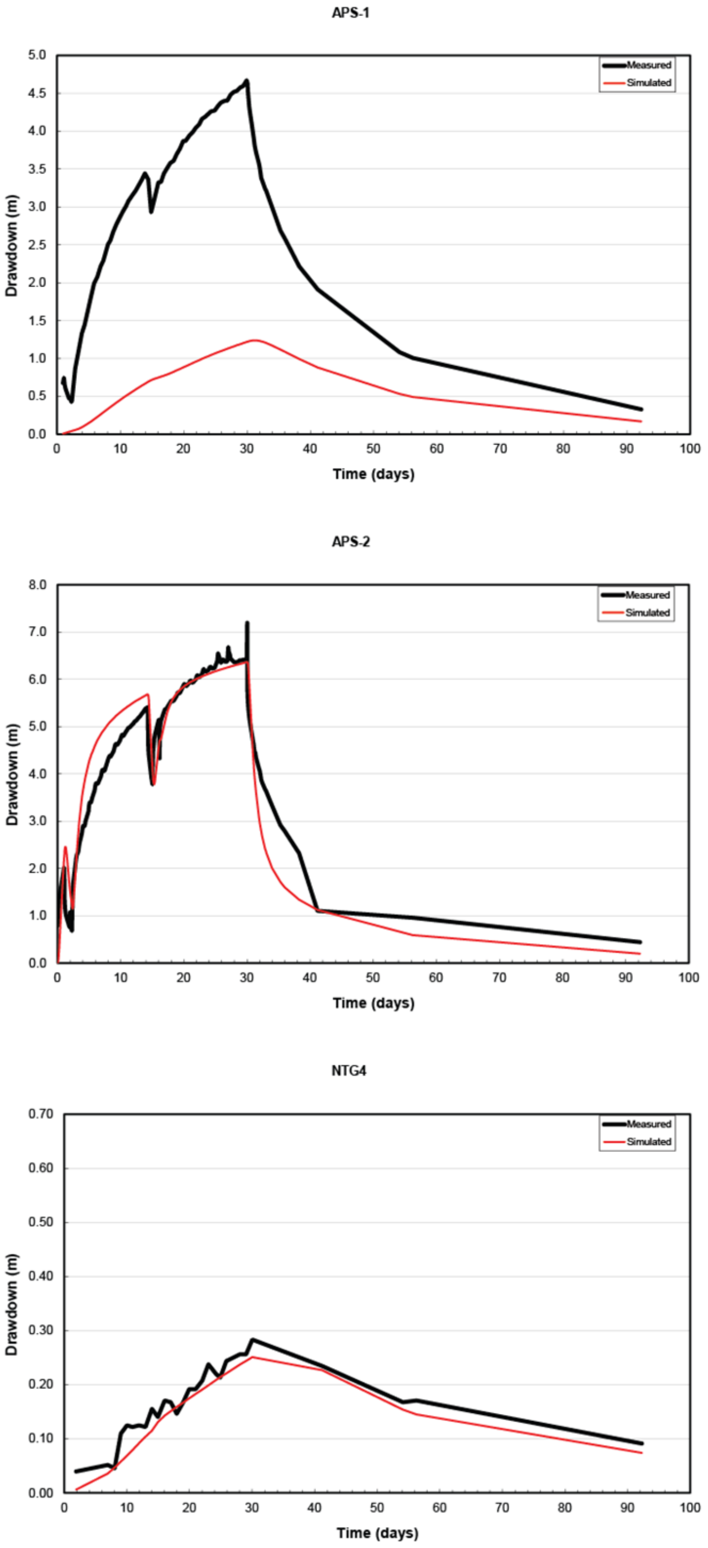

Figure 16. DFN MODFLOW model with best-fit hydraulic parameters calibrated to drawdown trends from APS-1, APS-2 and NTG4 located in the overlying alluvium. All fault planes are assigned a uniform k of 7.11×10^{-8} m^2.

Constant extraction-injection rates over a 30-year exploitation period were allowed to systematically vary from 15 kg/s (250 gpm) to 90 kg/s (1500 gpm) in increments of 15 kg/s for both dipole configurations. NUFT computes total energy in megawatts (MW) extracted from extraction well APS-3. This total energy value is then scaled to net energy according to the study of Heberle and Bruggemann (2010) which indicates 7 percent efficiency for low-temperature, isopentane binary systems. This efficiency does not include parasitic loads associated with the extraction and injection wells which further reduce the estimated efficiency to 5 percent. Thus, net energy is defined in this report by utilizing a 5 percent efficiency to scale NUFT-computed total energy output at APS-3.

Fluid temperatures at the extraction well over time are a function of the distribution of fluid temperature across the APS-3 screened interval. Initial temperatures for the 95°C and 105°C source temperatures with a flux of 10 kg/s are 90°C and 96°C, respectively. This corresponds to initial net energy production of 0.60 MW and 0.63 MW given a 30 kg/s (500 gpm) extraction-injection rate (Figures 24 and 25). These net energy values form a relatively narrow envelop that defines the potential energy output of the Astor Pass geothermal system per 30 kg/s increments of extraction-injection. Note that the relation between enthalpy and net energy production is approximately linear in the range of the reservoir temperatures.

Thermal drawdown trends over the 30-year exploitation period vary significantly between the two dipole configurations, and increase with extraction-injection rate. The theoretical injection and APS-3 extraction well configuration exhibits the lowest thermal drawdown for both the 95°C and 105°C source temperatures over the 30-year period, with estimates ranging between 4 and 10 percent for 15 kg/s (250 gpm) and 90 kg/s (1500 gpm) extraction-injection rates, respectively. The APS-1 injection and APS-3 extraction well configuration exhibits the highest thermal drawdown for both the 95°C and 105°C source temperatures over the 30-year period, with estimates ranging from 4 and 18 percent for 15 kg/s (250 gpm) and 90 kg/s (1500 gpm) extraction-injection rates, respectively.

The minimal thermal drawdown for the theoretical injection and APS-3 extraction dipole configuration can be explained by the low-temperature of the system, where the injected temperature of 50°C is only cooler by an average of 40°C to 46°C from the temperature at the APS-3 extraction well. The injection theoretical well is located a significant distance away for the zone of hot, convective circulation and provides pressure support for extraction activities at APS-3. The use of APS-1 as an injection well, however, results in the injection of cooler 50°C water directly into the zone of hot, convective circulation. The close proximity of APS-1 to APS-3 results in relatively short fluid flow pathways, decreased residence times of fluid between injection and extraction, and subsequently greater thermal drawdown than the other dipole configuration.

Sensitivity analyses were used to identify the influence of dual-domain parameters and fluid flux rates on net energy production over time. Thermal drawdown trends were found to be

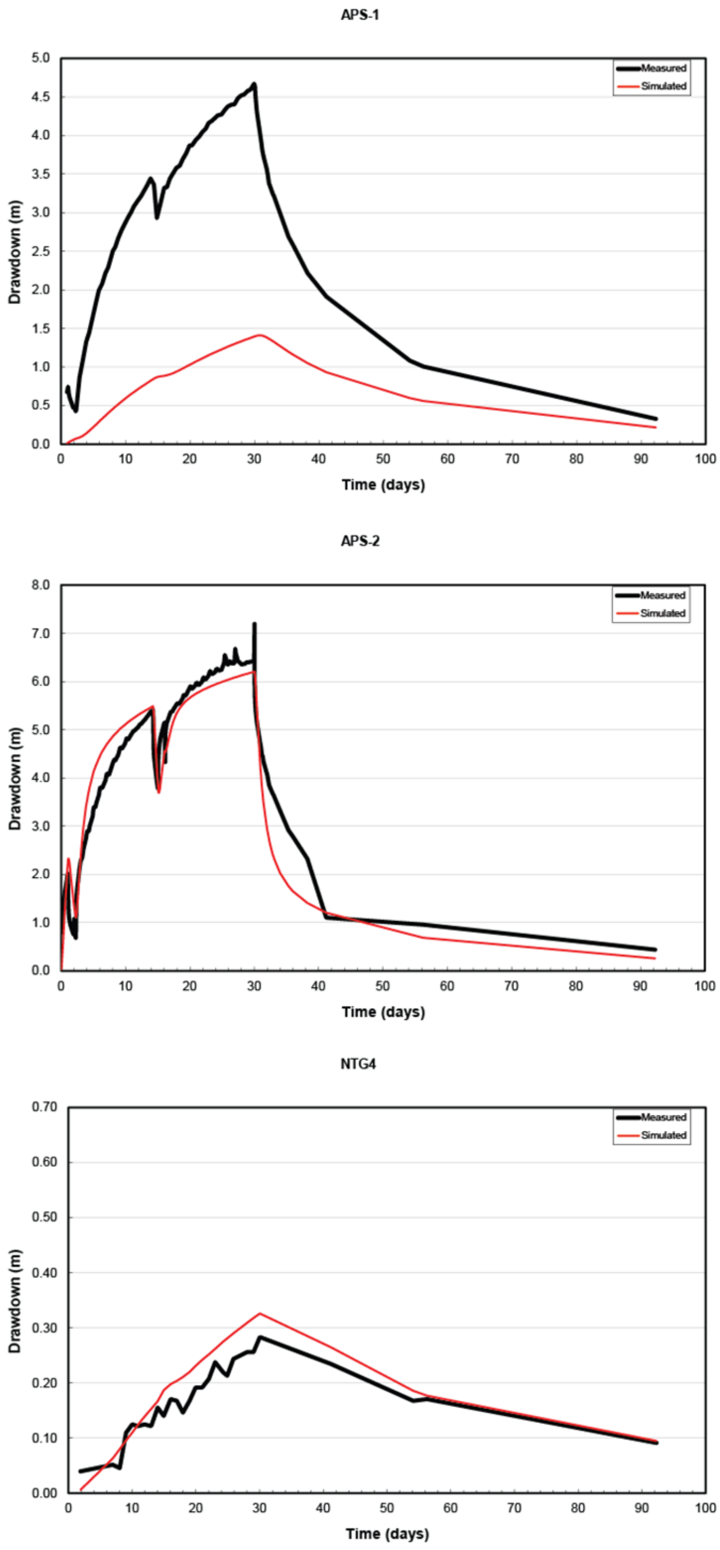

Figure 17. DFN MODFLOW model with best-fit hydraulic parameters calibrated to drawdown trends from APS-1, APS-2 and NTG4 located in overlying alluvium. Permeability assigned to fault planes is grouped into three bins: low – 1.6×10^{-9} m^2, intermediate – 3.2×10^{-9} m^2, high – 1.9×10^{-7} m^2 according to values of dilation tendency.

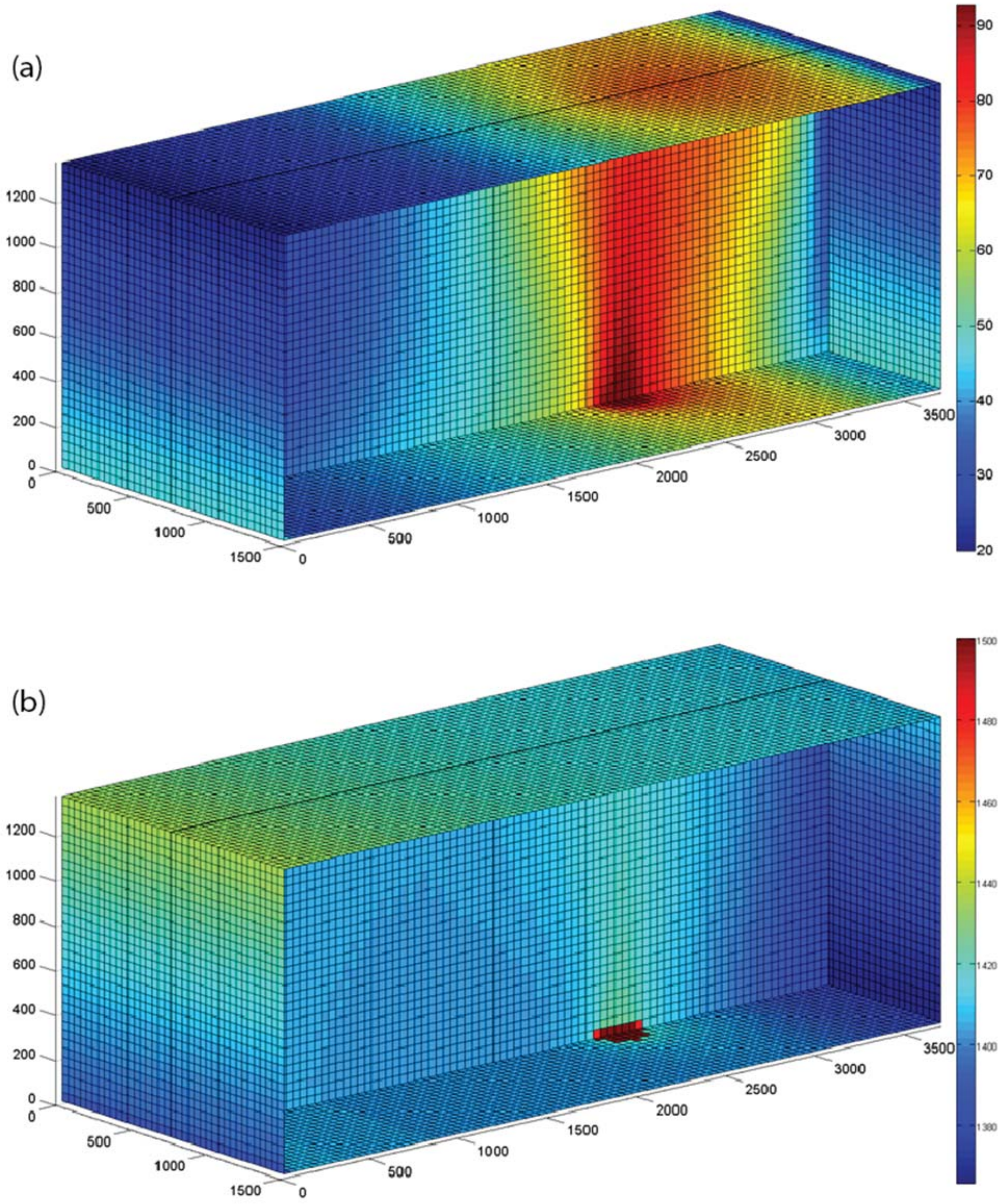

Figure 18. Geothermal reservoir model with steady-state profiles of (a) temperature and (b) head for source temperature of 95°C and fluid flux of 10 kg/s. Note the hydrothermal source location in both plots. Head values in (b) are truncated to a maximum of 1500 m.

relatively insensitive to the two sets of dual-domain parameters listed in Table 4. Net energy production for the 8 kg/s and 10 kg/s source flux values at an extraction-injection rate of 30 kg/s (500 gpm) differed by less than 4 percent.

Model Limitations

The reservoir model adequately reproduces the dominant characteristics of the Astor Pass geothermal system. However, all models are simple abstractions of more complex systems. While the EPM hydraulic parameter set used in the reservoir model produced excellent fits to observed drawdown, not much is known about the actual fault and joint networks within the reservoir. These networks are well-connected at the reservoir scale and exhibit relatively high permeability, yet the frequency and surface area of the fractures that actively transmit thermal fluid is unknown. EPM models overestimate fracture connectivity and subsequently thermal drawdown values for both dipole configurations could be under predicted. In particular, thermal drawdown values could exceed 18 percent in the APS-1 injection and APS-3 extraction configuration due to their close proximity and high potential for short circuiting along a few dominant faults.

The net energy production of the site as shown in Figures 24 and 25 could approach 1.8 MW assuming a sustained extraction-injection rate of 90 kg/s (1500 gpm). However, extraction-injection rates used in the model may not reflect the quantity of fluid that the reservoir is able to transmit continuously over a 30-year exploitation period. The success of extraction and injection wells in fractured rock masses typically depend on long screened intervals that increase the probability of the intersecting actively conducting faults and joints that are connected to a larger fracture network structure. The field hydraulic test involved APS-3 pumping at a rate of 450 gpm for 30-days with only 7 m of maximum drawdown – this corresponds approximately to the 30 kg/s (500 gpm) extraction-injection rate for an energy production between 0.60 and 0.63 MW. Therefore it is known with a high degree of confidence that reservoir can be exploited using a 30 kg/s extraction-injection rate. The upper extraction-injection rate, however, remains unknown and requires field validation.

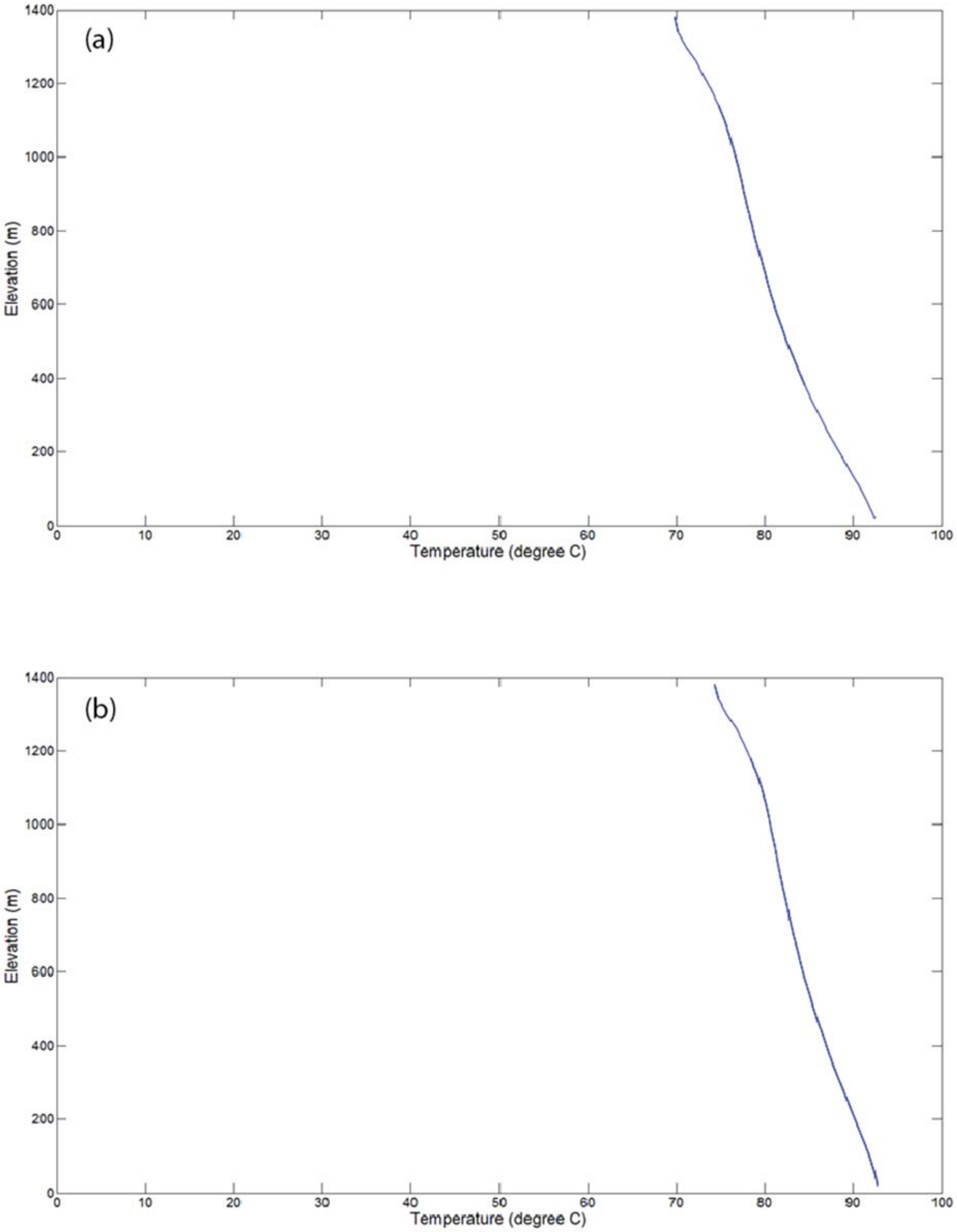

Figure 19. Steady-state temperature profile within center of convective plume with 95°C source temperature and (a) 8 kg/s and (b) 10 kg/s fluid flux. Note that the distribution of temperature is near-isothermal with a temperature of 70°C for 8 kg/s and 75°C for 10 kg/s at the water table (top of the model).

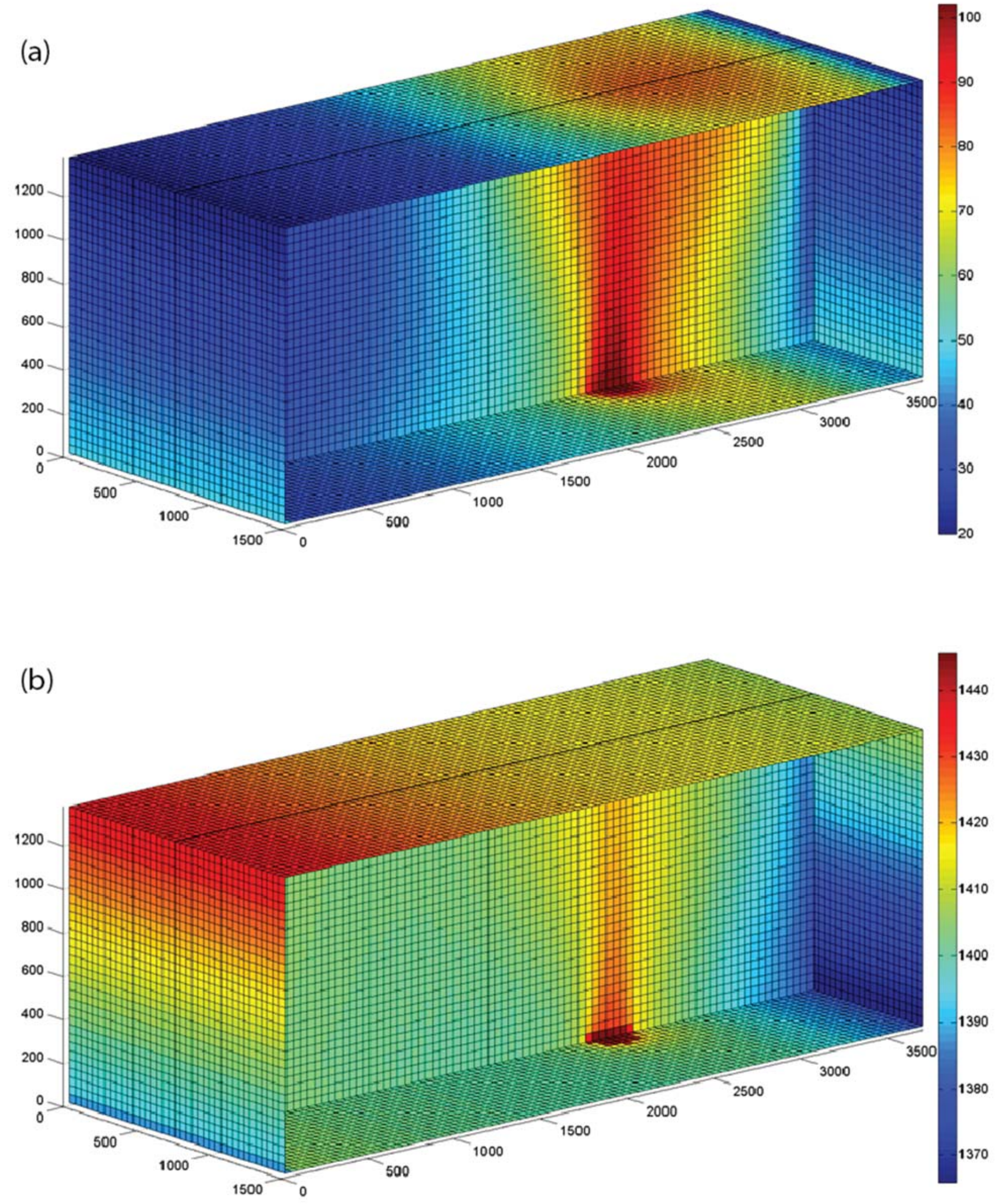

Figure 20. Geothermal reservoir model with steady-state profiles of (a) temperature and (b) head for source temperature of 105°C and fluid flux of 10 kg/s. Note the hydrothermal source location in both plots.

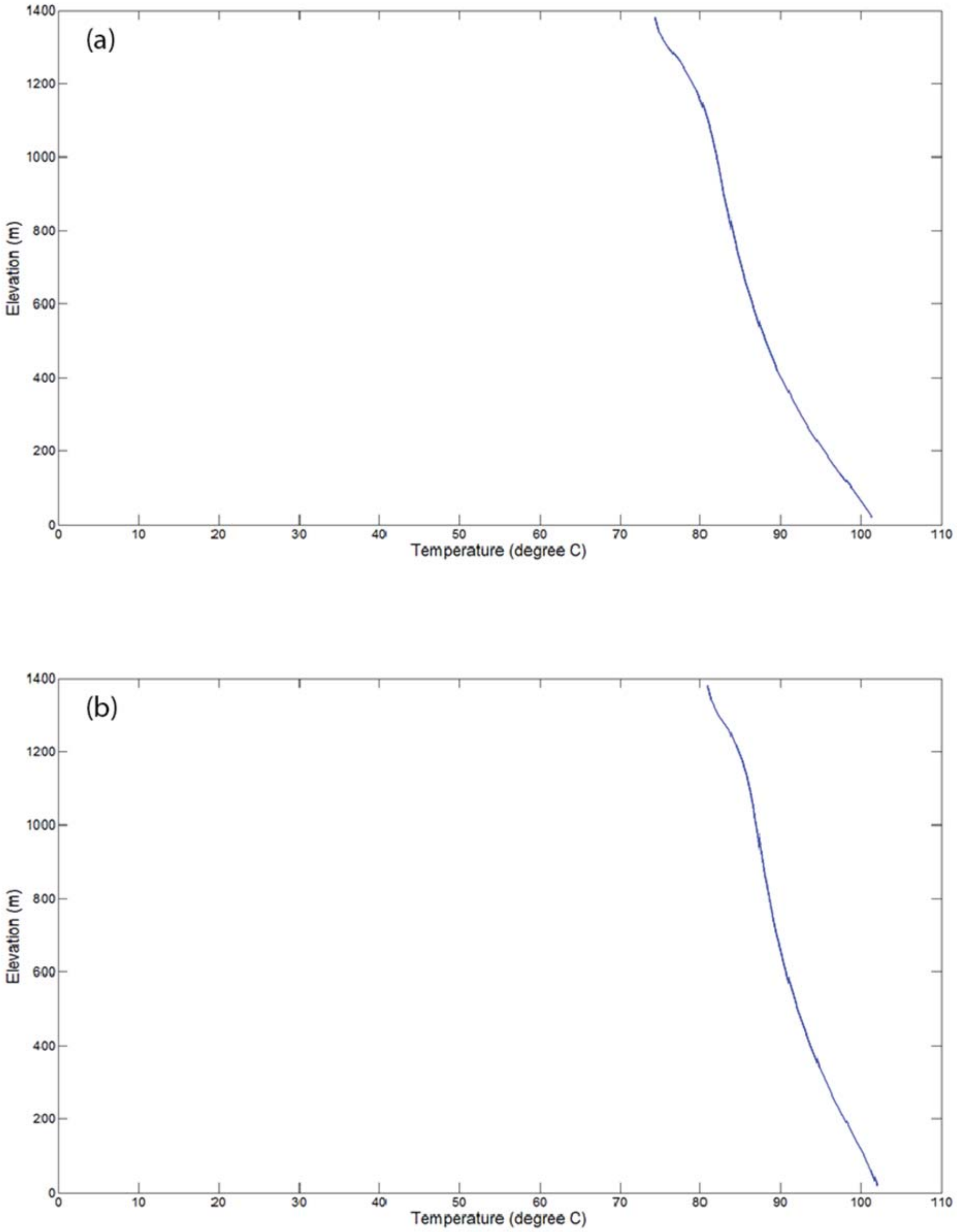

Figure 21. Steady-state temperature profile within center of convective plume with source temperature of 105°C and (a) 8 kg/s and (b) 10 kg/s fluid flux. Note that the distribution of temperature is near-isothermal with a temperature of 75°C for 8 kg/s and 82°C for 10 kg/s at the water table (top of the model).

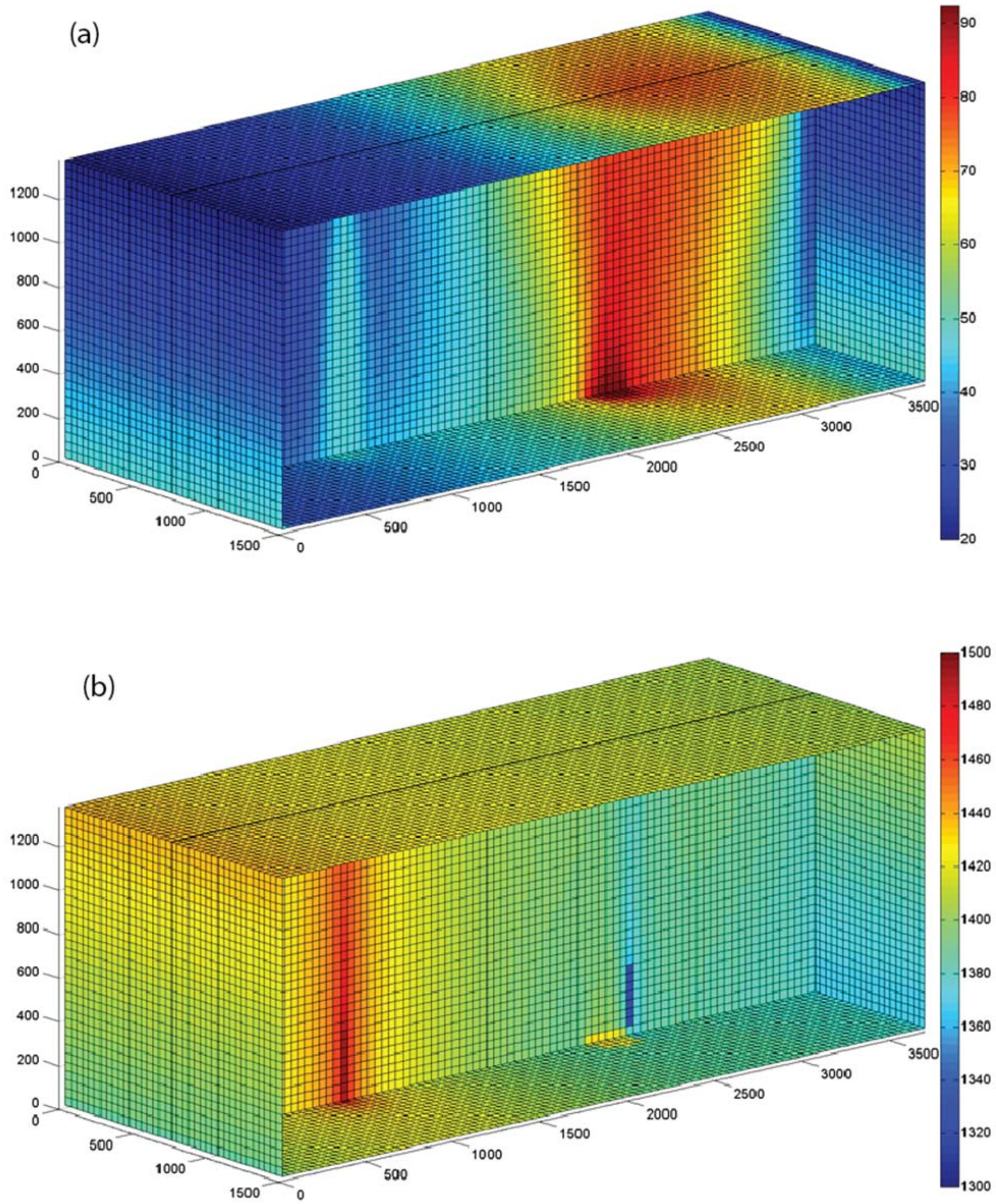

Figure 22. (a) Geothermal reservoir model with (a) temperature and (b) head profiles during exploitation scenarios with theoretical injection well shown in Figure 4 for 95°C source temperature and 10 kg/s flux. Note the dipole configuration in (b) with the injection well serving as a source and extraction well (APS-3) serving as a sink. Head values in (b) are truncated between 1300 m and 1500 m.

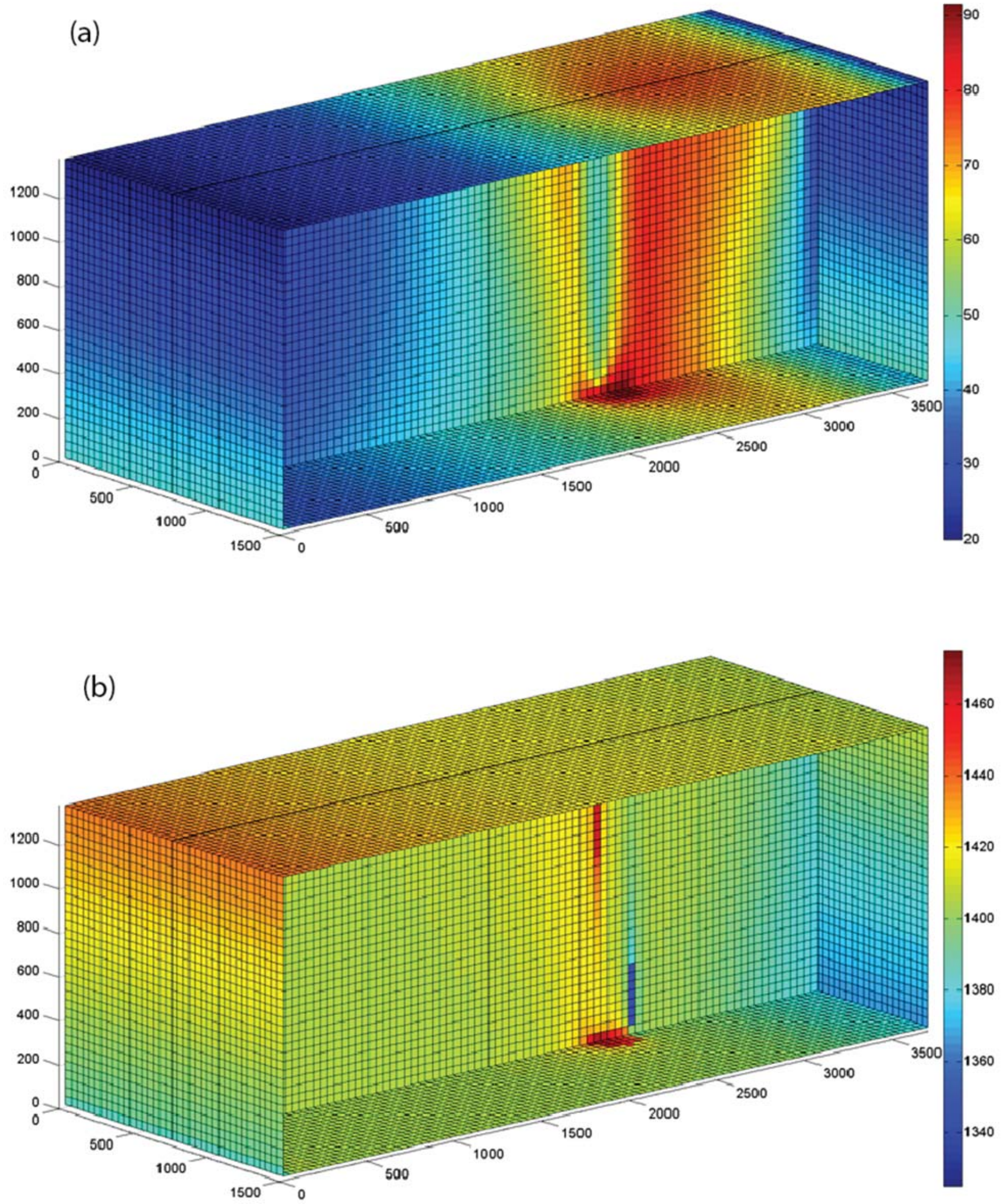

Figure 23. (a) Geothermal reservoir model with (a) temperature and (b) head profiles during exploitation scenarios with APS-1 injection well for 95°C source temperature and 10 kg/s flux. Note the dipole configuration in (b) with APS-1 serving as a source and extraction well (APS-3) serving as a sink. Head values in (b) are truncated between 1325 m and 1475 m.

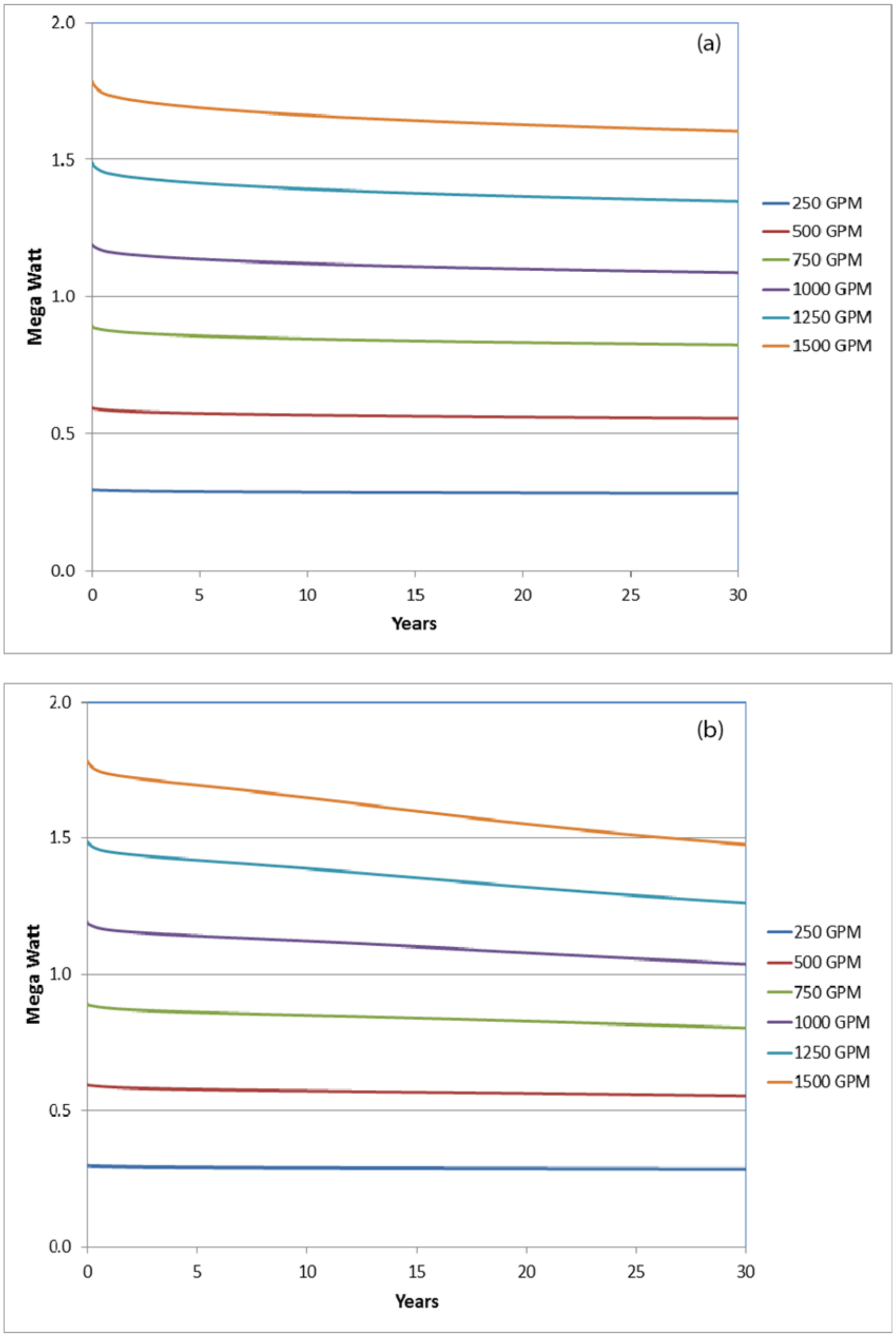

Figure 24. Net energy production for the (a) theoretical injection well and APS-3 dipole and (b) the APS-1 and APS-3 dipole configurations with a fluid flux of 10 kg/s and 95°C boundary temperature. Initial water temperature for all cases is 90°C which corresponds to an initial net energy production of 0.60 MW at a 30 kg/s (500 gpm) extraction-injection rate. Thermal drawdown over a 30-year exploitation period is highest in the APS-1 and APS-3 dipole and ranges up to 4% for a 15 kg/s (250 gpm) extraction-injection rate and 17% for a 90 kg/s (1500 gpm) extraction-injection rate.

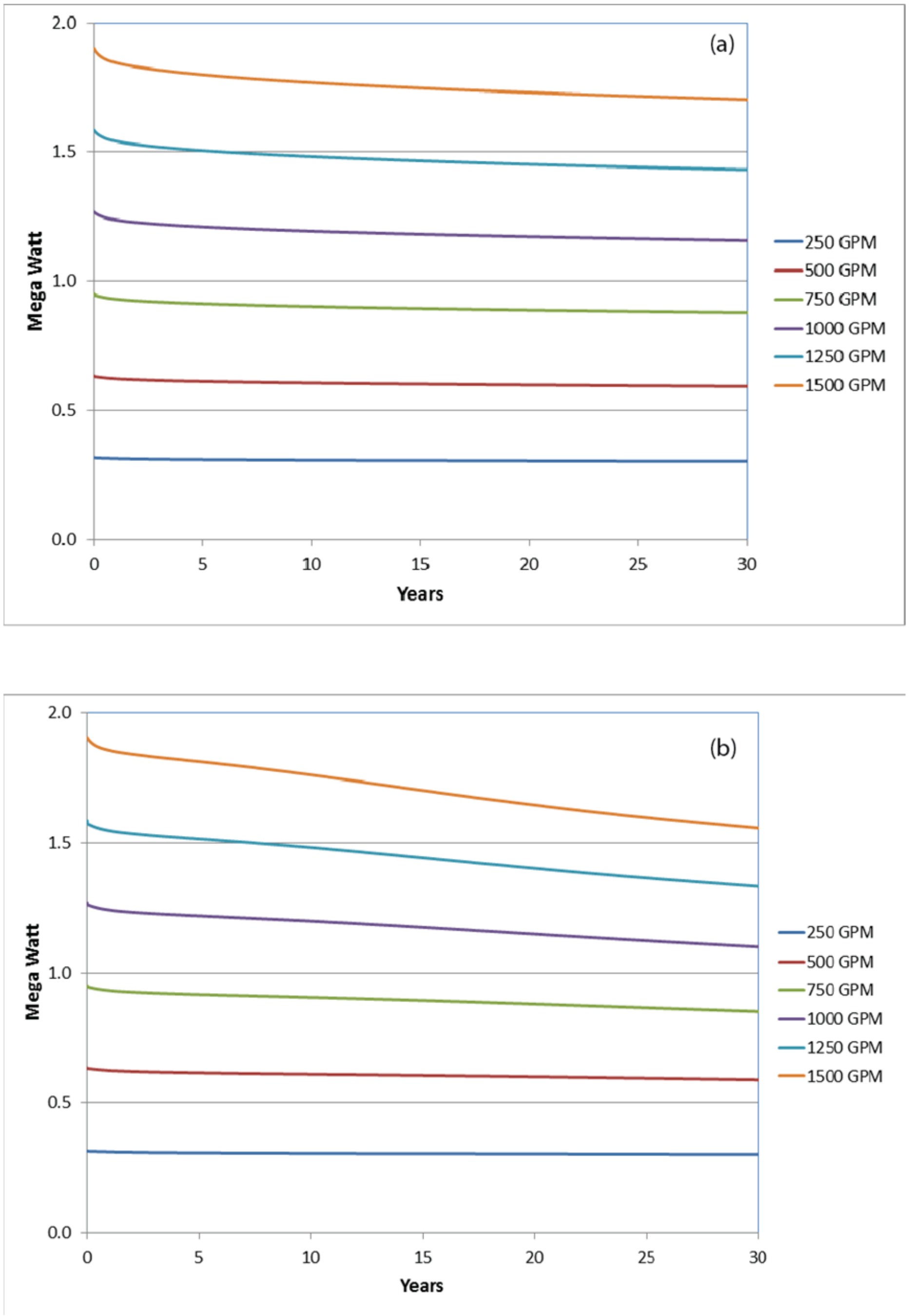

Figure 25. Net energy production for the (a) theoretical injection well and APS-3 dipole and (b) the APS-1 and APS-3 dipole configurations with a fluid flux of 10 kg/s and 105°C boundary temperature. Initial water temperature for all cases is 96°C which corresponds to an initial net energy production of 0.63 MW at a 30 kg/s (500 gpm) extraction-injection rate. Thermal drawdown over a 30-year exploitation period is highest in the APS-1 and APS-3 dipole and ranges up to 4% for a 15 kg/s (250 gpm) extraction-injection rate and 18% for a 90 kg/s (1500 gpm) extraction-injection rate.

RESERVATION-WIDE GEOTHERMAL EXPLORATION

Shallow Temperature Survey

As part of the initial Shallow Temperature Survey on the Pyramid lake Reservation, 2m temperature probes were conducted in Emerson Pass. The area was encouraging due to surface alteration in the geology shown in the hyper spectral imagery. Emerson Pass showed a structural complexity of silica and calcite veining in altered rocks, and a spatial correlation between the shallow heat anomaly and a complex system of faults along the eastern side of the pass. After the initial discovery of this anomaly by Chris Kratt in 2010 (see figures 26 and 27) the staff at Pyramid Lake prepared the equipment and was trained to conduct a complete shallow temperature survey in Emerson Pass in 2012.

The Tribal crew completed over 80 shallow temperature probes in Emerson Pass and along the north end of Pyramid Lake. Table 6 lists data that was collected with temperatures over 80 degrees Fahrenheit. The highest soil temperature of ~83^{0}C (182F) was found on the east side of the valley and delineated a shallow high temperature anomaly in an oblong shape at the base of the eastern hills (see figures 28 and 29).

A few more temperature probes were surveyed in March 2013 (Shevenell and Zehner) to confirm the anomalously hot temperatures detected by the Tribal crew and normalize the data to the original survey so that all the data sets could be compared. The maximum recorded temperature is associated spatially with the horse-tailing termination of a controlling fault.

Based upon the appearance of a subtle temperature reversal between the range front to near the toe of the fan ~700 m to the west, it is postulated that the geothermal fluids ascend a north south striking structure. The abrupt drop in temperature to the south may result from a northwest-striking fault that acts an impermeable barrier and is not oriented favorably for slip and/or dilation. Shallow temperatures return to background values west of the controlling fault as well, which may result from Quaternary alluvium masking the heat signature.

To further refine the zone of geothermal upwelling, four temperature gradient wells were drilled in Emerson Pass with funding from the Department of the Interior. Figure 30 provides the location of these wells (EPTG1 through EPTG4) along the range front. Based upon the occurrence of isothermal intervals in EG 1 and EG2 (see figure 31) and borehole lithology, it is postulated that these two gradient hole intercepted outflow zone and or faults with hot water migration through them.

EPTG1 was drilled to 100 feet with air before all returns were lost, suggesting that a fault zone was intersected. The circulating medium was changed over to mud in an effort to control the loss circulation conditions and went to 140 feet before the rig went through a large amount of mud with no returns. Since a fault is the likely reason for the loss of returns it was decided to complete the well before it was lost. The total depth was 145 feet with a maximum flow line temperature of 107^{0}F. EPTG2 was drilled to 250 feet with air with a maximum flow line temperature of 152^{0}F. EPTG 3 was drilled with air to a total of 250 feet, with a maximum flow

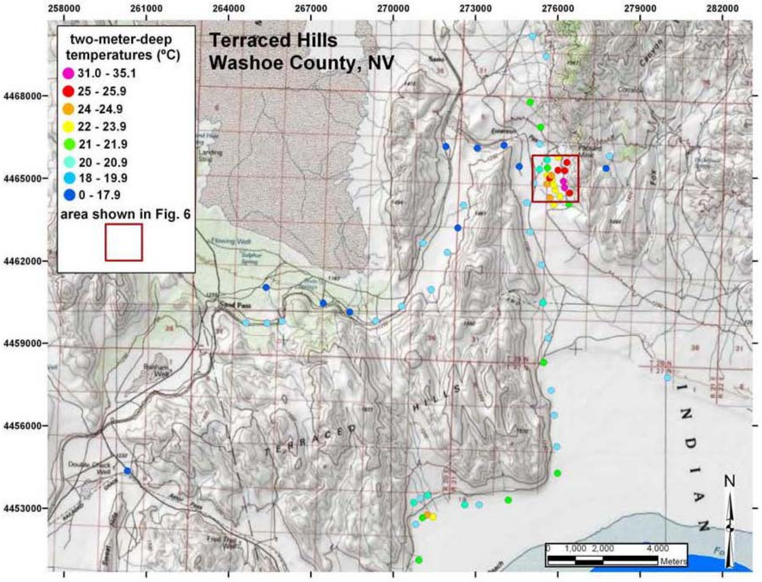

Figure 26. Location map of Emerson Pass and shallow temperature data acquired in 2010.

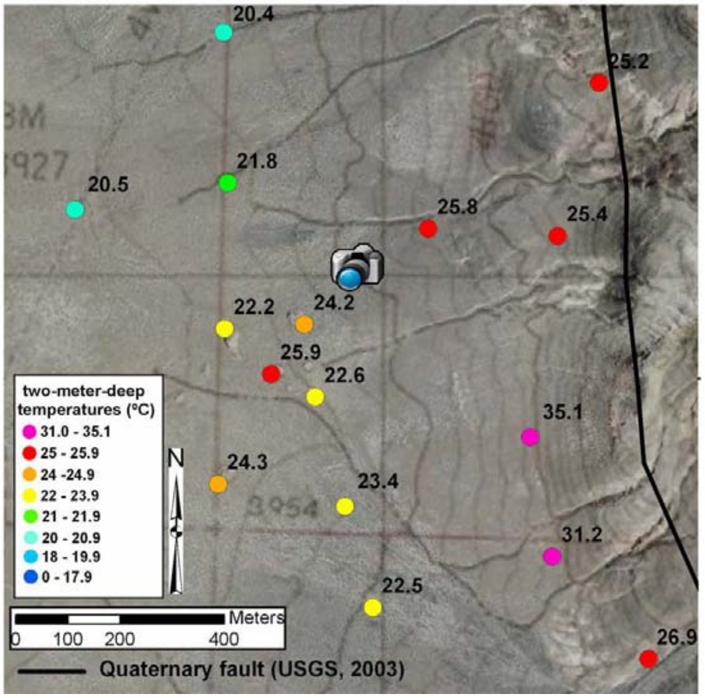

Figure 27. 2010 Shallow (2 meter) temperature survey showing temperature at 2 meters below ground level in Degrees Centigrade. The highest observed temperature was 35.1 degrees C (95.2F).

Table 6. Temperature data at 2 meters below ground level in excess of 80 degrees Fahrenheit acquire in 2012. (UTM coordinates in NAD83)

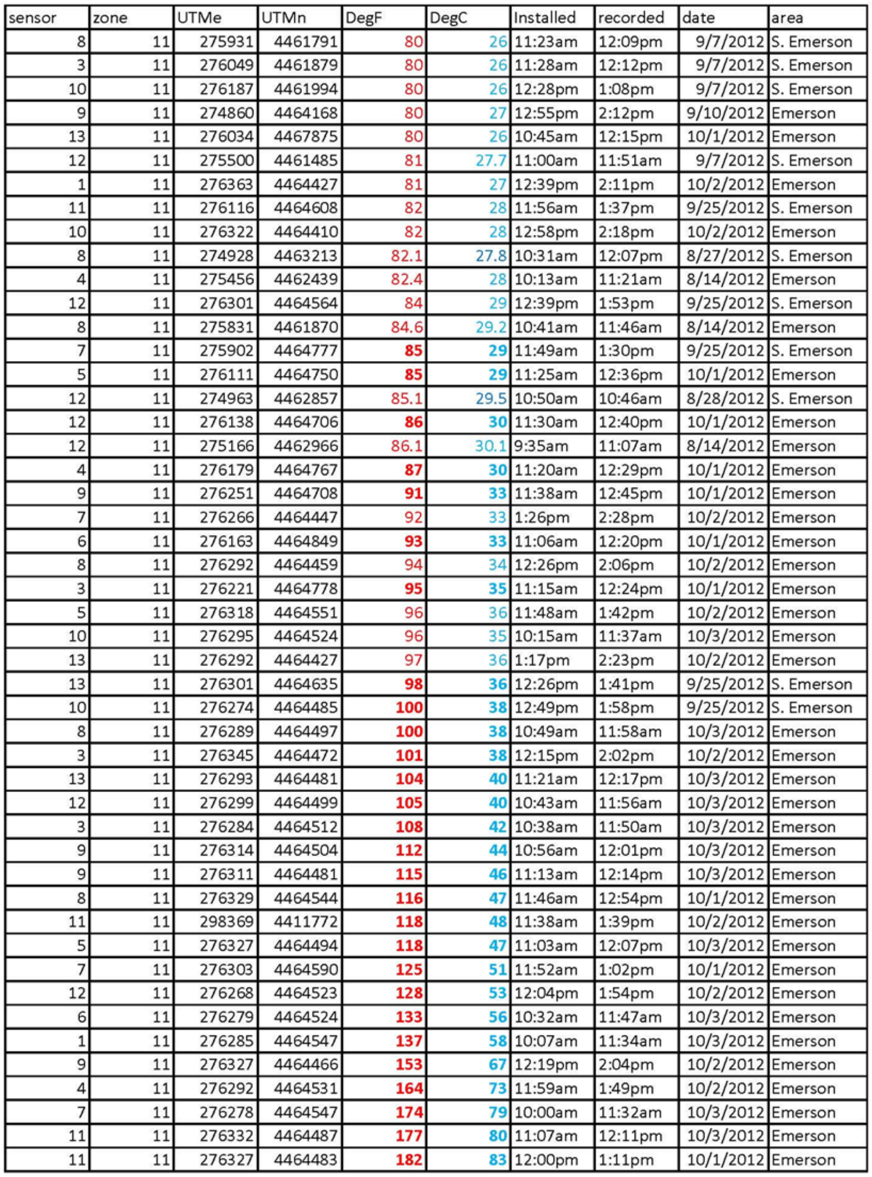

sensor	zone	UTMe	UTMn	DegF	DegC	Installed	recorded	date	area
8	11	275931	4461791	80	26	11:23am	12:09pm	9/7/2012	S. Emerson
3	11	276049	4461879	80	26	11:28am	12:12pm	9/7/2012	S. Emerson
10	11	276187	4461994	80	26	12:28pm	1:08pm	9/7/2012	S. Emerson
9	11	274860	4464168	80	27	12:55pm	2:12pm	9/10/2012	Emerson
13	11	276034	4467875	80	26	10:45am	12:15pm	10/1/2012	Emerson
12	11	275500	4461485	81	27.7	11:00am	11:51am	9/7/2012	S. Emerson
1	11	276363	4464427	81	27	12:39pm	2:11pm	10/2/2012	Emerson
11	11	276116	4464608	82	28	11:56am	1:37pm	9/25/2012	S. Emerson
10	11	276322	4464410	82	28	12:58pm	2:18pm	10/2/2012	Emerson
8	11	274928	4463213	82.1	27.8	10:31am	12:07pm	8/27/2012	S. Emerson
4	11	275456	4462439	82.4	28	10:13am	11:21am	8/14/2012	Emerson
12	11	276301	4464564	84	29	12:39pm	1:53pm	9/25/2012	S. Emerson
8	11	275831	4461870	84.6	29.2	10:41am	11:46am	8/14/2012	Emerson
7	11	275902	4464777	**85**	**29**	11:49am	1:30pm	9/25/2012	S. Emerson
5	11	276111	4464750	**85**	**29**	11:25am	12:36pm	10/1/2012	Emerson
12	11	274963	4462857	85.1	29.5	10:50am	10:46am	8/28/2012	S. Emerson
12	11	276138	4464706	**86**	**30**	11:30am	12:40pm	10/1/2012	Emerson
12	11	275166	4462966	86.1	30.1	9:35am	11:07am	8/14/2012	Emerson
4	11	276179	4464767	**87**	**30**	11:20am	12:29pm	10/1/2012	Emerson
9	11	276251	4464708	**91**	**33**	11:38am	12:45pm	10/1/2012	Emerson
7	11	276266	4464447	92	33	1:26pm	2:28pm	10/2/2012	Emerson
6	11	276163	4464849	**93**	**33**	11:06am	12:20pm	10/1/2012	Emerson
8	11	276292	4464459	94	34	12:26pm	2:06pm	10/2/2012	Emerson
3	11	276221	4464778	**95**	**35**	11:15am	12:24pm	10/1/2012	Emerson
5	11	276318	4464551	96	36	11:48am	1:42pm	10/2/2012	Emerson
10	11	276295	4464524	96	35	10:15am	11:37am	10/3/2012	Emerson
13	11	276292	4464427	97	36	1:17pm	2:23pm	10/2/2012	Emerson
13	11	276301	4464635	**98**	**36**	12:26pm	1:41pm	9/25/2012	S. Emerson
10	11	276274	4464485	**100**	**38**	12:49pm	1:58pm	9/25/2012	S. Emerson
8	11	276289	4464497	**100**	**38**	10:49am	11:58am	10/3/2012	Emerson
3	11	276345	4464472	**101**	**38**	12:15pm	2:02pm	10/2/2012	Emerson
13	11	276293	4464481	**104**	**40**	11:21am	12:17pm	10/3/2012	Emerson
12	11	276299	4464499	**105**	**40**	10:43am	11:56am	10/3/2012	Emerson
3	11	276284	4464512	**108**	**42**	10:38am	11:50am	10/3/2012	Emerson
9	11	276314	4464504	**112**	**44**	10:56am	12:01pm	10/3/2012	Emerson
9	11	276311	4464481	**115**	**46**	11:13am	12:14pm	10/3/2012	Emerson
8	11	276329	4464544	**116**	**47**	11:46am	12:54pm	10/1/2012	Emerson
11	11	298369	4411772	**118**	**48**	11:38am	1:39pm	10/2/2012	Emerson
5	11	276327	4464494	**118**	**47**	11:03am	12:07pm	10/3/2012	Emerson
7	11	276303	4464590	**125**	**51**	11:52am	1:02pm	10/1/2012	Emerson
12	11	276268	4464523	**128**	**53**	12:04pm	1:54pm	10/2/2012	Emerson
6	11	276279	4464524	**133**	**56**	10:32am	11:47am	10/3/2012	Emerson
1	11	276285	4464547	**137**	**58**	10:07am	11:34am	10/3/2012	Emerson
9	11	276327	4464466	**153**	**67**	12:19pm	2:04pm	10/2/2012	Emerson
4	11	276292	4464531	**164**	**73**	11:59am	1:49pm	10/2/2012	Emerson
7	11	276278	4464547	**174**	**79**	10:00am	11:32am	10/3/2012	Emerson
11	11	276332	4464487	**177**	**80**	11:07am	12:11pm	10/3/2012	Emerson
11	11	276327	4464483	**182**	**83**	12:00pm	1:11pm	10/1/2012	Emerson

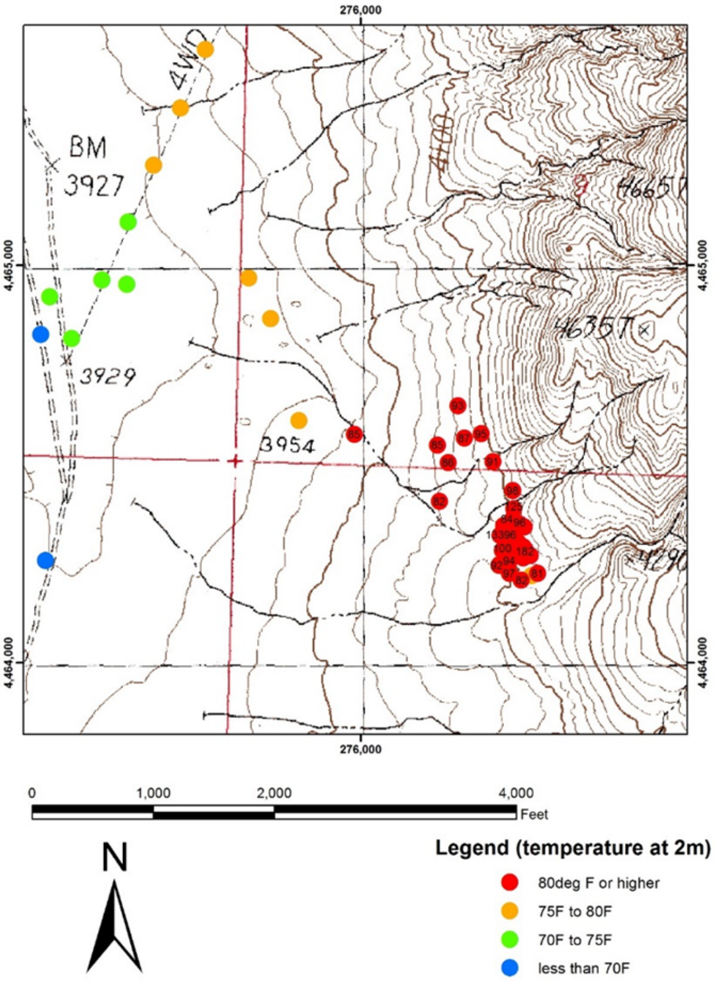

Figure 28. Location map of the 2012 shallow 2 meter temperature data showing the "oblong" thermal anomaly at the base of the eastern hills.

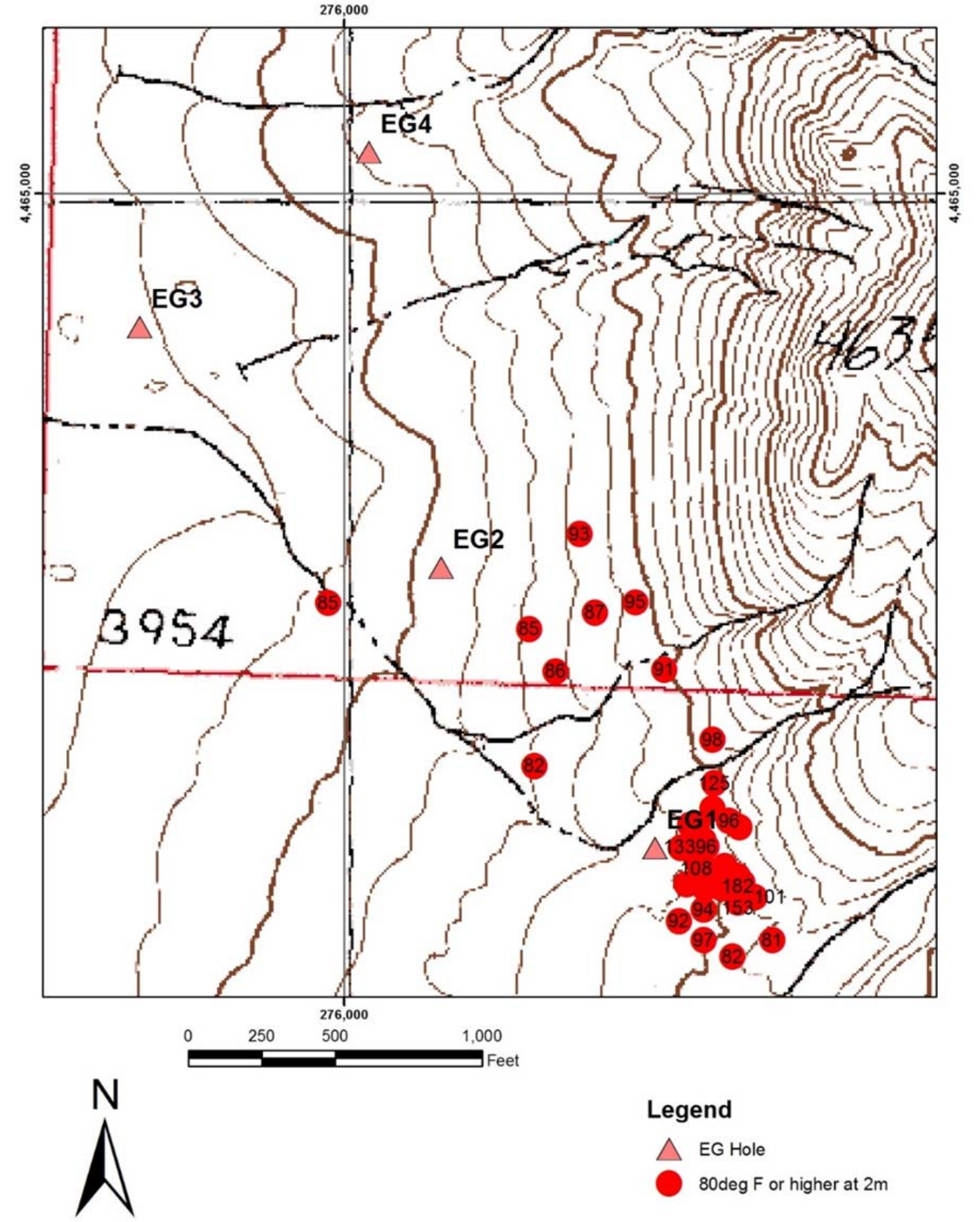

Figure 29. Location map showing shallow 2 meter data with temperatures of 80 degrees Fahrenheit or higher and four temperature gradient holes drilled in 2013.

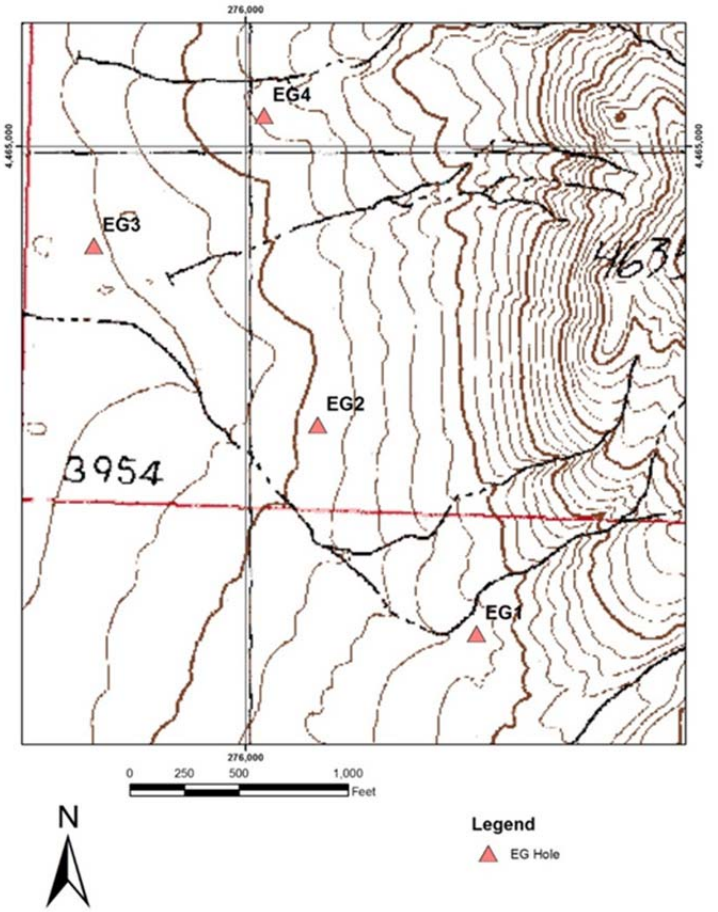

Figure 30. Location of temperature gradient wells in Emerson Pass.

line temperature of 127^{0}F. EPTG4 was drilled with air to a total depth of 165 feet with a maximum flow line temperature of 77^{0}F. All the wells were completed with 2 inch tubing to total depth with hole plug in the annulus from TD to the surface. Water was added to the tubing and allowed to equilibrate for temperature logging. The first temperature logs were acquired while the final well was being drilled. Another set of temperature logs were acquired 2 weeks after being drilled when the wells had time to equilibrate.

Figure 31 and Table 7 show the temperature profile for all four gradient holes. The well with the highest temperature was EPTG2. ETPG1 intersected a fault zone and was terminated after several loads of mud did not allow returns to flow. The charts below show the temperature gradients of each well in ^{0}C. Note the isothermal gradient in EPTG1 and EPTG2 at 100 to 150 feet. Lithology logs are still being completed along with the siting for the next gradient well. We will be looking into geophysics to enhance our knowledge of this geothermal site.

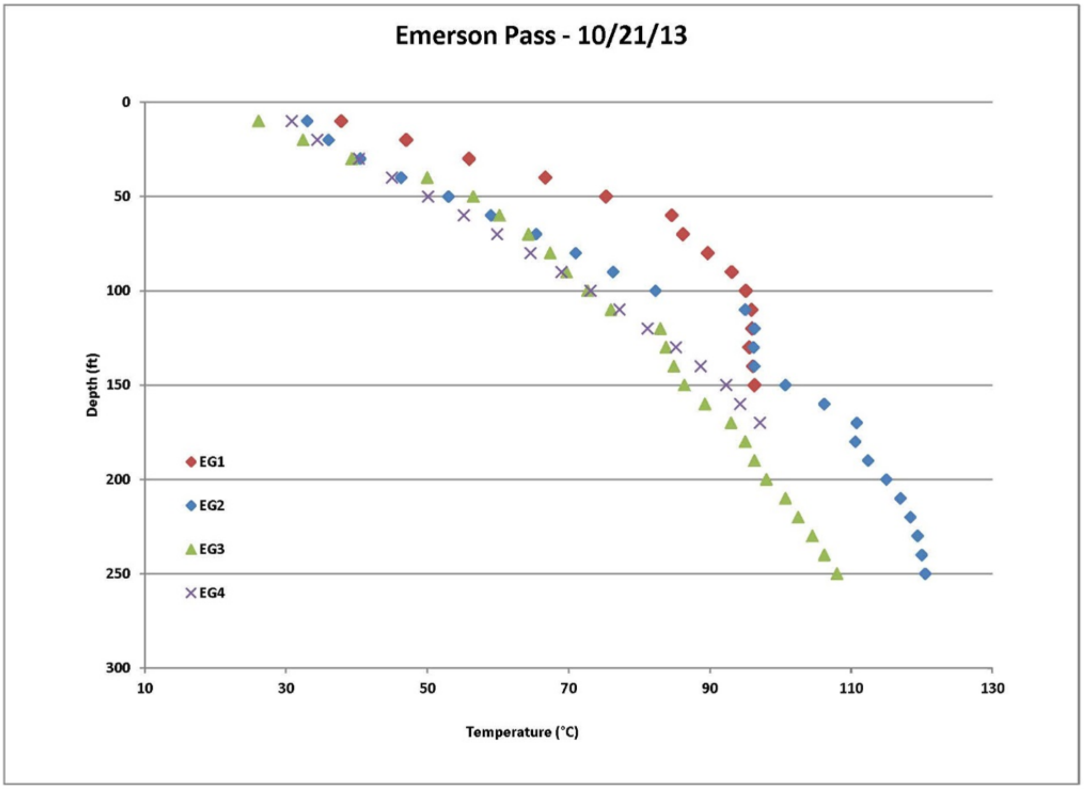

Figure 31. Temperature profiles in the temperature gradient wells in Emerson Pass.

Table 7. Temperature data from four shallow temperature gradient holes drilled in 2013

		EG1	EG2	EG3	EG4
Depth (ft)	Depth (m)	Temp C	Temp C	Temp C	Temp C
10	3.048	37.8	33	26.1	30.8
20	6.096	47	36	32.4	34.4
30	9.144	55.9	40.5	39.3	40.3
40	12.192	66.7	46.3	50	45
50	15.24	75.3	53	56.5	50.1
60	18.288	84.6	59	60.2	55.2
70	21.336	86.2	65.4	64.3	59.9
80	24.384	89.7	71	67.4	64.6
90	27.432	93.1	76.3	69.7	69
100	30.48	95.1	82.3	72.7	73.1
110	33.528	95.9	95	76	77.2
120	36.576	96	96.3	83	81.2
130	39.624	95.6	96.2	83.8	85.2
140	42.672	96.1	96.3	84.9	88.7
150	45.72	96.3	100.7	86.4	92.3
160	48.768		106.2	89.3	94.3
170	51.816		110.8	93	97.1
180	54.864		110.6	95	
190	57.912		112.4	96.3	
200	60.96		115	98	
210	64.008		117	100.7	
220	67.056		118.4	102.5	
230	70.104		119.4	104.5	
240	73.152		120	106.2	
250	76.2		120.5	108	

Geologic Mapping

Geologic mapping was carried out throughout the Pyramid Lake Paiute Reservation in order to assess the geothermal potential of tribal lands. This work was conducted by James Faulds and several graduate students and research scientists under his supervision, including Ryan Anderson, Nick Hinz, Brett Mayhew, and Greg Dering. The geologic mapping included three major components: 1) additional detailed mapping (1:24,000 scale) in the Astor Pass area building on previous efforts by Vice (2008), 2) detailed mapping (1:24,000 scale) of the Emerson Pass area in the northeastern part of the reservation (Anderson *et al.*, 2013), and 3) completion of a geologic map of the entire reservation at 1:100,000 scale (Faulds *et al.*, unpublished), incorporating previous work and mapping completed under this project. Preparation of the geologic map of the reservation required compilation of previously completed detailed geologic mapping in the area, including digitization of some maps (e.g., Ressel, 1996), and merging of all maps into one geodatabase. In addition, reconnaissance mapping was carried out in parts of the reservation not previously mapped. Each of these components is described separately below.

Astor Pass Area

Detailed mapping was completed of several square kilometers directly west of Astor Pass in order to better understand the kinematic evolution of the faults in the Astor Pass area. This mapping built on previous efforts by Vice (2008). This mapping showed that the area west of Astor Pass contains a major middle Miocene volcanic complex, which includes large basaltic andesite and rhyolite domes. Unusually thick (tens of meters) basaltic andesite and andesite lavas characterize this area. The massive and thick flows and domes in this area contrast with the more typical layer-cake stratigraphy, including thin (generally < 10 m) basaltic andesite flows to the east and north of Astor Pass. Initially, we considered the possibility that the significant contrast in stratigraphy across Astor Pass may result from appreciable strike-slip offset. However, we found no evidence for major strike-slip offset, although a small rhyolite dome directly east of Astor Pass appears to be offset ~600 m in a dextral sense. We therefore concluded that the Astor Pass area corresponds to the northeastern margin of a major middle Miocene volcanic center. The Astor Pass fault zone may have developed along the margin of this volcanic center due to the mechanical contrast between the more massive domes and subsurface intrusions to the west and more layer-cake strata to the east. Because the new mapping in this area essentially straddled the reservation boundary and extended slightly west of the boundary, we did not compile at 1:24,000 scale but rather incorporated into the 1:100,000 reservation-wide map.

In addition to the new mapping, significant effort was devoted to interpreting 16 seismic reflection profiles in the Astor Pass area and analyzing cuttings from the APS-2 and APS-3 wells (Mayhew, 2013). The seismic reflection data revealed the presence of a major previously unrecognized, east-dipping normal fault on the west side of Astor Pass, as well as several additional minor faults in the area. The seismic reflection and well data were incorporated into several cross sections used to construct the 3D model of Astor Pass (Mayhew, 2013). Figure 32 shows a new fault map for the Astor Pass area, which includes the traces of many subsurface faults observed on the seismic reflection profiles.

Emerson Pass Area

On the basis of a thermal anomaly identified with a 2-m shallow temperature survey (Kratt *et al.*, 2007; PLPT, unpublished data), a cluster of tufa mounds, and favorable structural setting, the Emerson Pass area in the northeastern part of the reservation was selected for detailed study. As part of his Master's thesis, Ryan Anderson mapped ~204 km^2 in this area (Figure 33) in order to analyze the stratigraphic and structural framework and vector into the potential location of a blind geothermal system, including identifying targets for temperature-gradient drilling (Anderson, 2013).

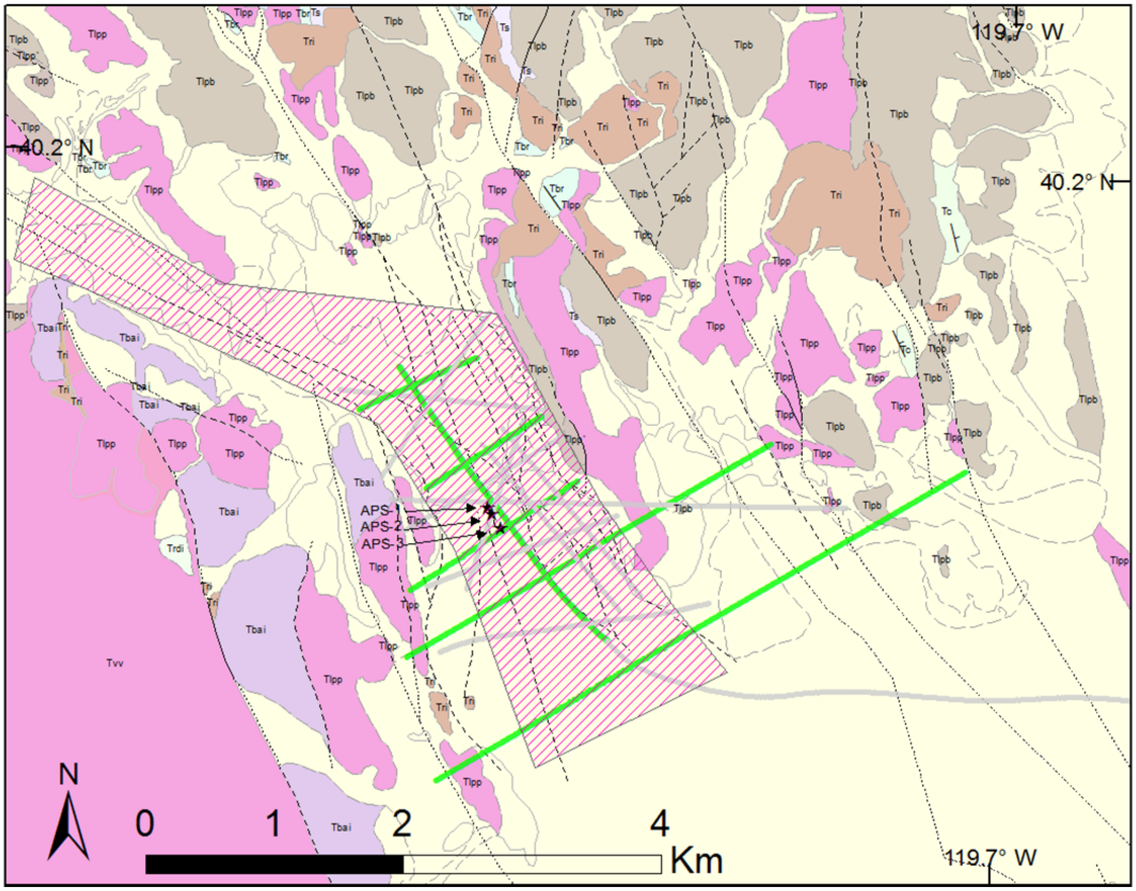

Figure 32. Simplified geologic map of the Astor Pass region, showing a myriad of faults in the Astor Pass graben. Many of these faults were identified in this study through interpretation of seismic reflection profiles. Brown, pink, purple, and gray units are Tertiary volcanic and sedimentary rocks. Yellow units are Quaternary alluvium, tufa, and other sediments. Green lines show locations of seismic reflection profiles used in the 3D model. Hatched area shows extent of Astor Pass. Stars in the middle of Astor Pass show locations of the APS wells (modified from Vice, 2008).

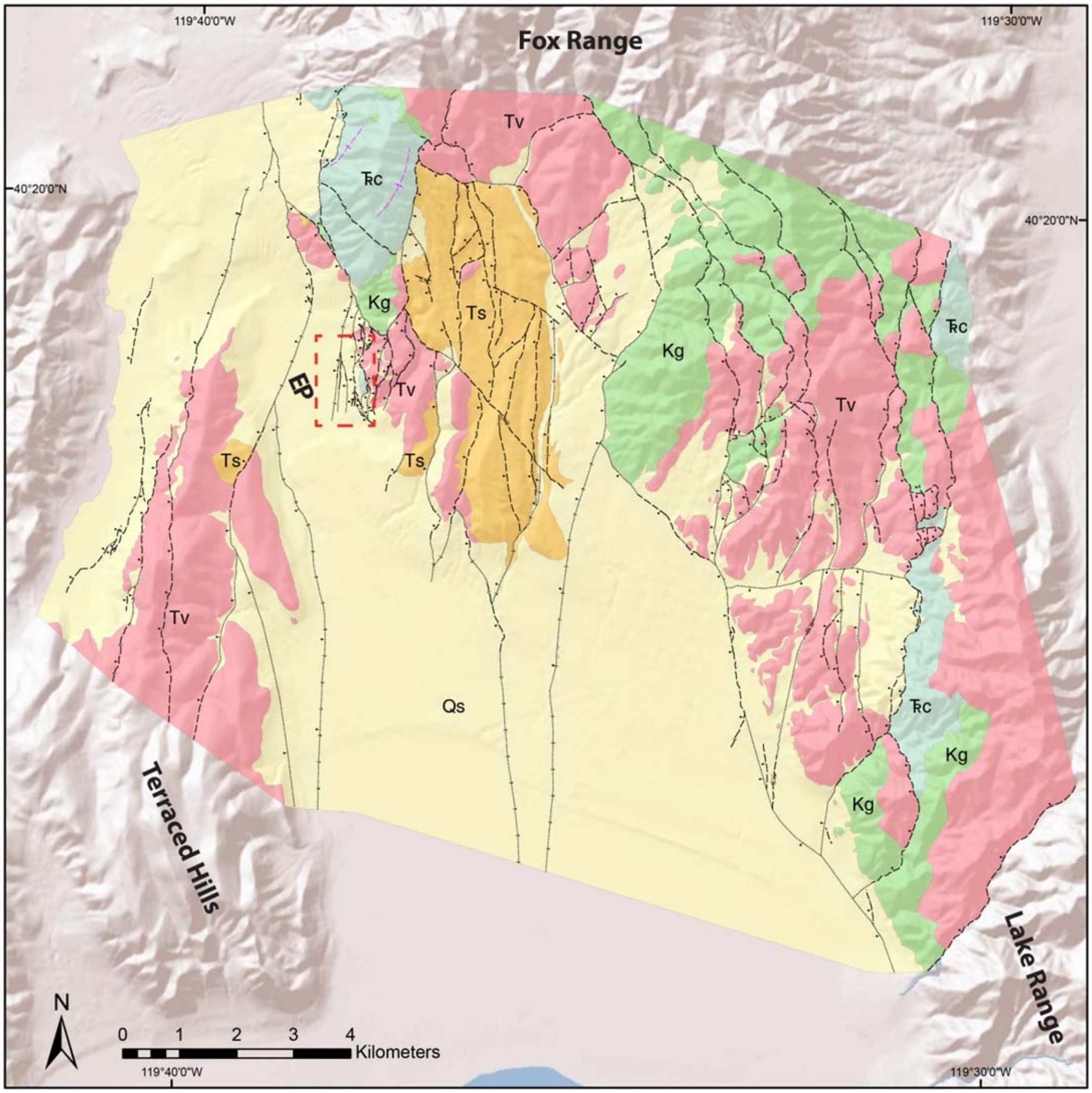

Figure 33. Simplified geologic map of the central Lake Range, southern Fox Range, and northern Terraced Hills (from Anderson, 2013). EP, Emerson Pass. Rock units from youngest to oldest: Qs, Quaternary sediments; Ts, Tertiary sediments and sedimentary rocks; Tv, Tertiary volcanic and volcaniclastic rocks; Kg, Cretaceous granitic intrusions; TRc, Triassic-Jurassic Cottonwood Canyon formation. Geothermal area highlighted by the red dashed box. Faults shown with ball and bar on the downthrown side. Detailed geologic map was published by the Nevada Bureau of Mines and Geology (Anderson *et al.*, 2013).

The detailed geologic mapping and stratigraphic-structural analyses elucidated the kinematics, stress state, and structural controls of a probable "blind" geothermal system in the Emerson Pass area. The area resides near the boundary of the Basin and Range and Walker Lane provinces of northwestern Nevada, at the northeast end of Pyramid Lake. Strata of the surrounding Fox Range, Lake Range, and Terraced Hills are comprised of late Miocene to Pliocene sedimentary rocks and the middle Miocene Pyramid sequence volcanic rocks, all overlying Cretaceous granitic intrusions and Triassic to Jurassic metasedimentary rocks.

The active geothermal system, as expressed by a 2-m shallow temperature thermal anomaly (maximum ~60°C), lies at the western edge of a broad left step at the northeast end of Pyramid Lake between the north- to north-northeast-striking, west-dipping, Fox and Lake Range normal faults. The 2-m temperature surveys defined a north-south elongate thermal anomaly that resides on a north- to north-northeast-striking normal fault. Additionally, travertine mounds, chalcedonic silica veins, and silica cemented Pleistocene lacustrine gravels in the Emerson Pass area were discovered through the mapping and indicate a robust geothermal system active at the surface in the recent past, likely the early Holocene. Structural complexity and spatial heterogeneities of the strain and stress field have developed in the step-over region, but kinematic data suggest a west-northwest-trending (~280° azimuth) extension direction. The Emerson Pass geothermal system likely results from enhanced permeability generated by the intersection of two oppositely dipping, southward terminating north- to north-northwest-striking (Fox Range fault) and north-northeast-striking normal faults. Our work at Emerson Pass has been released in a GRC paper (Anderson and Faulds, 2013), as well as an NBMG geologic map (Anderson *et al.*, 2013).

Pyramid Lake Reservation Geologic Map

A digital geologic map at 1:100,000 scale was completed for the entire PLPT Reservation (Figure 34). The map was compiled to facilitate assessment of the geothermal potential of the reservation, particularly with respect to identifying favorable structural settings for geothermal activity. Compilation of the map involved 1) digitization of a previously completed map of the central Lake Range (Ressel, 1996), 2) merging of several preexisting maps (Faulds *et al.*, 2003, 2005, 2007, 2008; Bell *et al.*, 2003a, b, 2004; Garside *et al.*, 2003; Delwiche, 2007; Drakos, 2007; Vice, 2008; Drakos and Faulds, 2013; Anderson *et al.*, 2013) into one geodatabase, 3) new reconnaissance mapping of bedrock and Quaternary geology of >300 km^2 of previously unmapped parts of the reservation, including the Smoke Creek Desert area, much of the central Lake Range, northern Pah Rah Range, and parts of the Virginia Mountains and Fox Range; 4) significant edge-mapping between the various maps; and 5) development of a comprehensive, coherent reservation-wide stratigraphy. The new reconnaissance mapping required substantial amounts of field work and aerial photo interpretation, largely completed in the last year of the project. In addition to completing the 1:100k geologic map of the entire reservation, previously completed mapping in the southern Lake Range was revised, updated, and released as an NBMG open-file report (Drakos and Faulds, 2013).

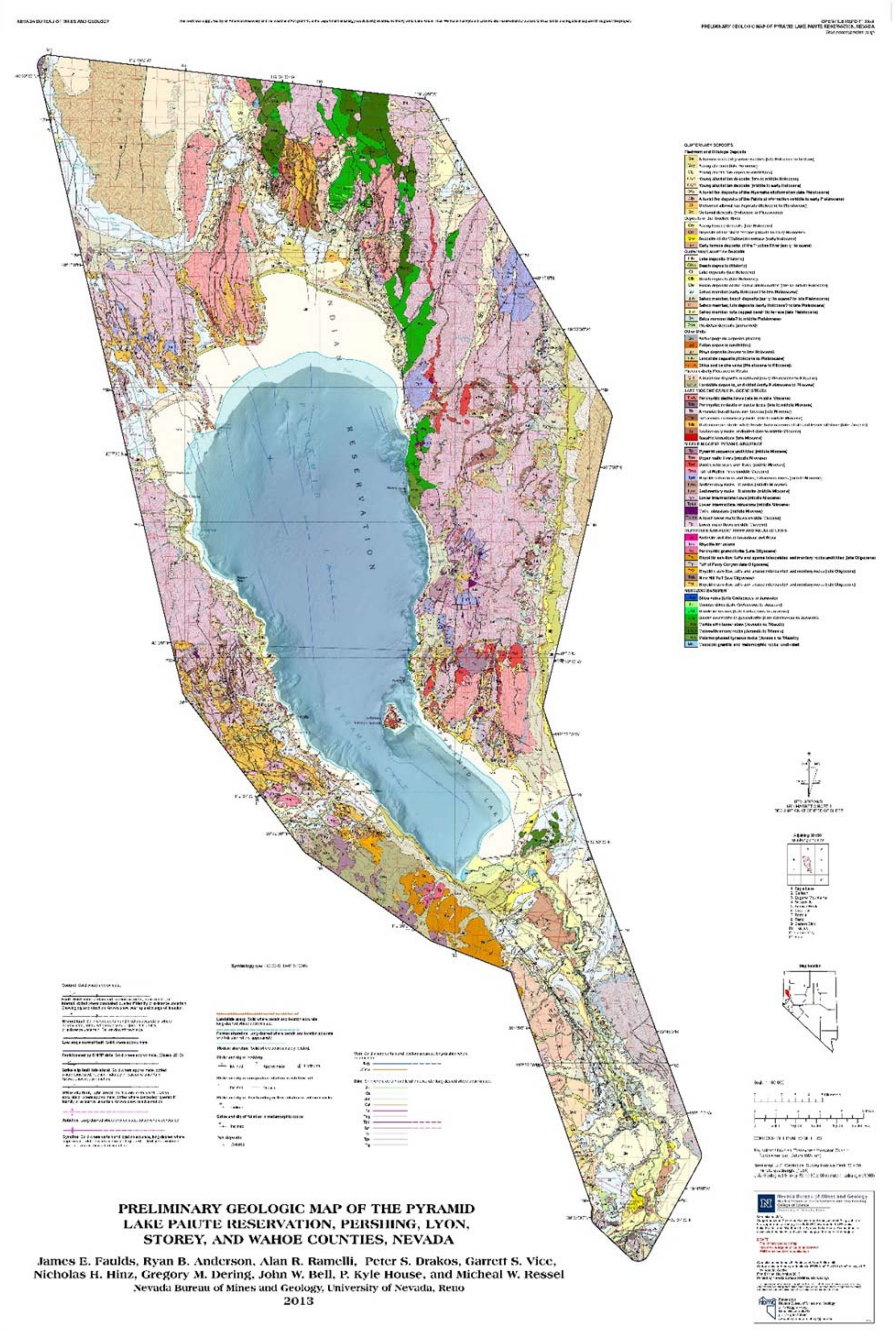

Figure 34. Geologic Map of the Pyramid Lake Paiute Reservation (1:100,000 scale). All data reside in the same ArcGIS geodatabase.

Major discoveries resulting from the new mapping and compilation include the following:

- Recognition of a large felsic volcanic center in the northeastern part of the reservation in the northern Lake Range.
- Identification of several large landslide deposits on the eastern flank of the Lake Range and northeastern part of the Pah Rah Range; some of these landslides show evidence of recent activity.
- Discounting the hypothesis of a major east-dipping antithetic fault zone on the east side of the Lake Range, which had been considered as a possible control of warm springs in the area; scarps in this area are primarily erosional and generally represent Lake Lahontan shorelines rather than fault scarps.
- Recognition of several northerly striking Holocene normal faults in the southern part of the Smoke Creek Desert; these faults may connect southward with faults cutting the Terraced Hills.
- Documenting major west-dipping, N- to NNE-striking Quaternary normal faults in the southern part of the San Emidio Desert and San Emidio Canyon; these faults link southward with the major range-front fault along the west flank of the Lake Range.
- Identification of several previously unrecognized exposures of Mesozoic basement rocks in the northern Lake Range and southern Fox Range.

The geologic map of the PLPT Reservation facilitates both analysis of geothermal potential and identification of possible localities for blind geothermal systems. Fault patterns, including favorable settings for geothermal activity such as step overs and fault terminations, can be readily identified at this scale (see discussion in Section 4.3). Although small and difficult to recognize at the 100k scale, tufa mounds are distinguished on the map. They can be easily found and highlighted in the geodatabase, which may be important for geothermal exploration, as tufa mounds can serve as a proxy for a blind geothermal system. Because the geologic map is a digital ArcGIS product, other layers, such as shallow temperature surveys, well locations, and soil gas data, can ultimately be added to facilitate geothermal exploration and development.

ANDERSON BAY GEOPHYSICAL ANALYSIS

Introduction

Pyramid Lake is located within the Walker Lane Belt (WLB) system. The WLB system consists of strike-slip and normal faults nearly parallel to the San Andreas Fault system (Briggs & Wesnousky, 2004). The fault system within Pyramid Lake contains the right-lateral Pyramid Lake fault and the Lake Range fault, a west-dipping range-front normal fault along the East Shore of Pyramid Lake (Eisses *et al.*, 2012).

Eisses *et al.* (2012) studied the fault locations and geometries in and around Pyramid Lake. They constrained the Lake Range fault found on the eastern edge of Pyramid Lake. This fault nomenclature will be used for the remainder of this report. The Lake Range fault has an average strike of N4˚W and is located primarily within the Lake. Tufa trends near the shore of the Lake suggest the presence of this fault. The location and geometry of the Lake Range fault is shown in Figure 35.

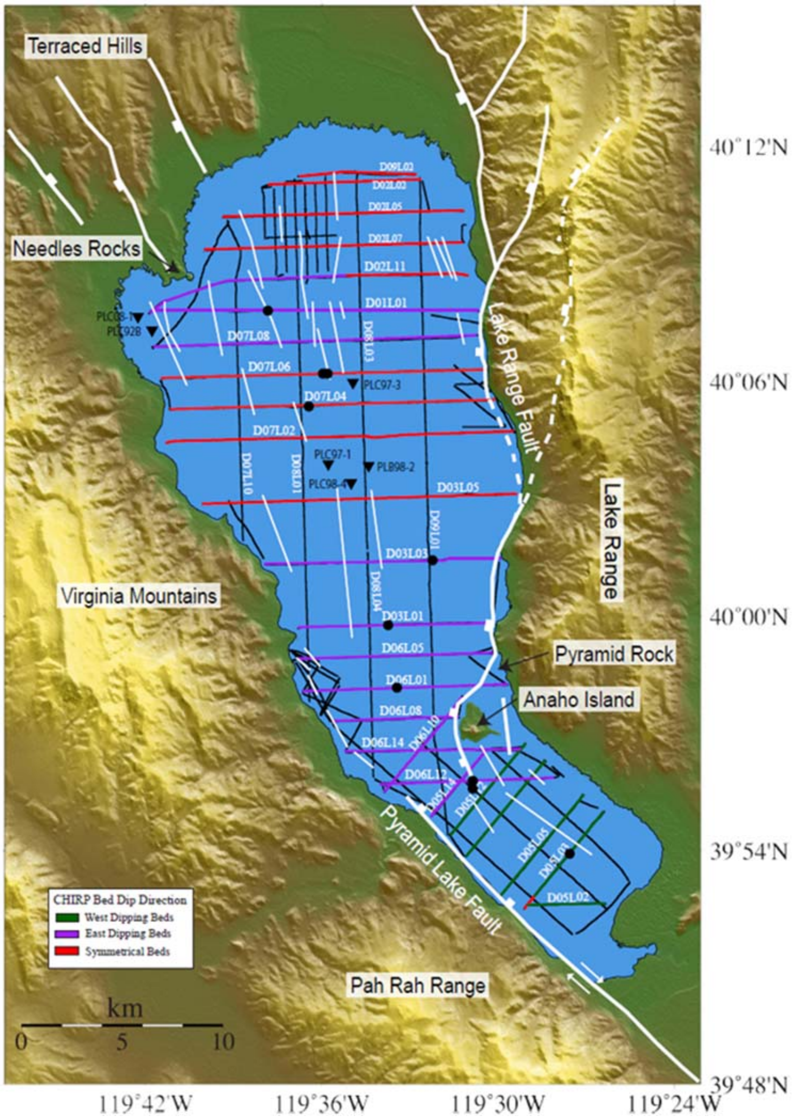

Figure 35. Map denoting the location of the Lake Range Fault (from Eisses, 2012).

Figure 35 depicts the location of the fault found with Compressed High Intensity Radar Pulse (CHIRP) seismic profiling. The Lake Range fault trace is a white line. The fault may bifurcate into the Lake Range at Anderson Bay (AB), denoted with “1”, and at Fox Bay, “2”. Eisses *et al.* (2012) stated it was possible to produce a comprehensive fault map of the Pyramid Lake region, including the faults located beneath the lake, as well as how they connect to mapped faults on land. This includes the continuation of the Lake Range fault from the Lake and through Anderson Bay.

Methods

In collaboration with the Pyramid Lake Paiute Tribe (PLPT), Nevada Seismological Laboratory student employees at the University of Nevada, Reno (UNR) conducted high-resolution magnetic surveys, six refraction microtremor arrays, and one seismic refraction/reflection array to characterize the continuation of the Lake Range fault on land.

Magnetic Survey

Magnetic data collected in the Anderson Bay area were of two survey types: one roving GEM magnetometer with another stationary GEM magnetometer as the base station, and an Apple iPhone 3GS with the xSensor Pro app from Crossbow Inertial Systems. The GEM base station measures diurnal variation of the Earth's magnetic field to remove this variation from the rover data during processing, and to provide an average value for the base-level magnetic field for the survey. The rover took readings at spacing's of about 50 meters, but tightened to as small as 10 meters in areas that indicated anomalies. The base station magnetometer collected 30-second time sampling data for the three-day survey covering roughly a 2.6 km^2 (1 mi^2) area. Data from the GEM system magnetometer is shown in figure 36.

Additionally, the iPhone data were collected in one day over a 2 km^2 (.4 mi^2) area. The xSensor Pro app collected data, time, and GPS position along with the three magnetic components of the iPhone's Hall-effect sensor. The GEM system functioned as a base station that recorded the diurnal variation of the magnetic field, and recorded any anomalies. A separate handheld GPS unit recorded locations and time for the GEM system measurements. Both surveys utilized NAD83 UTM Zone 11N metric coordinates, established by hand-held Garmin eTrex 20 GPS unit.

Magnetic data processing was conducted using Geosoft's Oasis Montaj. Magnetic mobile, base, and GPS datasets were imported and cross-correlated for correction and total magnetic intensity profiling.

Refraction Microtremor (ReMi)

The refraction microtremor method (Louie, 2001; Scott *et al.*, 2004) was utilized to collect Rayleigh wave data and calculate shear wave velocities for site classification purposes. A series of northwest-southeast trending arrays as well as one north-south, shoreline-bounded array were collected at Anderson Bay. The line geometry was intended to cross the hypothesized onshore fault splay perpendicularly.

The Bison seismograph was employed as the data-receiving unit to collect and save data. Twelve vertical geophones were attached and leveled at 10 m increments to the 110-m-long array. Each vertical geophone worked at 4.5 Hertz. As a source, a 16 lb. sledgehammer was struck onto a square, steel plate located several meters off the end of the line.

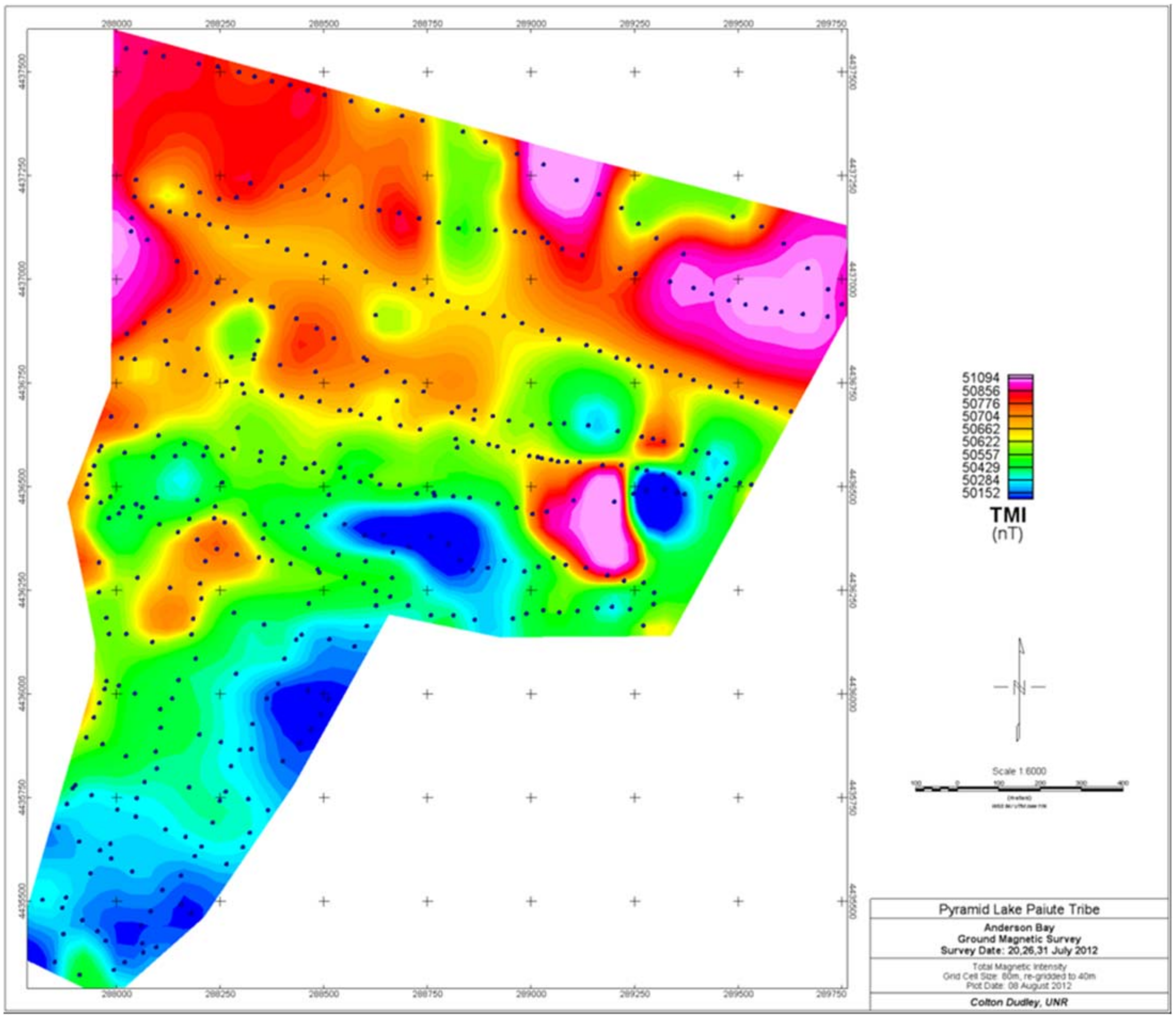

Figure 36. The GEM system magnetic map contoured in Oasis Montaj.

To process the data, p-f plots were filtered and combined for all data sets recorded from the same array location using SeisOpt® ReMi™ (© 2012 Optim). If a p-f plot appeared to have poor resolution, it was not included in the combined p-f plot. Minimum velocity picks were chosen and saved. Utilizing ReMiDisper®, velocity profiles were modeled.

Seismic Reflection and Refraction

The near-surface seismic reflection and refraction survey utilized a seismic cable with 48 channels and 3 m takeout spacing. Geophone arrays of six geophones over 4 m were used at each takeout and distributed parallel along the receiver array. Wave propagation was initiated at each takeout by striking a 16 lb. sledgehammer against a square, steel plate ten times, recorded by a 48-channel Bison Galileo-21 unit. A total of 10 hammer hits were collected for each geophone totaling 48 records. The array length is approximately 150 m.

Seismic processing included John Louie's JRG (Resource Geology Seismic Processing System for Java from crack.seismo.unr.edu/jrg) software. Geometry was then applied to the seismic array dataset and was processed by filtering, picking first seismic wave arrivals, and stacking data to achieve a stratigraphic cross section of each seismic line. First seismic wave arrivals were processed by SeisOpt® @2D™ (© 2012 Optim) for a color contour gridded velocity section of each seismic line in order to obtain velocities.

Results

Magnetic Survey

The magnetic survey consisted of two surveys: the GEM magnetometer system and the iPhone data. The GEM system magnetic data contoured in Oasis Montaj is shown in Figure 36 and the iPhone magnetics data is shown in figure 38.

The ground magnetic data were collected on July 20, 26, and 31 of 2012. The color contour map shows the total magnetic intensity values of the area recorded within Anderson Bay. The values range from 50,152 nT and 51,094 nT where the higher values are warm colors and the low values are cool colors. The diurnal variation was minimal at 50 nT and corrections were unnecessary. The map has a grid cell size of 80 m and re-gridded to 40 m.

Furthermore, the iPhone data collected were averaged over time in Excel and contoured in the Oasis Montaj mapping program. The 10 second, and 25 second time averages of the iPhone magnetic data from the xSensor Pro app is displayed in Figure 37

The chart shows the elapsed time (sec) versus the raw magnetic field data (nT). The green values represent the total magnetic field. The red values represent the ten second average of the total magnetic field. The blue values represent the 25 second average of the total magnetic field.

The iPhone data were spatially averaged and imported into Oasis Montaj for color contour mapping. The iPhone magnetic data contoured in Oasis Montaj are shown in Figure 38.

The ground magnetic data were collected on July 20, 2012. The map covered roughly the part of the area mapped in Figure 36. The black line on the map represents the survey path. The color contour map shows the total magnetic intensity values of the area recorded within Anderson Bay. The values range from 44,473 nT and 50,809 nT, where the higher values are warm colors and the low values are cool colors.

As stated previously, the GEM magnetometer map consisted of a three day integrated data collection. The iPhone data was collected during the time of the first day of surveying with the GEM system magnetics data. Day one of the GEM system magnetic data contoured in Oasis Montaj is shown in Figure 39.

The ground magnetic data were collected on July 20, 2012. The map covered nearly the same area as the iPhone data. The points on Figure 39 essentially resemble the line path on Figure 38. The color contour map shows the total magnetic intensity values of the area recorded within Anderson Bay. The values range from 50,119 nT and 50,836 nT where the higher values represent warm colors and the low values represent cool colors. The map has a grid cell size of 25 m.

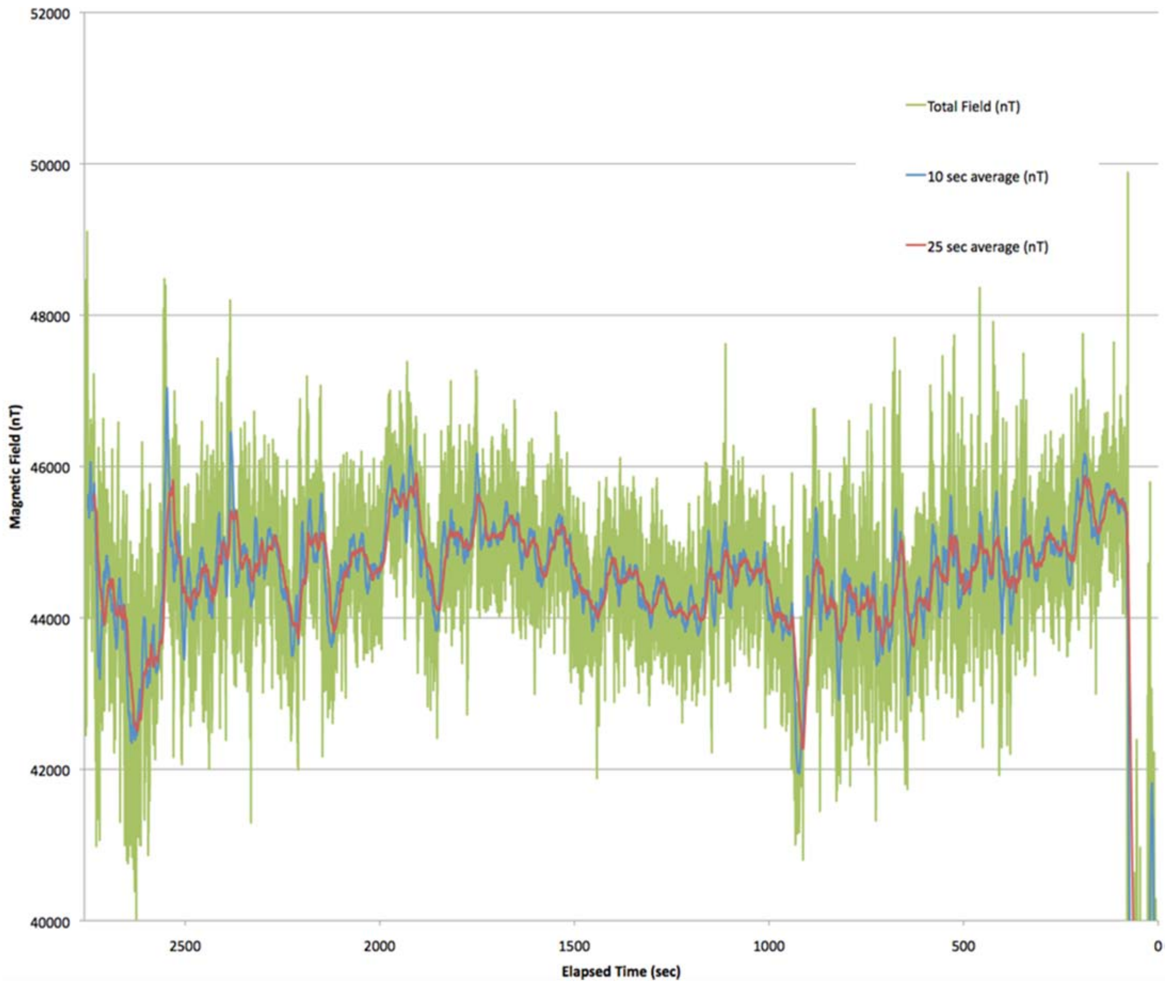

Figure 37. The magnetic data of the iPhone from the xSensor Pro app.

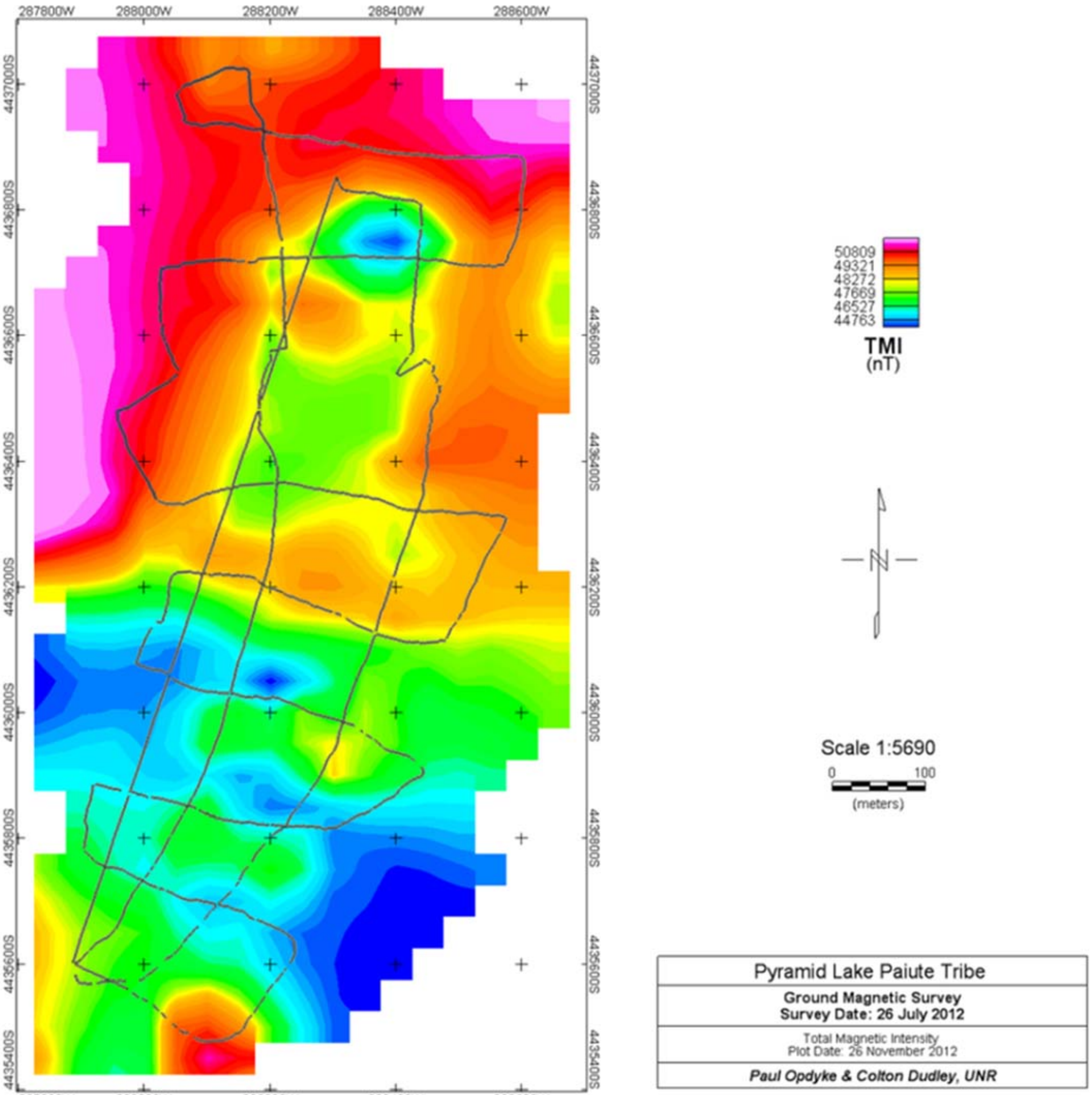

Figure 38. The iPhone magnetic map contoured in Oasis Montaj.

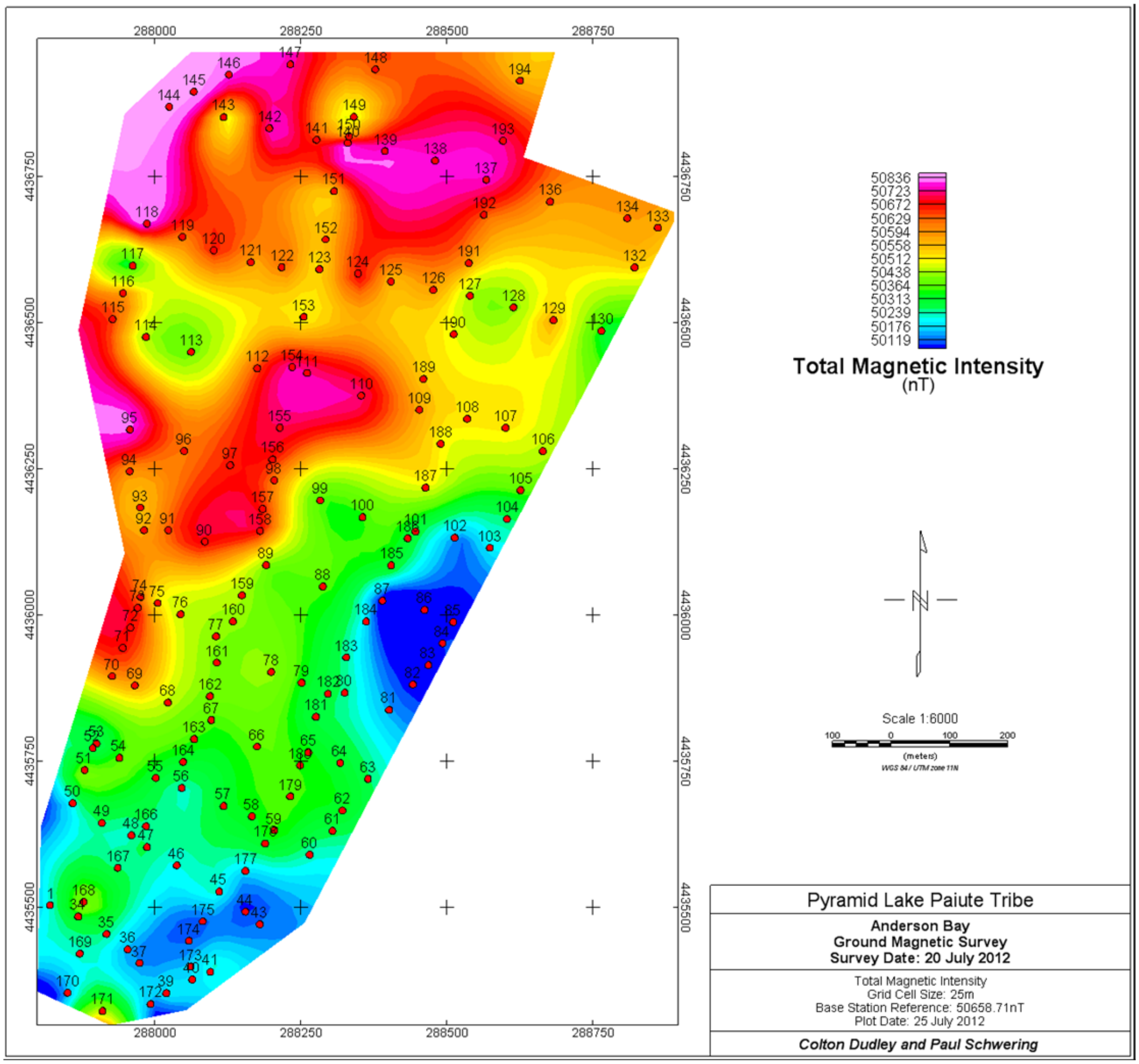

Figure 39. Day one of the GEM system magnetic map contoured in Oasis Montaj.

Refraction Microtremor (ReMi)

The refraction microtremor survey consisted of seventeen locations designed specifically for fault identification. The locations of the refraction microtremor results are shown in Figure 40.

The refraction microtremor data were collected July 26 and 31, 2012. The colors of the tags represent similar array geometry and location. The refraction microtremor arrays entailing latitude, longitude, Vs30 values, depth of measurements, and any notes concerning the arrays is shown in Table 8.

Figure 40. The locations of the refraction microtremor results tagged with their individual array name and Vs30 values (m/s). From Google Earth Pro.

Table 8. The refraction microtremor array metadata detailing latitude, longitude, Vs30 values, depth of measurements, and notes.

Array Name	Latitude	Longitude	Vs30 (m/s)	Depth of measurement (m)	Notes
TufaA	40.04392	-119.48597	769	125	
TufaB	40.04354	-119.48488	593	200	
TufaC	40.04527	-119.48374	378	200	
TufaD	40.04569	-119.48491	549	40	
ShoreA	40.05085	-119.48635	245	55	
ShoreB	40.04991	-119.48591	232	36	
ShoreC	40.04897	-119.4855			no geometry
ShoreD	40.04795	-119.48551	199	200	
ShoreE	40.04702	-119.48589	222	100	
R1A	40.05198	-119.48562	379	167	
Line2A	40.04984	-119.48494	282	50	
Line2B	40.04938	-119.48377	443	70	
Line2C	40.0491	-119.48287	442	110	partial line
R3A	40.05549	-119.48399	766	78	
R3B	40.05528	-119.4826	671	100	
R3C	40.05507	-119.48134	668	70	
R3D	40.05491	-119.48012	647	60	

ShoreC was unable to be processed due to the missing array geometry information. Line2C was a partial array. The field crew was unable to finish the array measurements. All other arrays were completed and processed for Vs30 values.

Overall, the Vs30 values decrease toward the lake. This includes R3, Line2, and both tufa arrays. The Shore array contained the lowest Vs30 value of 199 m/s at ShoreD. The most southern tufa line contained the highest Vs30 value of 769 m/s at TufaA. The Shore array had relatively no change in Vs30 values. The largest, immediate change occurred on Line2. There was a 57 percent increase from Line2A to Line2B.

Seismic Reflection and Refraction

Seismic data were intended to cross the fault zone. The array was located along the road where access was easiest. The relative location and orientation of the seismic array is shown in red in Figure 41.

The Anderson Bay refraction data were completed using Optim's SeisOpt® @2D™ package (© 2012 Optim). The results of the velocity section are shown below in Figure 42.

The seismic refraction data were collected on August 15, 2012. Refraction results were determined by picking first wave arrivals and optimizing them with Optim's SeisOpt® @2D™ package. The northeast looking section is labeled with the distance on the bottom. Notice that the section distance begins with 0 m and terminates at 140 m. This visualization is similar to the cropped section in Figure 41. The section is nearly 90 m thick. The velocities of the section range from 0 m/s to 6000 m/s, where warm colors represent higher velocities and cool colors represent lower velocities.

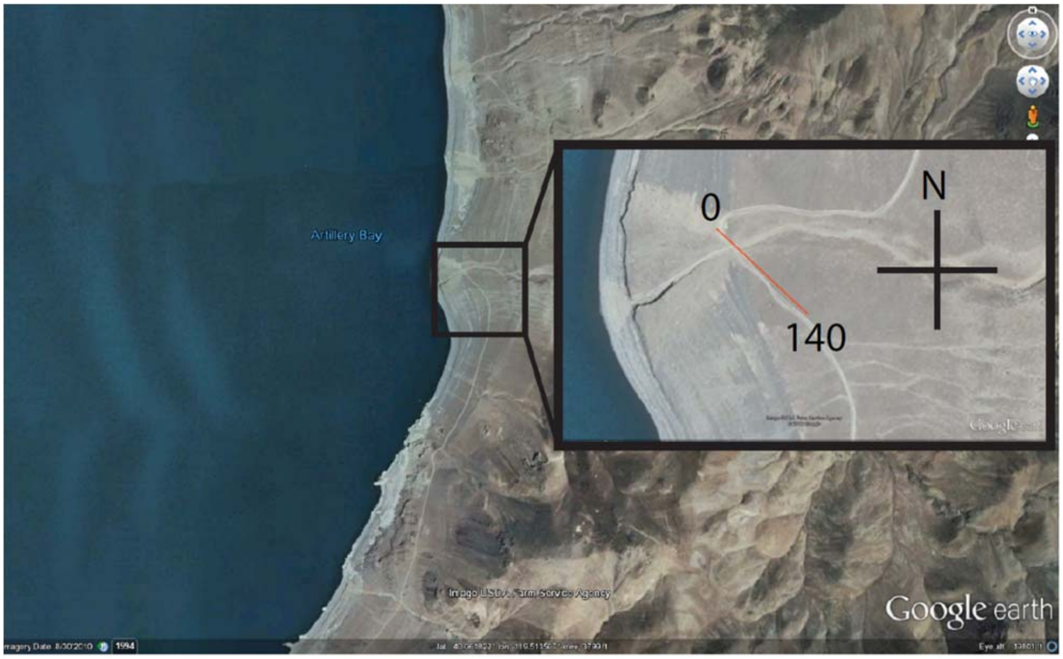

Figure 41. The relative location and orientation of the seismic line within Anderson Bay (Anderson).

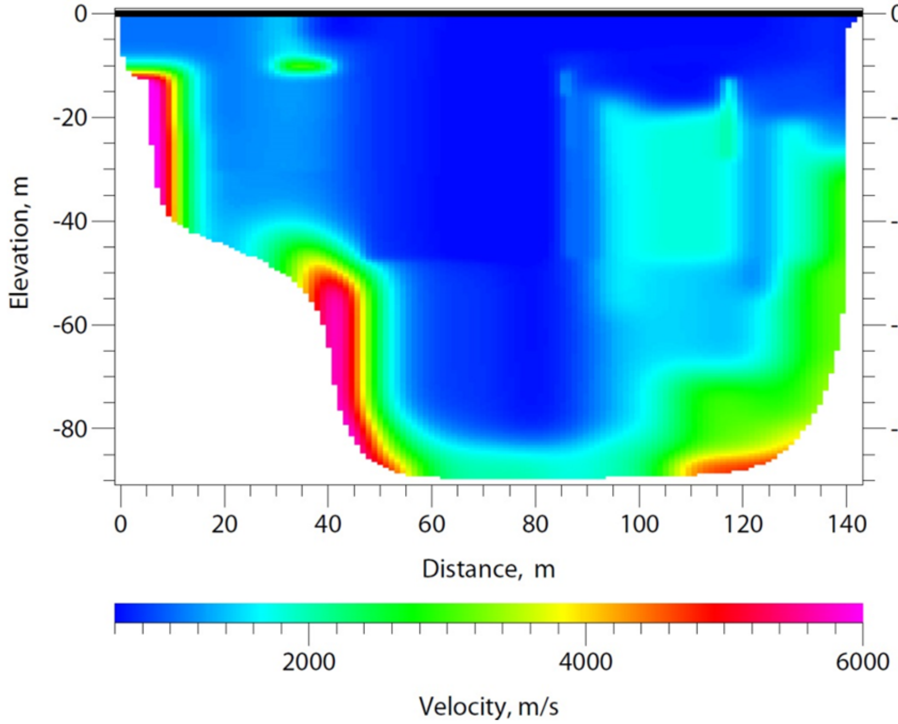

Figure 42. The velocity section of the seismic refraction results.

The seismic reflection data were processed and plotted with Dr. John N. Louie's JRG package from crack.seismo.unr.edu/jrg. The seismic reflection data plotted with the colored refraction overlaid is shown in Figure 43. Additionally, Figure 44 shows the pre stacked depth migrated reflection data with a velocity model processed by Optim overlain along with the brute stack of the reflection data on the right showing the differences between the data from rough processing to being migrated.

The reflection data were completed the same day as the refraction data on August 15, 2013. The refraction data from Figure 42 was minimized and overlaid onto the reflection data in Figure 43. The length of the section is the same length of the refraction line in Figure 41 at 140 m. Additionally, the section is a northeast looking section at approximately 160 m deep.

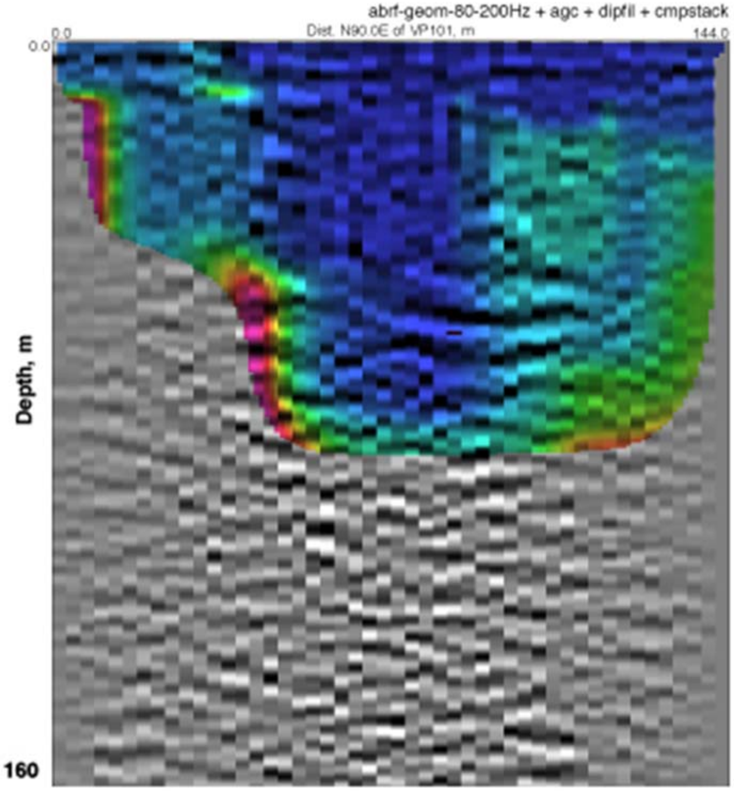

Figure 43. The black and white reflection brute stack plotted with the colored refraction velocities overlain. This section is north-looking, with west-northwest on the left and east-southeast on the right.

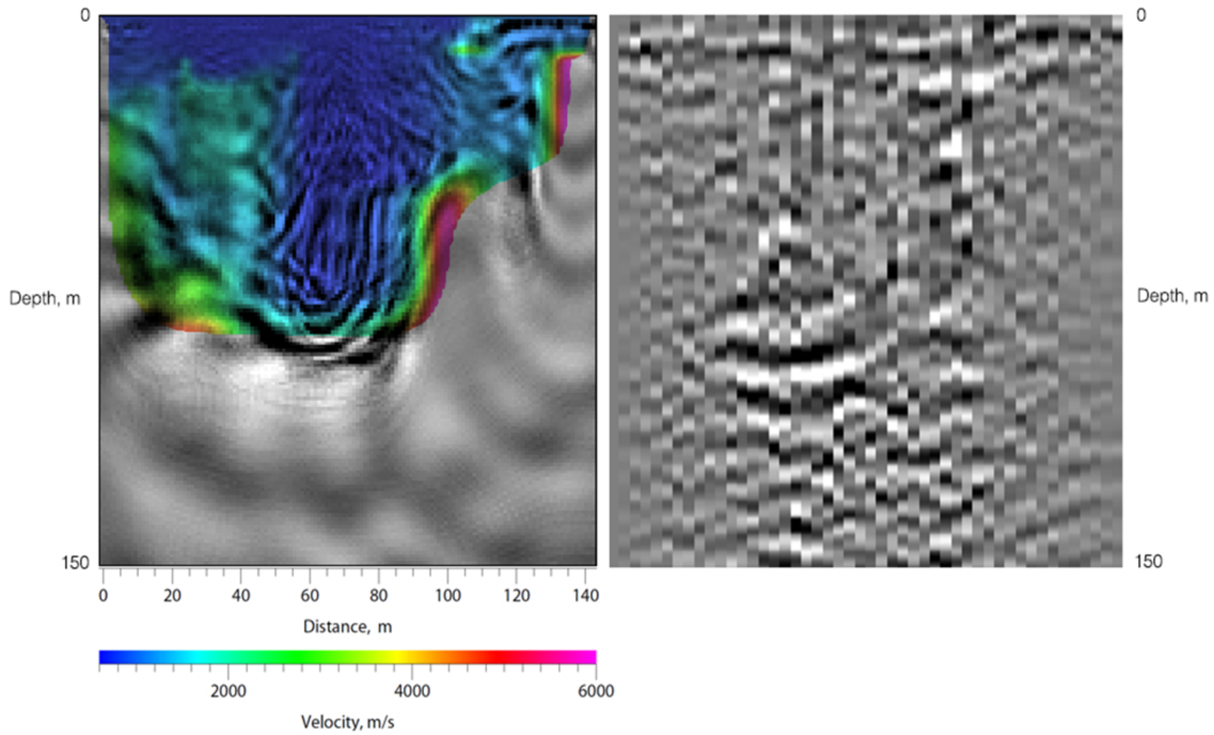

Figure 44. The prestack depth migrated reflection data with overlain velocity model, left, alongside the brute stack of the reflections, right. These sections are south-looking, with east-southeast on the left and west-northwest on the right.

Conclusions

The magnetic, refraction microtremor, and seismic refraction/reflection surveys were successful in characterizing the proposed fault structure at Anderson Bay. All three surveys performed showed data entailing the presence of steeply dipping structures.

The magnetic data from the GEM system shows an anomaly trending northwest and southeast. This regional anomaly can be seen in two areas of the magnetic data from the GEM system. Both trends show a change of 500 nT over a short distance. These two trends in the GEM magnetic data are shown in Figure 45.

The iPhone magnetic data similarly concludes the same anomaly trending northwest and southeast in Figure 42, though the anomalies were of a 2,000 nT difference in magnitude compared to the 500 nT difference with the GEM system data. The trends in the iPhone and GEM system magnetic data are shown in Figure 46.

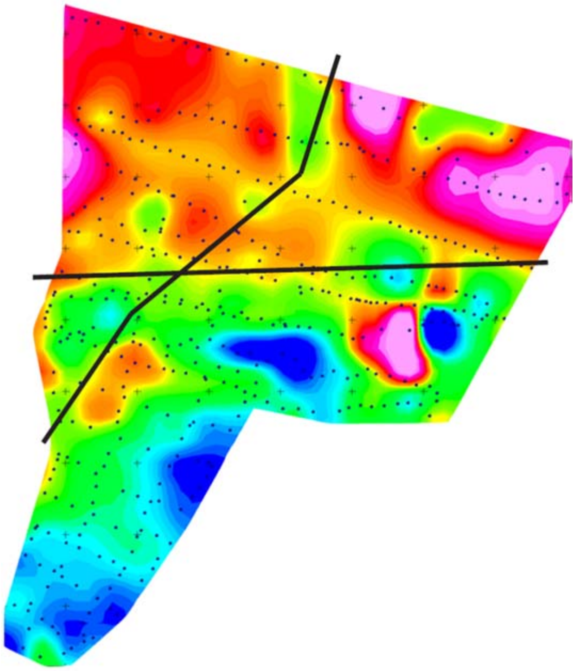

Figure 45. The two trends in the GEM system magnetic data. North is up.

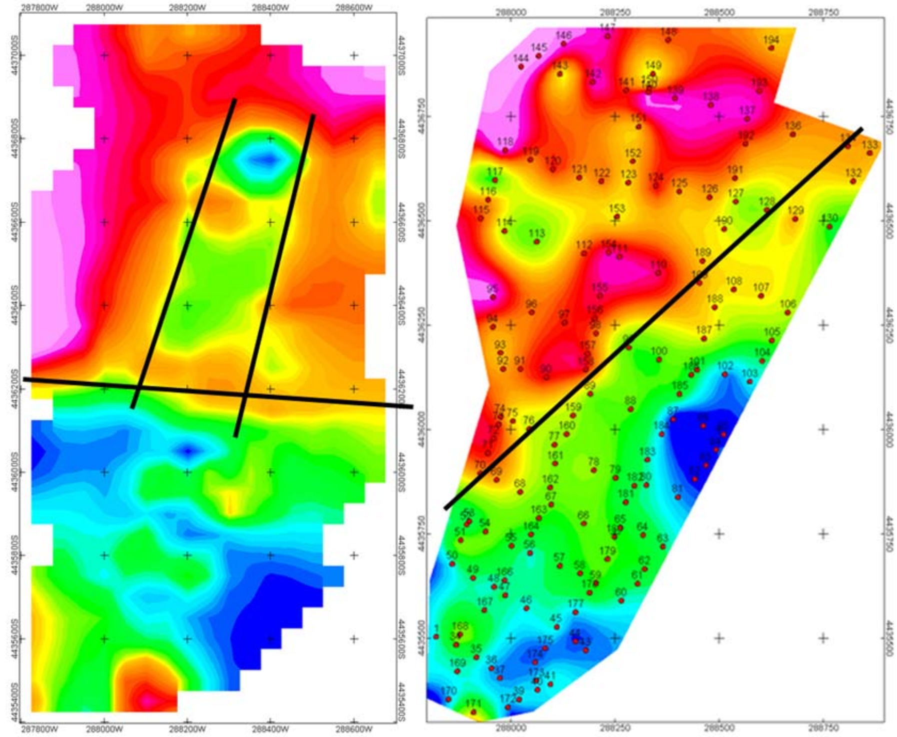

Figure 46. The trends in the iPhone magnetic data to the left and the GEM system to the right, with alternative fault interpretations, black lines.

The magnetic results from the three data sets show a general northeast and southwest anomaly. The collection of all three magnetic data sets with Google Earth imagery are shown below in Figure 47.

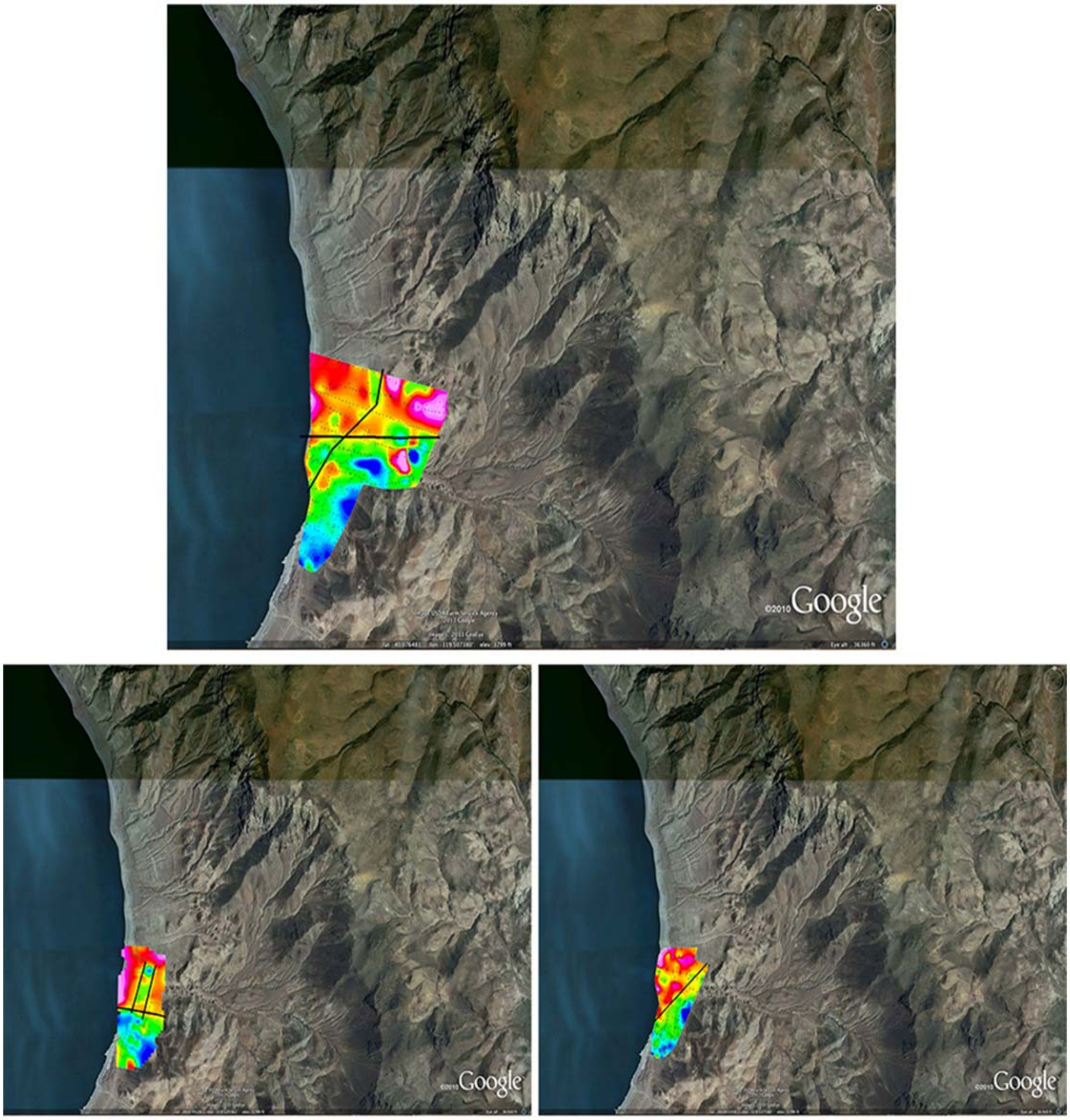

Figure 47. The three magnetic data sets with Google Earth imagery (Google Earth Pro).

ReMi conclusions include a general decreasing Vs30 value progressing toward the shoreline. This decrease in Vs30 values suggests the presence of a fault. The location of the fault is shown in Figure 48.

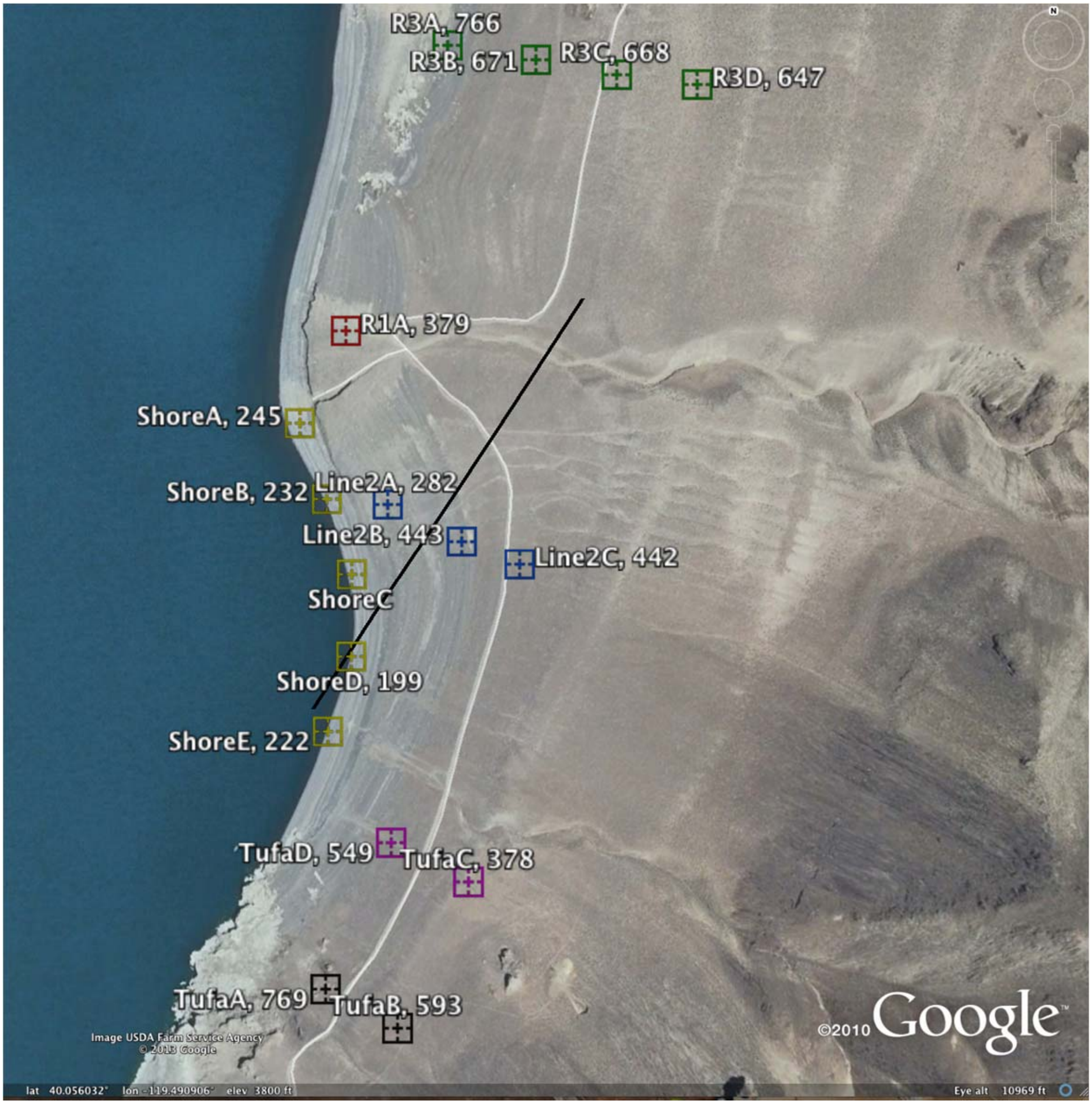

Figure 48. The location of the fault is shown in black (Google Earth Pro).

Seismic refraction indicates existence of steeply dipping structures, with prestack migration results (Figure 45) showing vertical reflectors. A low velocity section is found within the two main structures suggesting possible graben-like characteristics. The magnetic results suggest a graben at the same location. This could indicate the underlying fault splay. The refraction data with the indication of a fault is shown in Figure 49.

The seismic reflection brute stack indicates one substantial reflection that extends from 70 m to 110 m location, at 60 m to 80 m at depth. This continuous reflection is contiguous with the refraction velocities and is most likely the depth to bedrock. The refraction data overlaid on the reflection data with the indicated fault is shown in Figure 50.

COCORP Reprocessing

In the mid-1980s the NSF-supported Consortium for Continental Reflection Profiling (COCORP), run out of Cornell University, conducted large-scale deep-crustal reflection profiling across the south end of the Pyramid Lake Paiute Reservation. This survey is known as COCORP Nevada Line 8 (NV08). Figure 51 here shows the map of the survey published by Kneupfer *et al.* (1987), as their Figure 2. Line 8's survey route crossed the Truckee River 2.40 km northwest of Nixon, Nevada at vibrator point (VP) number 1045, at 39.8453° North latitude and 119.3809° West longitude (NAD27 datum).

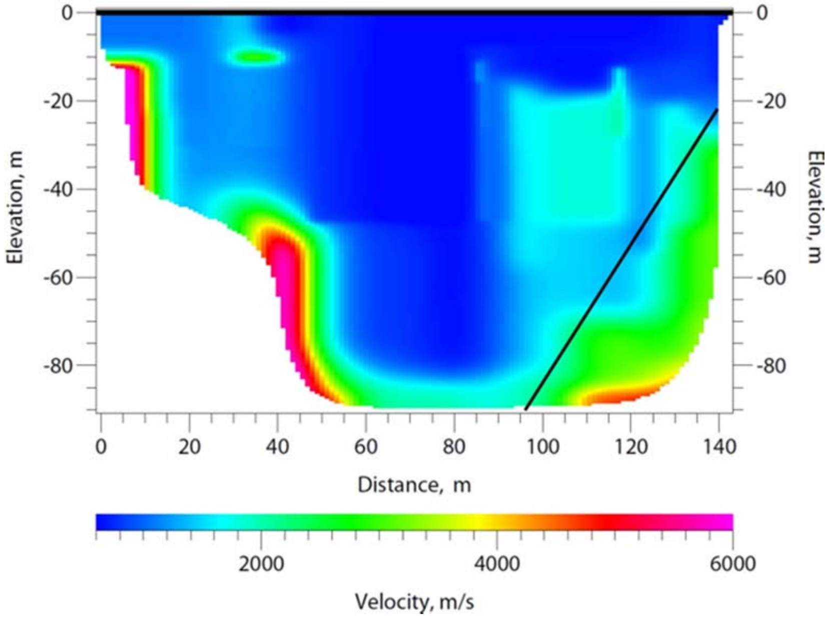

Figure 49. Seismic refraction velocity results from SeisOpt® @2D™ optimization of first-arrival times, with the indication of a fault on the east edge of a low-velocity zone (blue) to 80 m depth. The west-dipping fault, part of the Lake Range normal-fault system, is suggested by the black line. This section is north-looking, with west-northwest on the left and east-southeast on the right.

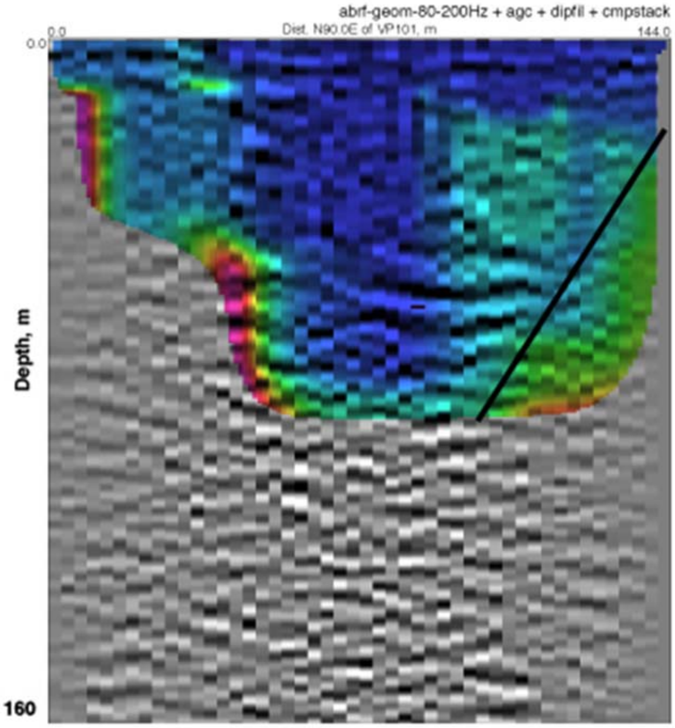

Figure 50. The colored refraction velocities overlain on the reflection brute stack. The west-dipping fault, part of the Lake Range normal-fault system, is suggested by the black line. This section is north-looking, with west-northwest on the left and east-southeast on the right.

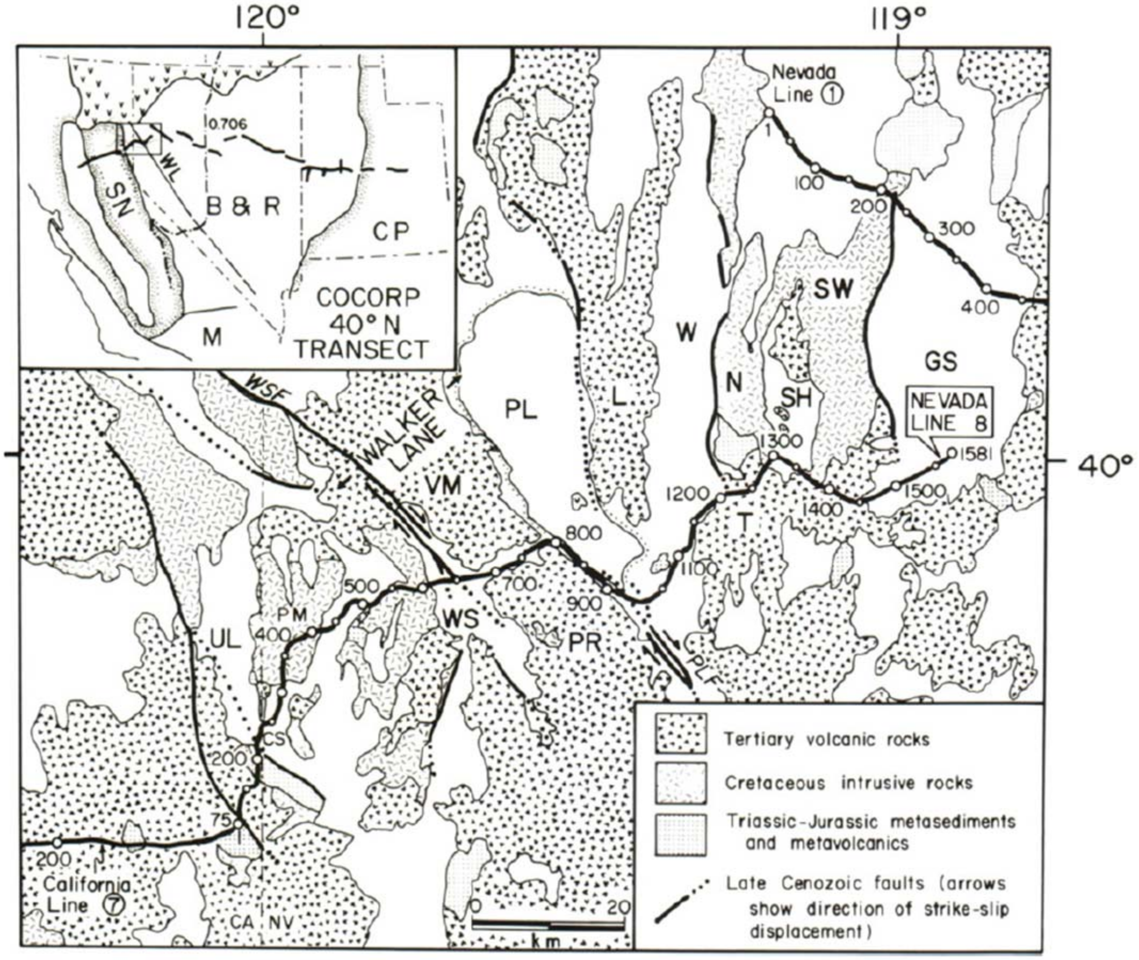

Figure 1. Generalized geologic map of the vicinity of Nevada Line 8, modified from Jennings (1977) and Stewart and Carlson (1978). Inset shows regional physiographic/tectonic provinces (SN, Sierra Nevada; B&R, Basin and Range; CP, Colorado Plateau; M, Mojave; WL, Walker Lane) and 0.706 Sr isotope ratio isopleth modified from Kistler and Peterman (1973). Faults of the Walker Lane are indicated by WSF (Warm Springs fault) and PLF (Pyramid Lake fault). UL, Upper Long Valley; CS, Cold Spring Valley; PM, Peterson Mountain; WS, Warm Springs Valley; VM, Virginia Mts.; PR, Pah Rah Range; PL, Pyramid Lake; L, Lake Range; W, Winnemucca Lake Valley; N, Nightingale Mts.; T, Truckee Range; SH, Sage Hen Valley; SW, Shawave Mts.; GS, Granite Springs Valley.

Figure 51. Map published as Figure 2 of Kneupfer *et al.* (1987) showing the route of the COCORP NV-8 deep-crustal reflection survey.

Kneupfer *et al.* (1987) and the COCORP program were focused on the deep crust, and did not process or display their results for optimal interpretation of structures or stratigraphy at the 1-2-km depth of geothermal reservoirs in this region. The Mohorovičić discontinuity (Moho) at the base of the crust is at a depth of about 35 km in this region (Louie *et al.*, 2004), which corresponds to a two-way vertical travel time of 10-12 seconds for P-wave reflections. The large source-receiver distances, up to 10 km, and large times emphasized by Kneupfer *et al.* (1987) in their acquisition and processing left the upper 1-2 seconds of two-way travel time, and upper 2 km of the sections, poorly sampled (figure 3).

The deep-crustal results of Kneupfer *et al.* (1987) do address the regional roots of fault systems and geothermal resources broadly across northeastern California and northwestern Nevada. They proposed west-dipping normal fault systems, cutting the upper crust and perhaps the entire crust, below the eastern Sierra Nevada and the Walker Lane. Kneupfer *et al.* (1987) proposed that, at shallower depths below Nixon, they imaged a steeply east-dipping normal fault from the surface at the Pyramid Lake fault zone to 4 seconds two-way time (B by 1008 in their figure 3, figure 52 here). As well, they proposed these east-dipping reflections terminate against a southwest-dipping basin-bounding fault on the west side of Black Warrior Peak (P in figure 3).

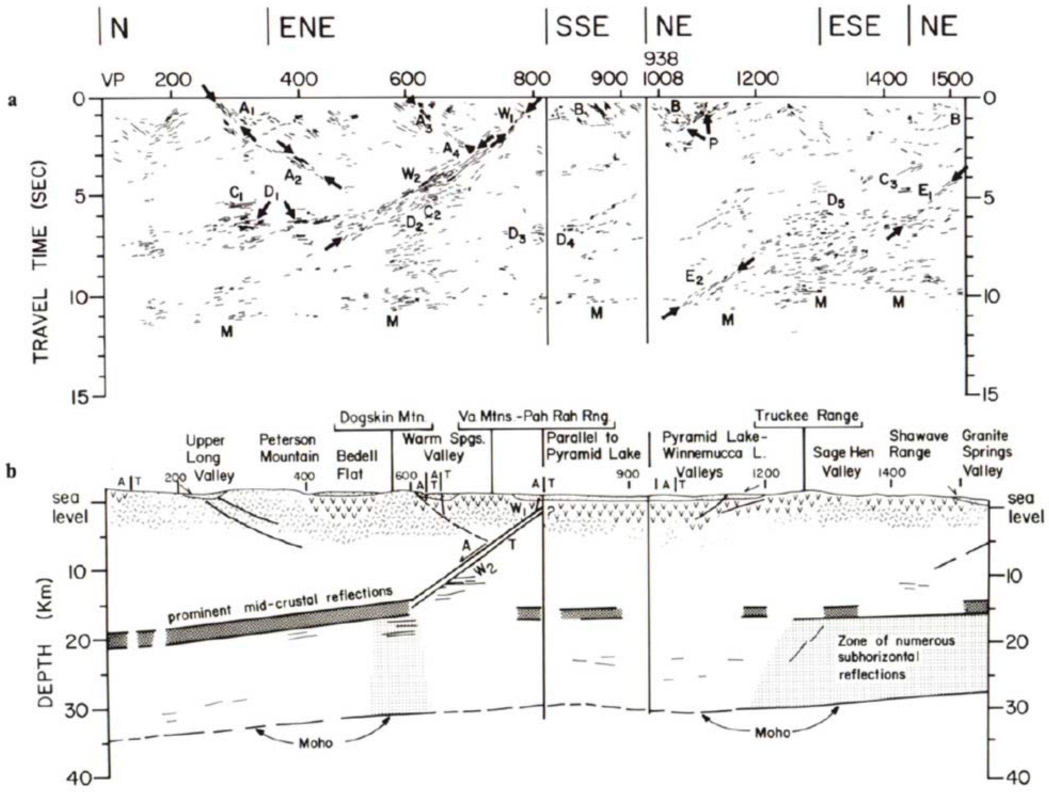

Figure 2. a. Line drawing from unmigrated stacked data of COCORP Nevada Line 8. Letters refer to features discussed in text. Scale is 1:1 at 6 km/s. b. Interpretive cross section of Nevada Line 8, based on migrated line drawings and migrated stacked data. Heavy stipple pattern shows extent of prominent mid-crustal reflections; light stipple indicates zones of numerous subhorizontal reflections. Inferred locations of Tertiary volcanics and Sierran batholithic rocks shown diagrammatically in upper part of section. Positions of major mapped surface faults shown; for strike-slip faults, T indicates side moving toward viewer. H:V = 1:1.

Figure 52. Sections published as Figure 3 of Kneupfer *et al.* (1987). Nixon lies near the "B" in the upper section just northeast of VP1008.

In their gravity analysis and inversion for the entire Basin and Range, Saltus and Jachens (1995) mapped a small sedimentary basin below Nixon, just south of the pre-Tertiary bedrock of Marble Bluff ("N" in figure 4). The gravity results suggested that this basin could be as deep as 1.5 to 2 kilometers, with relatively steep walls. It may not be elongated north to south as the Truckee River valley is; instead it appears to be roughly circular in plan.

Figure 53. Portion of basin-thickness contour map developed from gravity inversion by Saltus and Jachens (1995). The red "N" shows the location of Nixon. Dark contours are basin thickness at 0.5-km intervals; light contours are generalized elevation at 0.25 km intervals. Blue areas are basement rocks; orange areas are outcrops of Neogene volcanic basin fill; very light yellow areas are Neogene sedimentary basin fill.

Our reprocessing at the University of Nevada, Reno began with the same correlated vibrator seismic field records that Kneupfer *et al.* (1987) processed. We obtained these in 2005 from a hidden web site at Cornell University. These public data have since been moved to a national database, but their destination has not been well documented. We keyed in by hand hundreds of pages of surveyors' and observers' reports, needed to define the geometry of the seismic records. Our Nixon segment of the survey begins within the Pyramid Lake fault zone west of Nixon, at VP1008 located 39.8311° North latitude 119.4152 West longitude, and proceeds 13 km generally toward the northwest.

After entering the geometry, the major task to reprocess COCORP NV08 was to hand-pick first-arrival travel times from hundreds of 96-trace reflection records. S. Pullammanappallil at Optim employed their SeisOpt® @2D™ technology to optimize the travel times into velocity sections, based on the work of Pullammanappallil and Louie (1994). Given the large maximum source-receiver distance of 10 km, these first-arrival times provided velocity control at Nixon to within high-velocity basement at more than 2 km depth.

Figure 54 shows the resulting velocity section for the Nixon segment, plotted atop a simple stacked reflection section from the same COCORP NV08 records. The stack has been roughly depth converted, based on average stacking velocities. Strong reflections line up with the transition to higher bedrock velocities 1.5 km below the Truckee River, in figure 5. Faults A, C, and C are interpreted by connecting diffraction tops, and linking terminations of sub-horizontal reflections. Fault D is interpreted to be the sideswiped image of the fault bounding the southeast side of Marble Bluff, with very low apparent dip since the survey path was almost parallel to the fault. This fault was thus drawn along reflections, and following a basement rise of higher velocities.

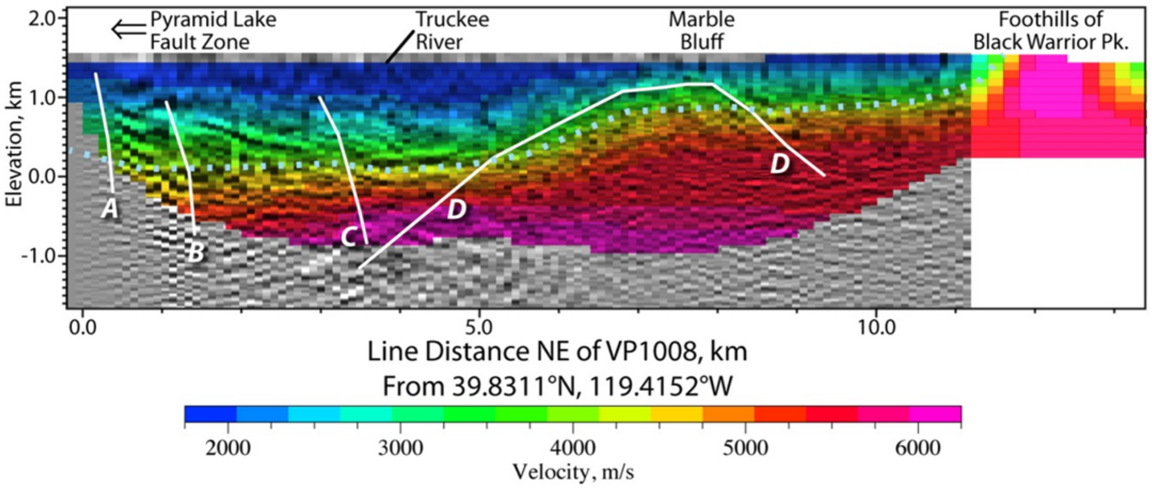

Figure 54. Composite interpreted section showing reprocessing results for the Nixon basin, with approximately no vertical exaggeration. A stacked reflectivity section is in grayscale, overlain by SeisOpt® P-velocity results in color. The dotted blue line follows the transition to high-velocity basement. White lines interpret faults, labeled for discussion.

The southwest end of this segment of NV08, at VP1008, may be within the northwest-trending Pyramid Lake strike-slip fault zone. The interpreted faults A, B, and C in figure 54 were given steep northeast dips, but an alternative interpretation of steep southwest dips is also possible from these results. The northeast dips would fit a model of the 1.5-km depths of the Nixon basin developing from a releasing left bend of the Pyramid Lake fault. The strong reflector, probably the top of Tertiary volcanics as is common in this region, is cut and offset by faults A, B, and C. The reflector has increasingly northwest dip toward west, perhaps suggesting that these faults have southwest dips.

The edge of the Marble Bluff pre-Tertiary bedrock block, interpreted as fault D in figure 54, is drawn as terminating fault C. This hypothesis is an interpretation that fault D follows the weak southwest-dipping reflections below the end of fault C. These results could alternatively be interpreted with fault C terminating fault D.

The most robust parts of these results are the Nixon basin thicknesses (dotted blue line in figure 54), and the geometry of the strong basin-bottom reflector, with its increasing northeast dip, as it continues to the southwest into the Pyramid Lake fault zone. The basin floor is certainly cut by several faults, and the lateral terminations of the strong reflector locate those faults at 1 to 1.5 km depth in the basin. It is these terminations, and these cuts, that could suggest where geothermal reservoirs may be located near Nixon.

Future work should include further prestack depth migration of the Nixon segment, to image faults A, B, C, and D as fault-plane reflectors. As well, 3d prestack migration within the Pyramid Lake fault zone that includes records from stations west of VP1008 could elucidate the structure of this major fault zone. A new, higher resolution 2d seismic-reflection survey should be conducted on a straight northeast-trending line through Nixon. This survey would cross the center of the Nixon basin, rather than skirting around the edge of the basin as COCORP NV08 does. A new survey is warranted, given the discovery in this reprocessing of the faults cutting the basin floor.

CONCLUSIONS

- The $^{3}He/^{4}He$ ratios indicate that approximately 3 percent of the helium in the APS-3 sample is derived from the mantle. The implication is that the geothermal reservoir at Astor Pass may be heated by this same small percent of mantle derived heat, but that most of the heat is derived by deep circulating groundwater not in contact with any mantle-derived fluids, as are most of the geothermal systems in the Great Basin.
- Carbon-14 age dating suggests that fluid within the Astor Pass reservoir consists of relatively “young” water that is approximately 1,500 years old.
- Stable isotope data of hydrogen and oxygen suggest that reservoir fluids are vertically well mixed in the Astor Pass area.

- Although the geothermometry yield inconsistent results, all indications are that the reservoir temperature in the Astor Pass area is less than 115°C.
- Under both normal faulting and strike-slip faulting stress regimes, the north-striking, near-vertical fault segments on the Pyramid Lake Paiute Reservation have the highest dilation tendency.
- A three-dimensional geologic model for Astor Pass was built using the EarthVision software package. The geologic model consists of 19 fault planes and 16 stratigraphic units. The Astor Pass graben is bounded by steeply west-dipping, anastomosing normal faults on the east side and one steeply east-dipping normal fault on the west side. A steeply northeast-dipping dextral-normal fault zone and a steeply west-dipping normal fault zone intersect on the surface near the Pleistocene tufa deposits that serve as the primary structural control of the Astor Pass geothermal system. Fluid up-flow from depth is likely focused within these two fault intersection zones beneath the Pleistocene tufa deposits. This fluid flow is accommodated by fault controlled fracture permeability in the Mesozoic basement, where primarily lithologic permeability is very low. These fluids flow out into the highly interconnected, transmissive reservoir in the middle Miocene volcanic rocks. In addition to outflow into the Tertiary section, fluid upflow continues along these discrete fault intersections into the shallow subsurface, as evidenced by the concentrated shallow temperature anomaly in the vicinity of the Pleistocene tufa deposits.
- Results of the wells testing suggest that the reservoir (middle Miocene volcanic rocks) permeabilities are relatively large with maximum permeability in the vertical direction (6×10^{-12} m^2) and significantly less in the horizontal direction (3×10^{-14} m^2).
- The net energy production at the Astor Pass site could approach 1.8 MW assuming a sustained extraction-injection rate of 90 kg/s (1500 gpm).
- Shallow temperature measurements in the Emerson Pass area yielded a maximum 2 m soil temperature of ~83^{o}C (182F), which was found on the east side of the valley and delineated a shallow high temperature anomaly in an oblong shape at the base of the eastern hills.
- Exploration data in the Emerson Pass area suggests a favorable geothermal setting. The 2-m temperature surveys defined a north-south elongate thermal anomaly that resides on a north- to north-northeast-striking normal fault. Additionally, travertine mounds, chalcedonic silica veins, and silica cemented Pleistocene lacustrine gravels in the Emerson Pass area were discovered through the mapping and indicate a robust geothermal system active at the surface in the recent past, likely the early Holocene. Structural complexity and spatial heterogeneities of the strain and stress field have developed in the step-over region, but kinematic data suggest a west-northwest-trending (~280° azimuth) extension direction. The Emerson Pass geothermal system likely results from enhanced permeability generated by the intersection of two oppositely dipping, southward terminating north- to north-northwest-striking (Fox Range fault) and north-

northeast-striking normal faults. Three shallow temperature gradient wells have been drilled at the Emerson Pass site, with a maximum temperature of 120 ^{0}C at 250 ft bgs in EG2.

- Reservation-wide geologic mapping yielded numerous discoveries including:
    - Recognition of a large felsic volcanic center in the northeastern part of the reservation in the northern Lake Range.
    - Identification of several large landslide deposits on the eastern flank of the Lake Range and northeastern part of the Pah Rah Range; some of these landslides show evidence of recent activity.
    - Discounting the hypothesis of a major east-dipping antithetic fault zone on the east side of the Lake Range, which had been considered as a possible control of warm springs in the area; scarps in this area are primarily erosional and generally represent Lake Lahontan shorelines rather than fault scarps.
    - Recognition of several northerly striking Holocene normal faults in the southern part of the Smoke Creek Desert; these faults may connect southward with faults cutting the Terraced Hills.
    - Documenting major west-dipping, N- to NNE-striking Quaternary normal faults in the southern part of the San Emidio Desert and San Emidio Canyon; these faults link southward with the major range-front fault along the west flank of the Lake Range.
    - Identification of several previously unrecognized exposures of Mesozoic basement rocks in the northern Lake Range and southern Fox Range.
- Magnetic, refraction microtremor, and seismic refraction/reflection surveys were successful in characterizing the proposed fault structure at Anderson Bay. All three surveys performed showed data entailing the presence of steeply dipping structures and a general northeast and southwest anomaly.
- A reanalysis of the COCORP program data resulted in a revised basin thickness in the Nixon area, and a detailed geometry of the strong basin-bottom reflector, with its increasing northeast dip, as it continues to the southwest into the Pyramid Lake fault zone. The basin floor is certainly cut by several faults, and the lateral terminations of the strong reflector locate those faults at 1 to 1.5 km depth in the basin. It is these terminations, and these cuts, that could suggest where geothermal reservoirs may be located near Nixon.

REFERENCES

Anderson, M.P. and W.W. Woessner (1992) Applied groundwater modeling: simulation of flow and advective transport, Academic Press, San Diego.

Bethke, C.M., and T.M. Johnson, 2002, Ground water age, *Ground Water*, 40(4), 337-339.

Blackwell, D.D. and M. Richards (2004), Geothermal map of North America, American Association of Petroleum Geologists, 1 sheet, scale 1:6,500,000.

Clark, I., and P. Fritz, 1997, *Environmental Isotopes in Hydrogeology*, Lewis Publishers, 328 pp.

Coolbaugh, M.F., J.E. Faulds, C. Kratt, G. Oppliger, L. Shevenell, W. Calvin, W.J. Ehni, and R.E. Zehner, 2006, Geothermal potential of the Pyramid Lake Paiute Reservation, Nevada, USA: Evidence of previously unrecognized moderate-temperature (150-70°C) geothermal systems, Geothermal Resources Council *Transactions*, v. 30, 59-67.

Coolbaugh, M.F., P. Lechler, C. Sladek, and C. Kratt, 2009, Carbonate tufa columns as exploration guides for geothermal systems in the Great Basin, Geothermal Resources Council

Doherty, J. (2000) PEST – model-independent parameter estimation – user's manual, 4th Ed., Watermark Numerical Computing.

Faure, G., 1977, *Principles of Isotope Geology*, John Wiley & Sons, 464 p.

Ferguson, G., S.E. Grasby, and S.R. Hindle, 2009, What do aqueous geothermometers really tell us? *Geofluids*, v. 9, 39-48.

Fontes, J. -Ch., and J-M Garnier, 1979, Determination of the initial ^{14}C activity of total dissolved carbon: A review of existing models and a new approach, *Water Resources Research*, v. 15, 399-413.

Fournier, R.O., 1977, Chemical geothermometers and mixing models for geothermal systems, *Geothermics*, v. 5, 41-50.

Freeze, R.A. and J.A. Cherry (1979) Groundwater, Prentice Hall, Upper Saddle River, New Jersey.

Garside, L.J., and J.H. Schilling, 1979, Thermal Waters of Nevada, Bulletin 91, Nevada Bureau of Mines and Geology, 163 pp.

Harbaugh, A.W. (2005), MODFLOW-2005: the U.S. Geological Survey modular ground-water model – the Ground-Water Flow Process: U.S. Geological Survey Techniques and Methods, 6-A16.

Heberle, F. and D. Bruggemann (2010), Energy based fluid selection for a geothermal Organinic Rankine Cycle for combined heat and power generation, Applied Thermal Engineering, 30, 1326-1332.

Kennedy, B.M., and M.C. van Soest, 2006, A helium isotope perspective on the Dixie Valley, Nevada, hydrothermal system, *Geothermics*, 35, 26-43.

Mazor, E., 1991, *Applied Chemical and Isotopic Groundwater Hydrology*, Halstead Press (John Wiley & Sons), 274 pp.

Neretnieks, I., 1981, Age dating of groundwater in fissured rock: Influence of water volume in micropores, *Water Resources Research*, 17(2), 421-422.

Nitao, J.J. and Y. Sun, (2007), USNT Reference manual of the NUFT flow and transport code, Lawerence Livermore National Laboratory.

Parashar, R. and D.M. Reeves (2011), Computation of flow and transport in fracture networks on a continuum grid, Proceedings of MODFLOW and MORE 2011: Integrated Hydrologic Modeling, June 5-8, Golden, CO, 771-775.

Reeves, D.M., D.A. Benson, and M.M. Meerschaert (2008), Transport of conservative solutes in simulated fracture networks: 1. Synthetic data generation, Water Resources Research, 44, WO5401, doi:10.1029/2007WR006069.

Reeves, D.M., G. Pohll, B. Lyles, J. Faulds, J. Louie, B. Ehni, C. Kratt, C. Cooper, R. Parashar, S. Pullammanappallil, and D. Noel (2012), Geothermal resource characterization and evaluation at Astor Pass, Nevada, Geothermal Resources Council Transactions, 36, 1371-1376.

Robertson, E.C., (1988), Thermal Properties of Rocks, U.S. Geological Sruvey, Open-File Report 88-441.

Sanford, W.E., 1997, Correcting for diffusion of carbon-14 dating of ground water, *Ground Water*, 35(2), 357-361.

Siler, D., B. Mayhew, and J.E. Faulds (2012), Three-dimensional geologic characterization of geothermal systems: Astor Pass, Nevada, USA, Geothermal Resources Council Transactions, 36, 783-786.

Thorstenson, D.C., E.P. Weeks, H. Haas, E. Busenberg, L.N. Plummer, and C.A. Peters, 1998, Chemistry of unsaturated zone gases sampled in open boreholes at the crest of Yucca Mountain, Nevada: Data and basic concepts of chemical and physical processes in the mountain, *Water Resources Research*, 34(6), 1507-1529.

Anderson, R, 2013, Structural controls of the Emerson Pass Geothermal System, Washoe County, Nevada: [M.S. Thesis]: University of Nevada, Reno, 108 p.

Ferrill, D.A., Winterle, J., Wittmeyer, G., Sims, D., Colton, S. and Armstrong, A., 1999. Stressed Rock Strains Groundwater at Yucca Mountain, Nevada. GSA Today, 9(5): 1-8.

Mayhew, B., 2013. A 3D Characterization of the Astor Pass Gepthermal System, Washoe County, Nevada, University of Nevada, Reno, 110 p.

Morris, A., Ferrill, D.A. and Henderson, D.B., 1996. Slip-tendency analysis and fault reactivation. Geology (Boulder), 24(3): 275-278.

Sibson, R.H., 1994. Crustal stress, faulting and fluid flow. Geological Society, London Special Publication, 78: 69-84.

Sibson, R.H., 1996. Structural permeability of fluid-driven fault-fracture meshes. Journal of Structural Geology, 18(8): 1031-1042.

Bonham, H.F. and Papke, K.G., 1969. Geology and mineral deposits of Washoe and Story Counties, Nevada. Nevada Bureau of Mines and Geology.

Eisses, A., Kell, A., Kent, G., Driscoll, N., Karlin, R., Baskin, R., Louie, J. and Pullammanappallil, S., 2011. Marine and land active-source seismic imaging of mid-Miocene to Holocene-aged faulting near geothermal prospects at Pyramid Lake, Nevada. Geothermal Resources Council Transactions, 30: 1643-1646.

Faulds, J.E., Drakos, P., Vice, G.S., Mayhew, B. and Noel, D., 2011. The Pyramid Lake Paiute Reservation, western Nevada (USA): Exploration for blind geothermal systems in a transtensional displacement transfer zone, New Zealand Geothermal Workshop, Auckland, New Zealand.

Jolie, E., Faulds, J. and Moeck, I., 2012. The Development of a 3D Structural-Geological Model as part of the Geothermal Exploration Strategy -- A Case Study from the Brady's Geothermal System, Nevada, USA, Thirty-Seventh Workshop on Geothermal Reservoir Engineering., Stanford University, pp. 421-425.

Louie, J.N., Pullammanappallil, S.K. and Honjas, W., 2011. Advanced seismic imaging for geothermal development, New Zealand Geothermal Workshop, Auckland, New Zealand, pp. 7.

Mayhew, B., 2013. A 3D Characterization of the Astor Pass Gepthermal System, Washoe County, Nevada, University of Nevada, Reno, 110 pp.

Moeck, I., Schandelmeier, H. and Holl, H.-G., 2009. The stress regime in a Rotliegend reservoir of the Northeast German Basin. International Journal of Earth Sciences, 98(7): 1643-1654.

Reeves, D.M., Pohll, G., Lyle, B., Faulds, J., Louie, J., Kratt, C., Cooper, C., Parashar, R., Pullammanappallil, S. and Noel, D., 2012. Geothermal Resource Characterization and Evaluation at Astor Pass, Nevada. Geothermal Resource Council Transactions, 36: 1371-1376.

Siler, D.L., Mayhew, B. and Faulds, J.E., 2012. Three-Dimensional Geologic Characterization of Geothermal Systems: Astor Pass, Nevada, USA Geothermal Resource Council Transactions, 36: 783-786.

Vice, G.S., 2008. Structural controls of the Astor-Pass-Terraced Hills geothermal system in a region of strain transfer in the western Great Basin, northwestern Nevada, University of Nevada, Reno, 125 pp.

Vice, G.S., Faulds, J.E., Ehni, W.J. and Coolbaugh, M.F., 2007. Structural controls of a blind geothermal system in the northern Pyramid Lake area, northwestern Nevada. Geothermal Resource Council Transactions, 31: 133-137.

Anderson, R.B., 2013, Structural controls of the Emerson Pass geothermal system, Washoe County, Nevada [M.S. thesis]: University of Nevada, Reno, 100 p.

Anderson, R.B. and Faulds, J.E., 2013. Structural Controls of the Emerson Pass Geothermal System, Washoe County, Nevada: Geothermal Resources Council Transactions, v. 37, p. 453-458.

Anderson, R.B., Faulds, J.E., and Dering, G.M., 2013, Preliminary geologic map of the central Lake Range, southern Fox Range, and northern Terraced Hills, Emerson Pass geothermal area, Washoe County, Nevada: Nevada Bureau of Mines and Geology Open-File Report 13-10, 9 p. text.

Bell, J. W., House, P. K., and Briggs, R. W., 2003a, Preliminary geologic map of the west half of the Nixon Quadrangle, Washoe County, Nevada: Nevada Bureau of Mines and Geology Open-File Report 03-21.

Bell, J. W., Garside, L. J., and House, P. K., 2003b, Preliminary geologic map of the Wadsworth Quadrangle, Storey and Washoe County, Nevada: Nevada Bureau of Mines and Geology Open-File Report 03-28.

Bell, J. W., House, P. K., and Briggs, R. W., 2004, Preliminary geologic map of the east half of the Pah Rah Mountain Quadrangle, Washoe County, Nevada: Nevada Bureau of Mines and Geology Open-File Report 04-3.

Delwiche, B.M., 2007, Oligocene paleotopography and structural evolution of the Pah Rah Range, western Nevada: Implications for constraining slip on the right-lateral Warm Springs Valley fault in the northern Walker Lane [M.S. thesis]: University of Nevada, Reno, 126 p.

Drakos, P.S., 2007, Tertiary stratigraphy and structure of the southern Lake Range, northwest Nevada: Assessment of kinematic links between strike-slip and normal faults in the northern Walker Lane [M.S. thesis]: University of Nevada, Reno, 165 p.

Drakos, P.S., and Faulds, J.E., Preliminary geologic map of the southern Lake Range, Washoe County, Nevada: Nevada Bureau of Mines and Geology Open-File Report Open-File Report 13-11, 5 p. text.

Faulds, J.E., Henry, C.D., and dePolo, C.M., 2003, Preliminary geologic map of the Tule Peak Quadrangle, Washoe County, Nevada: Nevada Bureau of Mines and Geology Open-File Report 03-10.

Faulds, J.E., and Ramelli, A.R., 2005, Preliminary geologic map of the Fernley East Quadrangle, Lyon and Washoe Counties, Nevada: Nevada Bureau of Mines and Geology Open-File Report 05-9, scale 1:24,000.

Faulds, J.E., dePolo, C.M., and Henry, C.D., 2007, Preliminary geologic map of the Sutcliffe Quadrangle, Washoe County, Nevada: Nevada Bureau of Mines and Geology Open-File Report 03-17, 1:24,000.

Faulds, J.E., Ramelli, A.R., and Henry, C.D., 2008, Preliminary geologic map of the Fernley West Quadrangle, Lyon, Storey, and Washoe Counties, Nevada: Nevada Bureau of Mines and Geology Open-File Report 08-04, scale 1:24,000.

Faulds, J., Drakos, P., Vice, G., Mayhew, B., and Noel, D., 2011, The Pyramid Lake Paiute Reservation, western Nevada (USA): Exploration for blind geothermal systems in a transtensional displacement transfer zone: New Zealand Geothermal Workshop 2011 Proceedings, 21-23 November 2011, Auckland, New Zealand, 5 p.

Faulds, J.E., Anderson, R.B., Ramelli, A.R., Drakos, P.S., Vice, G.S., Hinz, N.H., Dering, G.M., Bell, J.W., House, P.K., and Ressel, M.W., 2013, Preliminary geologic map of the Pyramid Lake Paiute Reservation, Lyon, Pershing, Storey, and Washoe Counties, Nevada: Nevada Bureau of Mines and Geology unpublished map.

Garside, L. J., Castor, S. B., and dePolo, C.M., 2003, Geology of the Fraser Flat Quadrangle and the west half of the Moses Rock Quadrangle, Washoe County, Nevada: Nevada Bureau of Mines and Geology Map 146.

Mayhew, B, A., 2013, A 3D characterization of the Astor Pass geothermal system, Washoe County, Nevada [M.S. thesis]: University of Nevada, Reno, 102 p.

Ressel, M. W., 1996, A Transitional Basaltic Center in West-Central Nevada: Petrochemistry and Constraints on Regional Middle Miocene Magmatism and Tectonism [M.S. thesis]: University Nevada, Reno.

Vice, G.S., 2008, Structural controls of the Astor-Pass-Terraced Hills geothermal system in a region of strain transfer in the western Great Basin, northwestern Nevada [M.S. thesis]: University of Nevada, Reno, 125 p.

Briggs, R.W., and Wesnousky, S.G., 2004 R.W. Briggs and S.G. Wesnousky, Late Pleistocene fault slip rate, earthquake recurrence, and recency slip along the Pyramid Lake fault zone, northern Walker Lane, United States, *Journal of Geophysical Research* 109 (2004), p. 16.

Eisses, A., Kell, A., Graham, K., Driscoll, N., Baskin, R., Smith, K., Karlin, R., Louie, J., and Pullammanappallil, S., 2012, New Constraints on Slip Rates, Recurrence Intervals, and Strain Partitioning Beneath Pyramid Lake, Nevada. University of Nevada, [M.S. Thesis]: University of Nevada, Reno.

Louie, John N., 2001, Faster, better: shear-wave velocity to 100 meters depth from refraction microtremor arrays: Bull. Seismol. Soc. Amer., 91, no. 2 (April), 347-364. http://crack.seismo.unr.edu/ftp/pub/louie/papers/disper/refr.html

Scott, J. B., M. Clark, T. Rennie, A. Pancha, H. Park and J. N. Louie, 2004, A shallow shear-wave velocity transect across the Reno, Nevada area basin: Bull. Seismol. Soc. Amer., 94, no. 6 (Dec.), 2222-2228. http://crack.seismo.unr.edu/hazsurv/renoprof/renoprof.html

Knuepfer, P. L. K., Lemiszki, P. J., Hauge, T. A., Brown, L. D., Kaufman, S., and Oliver, J. E., 1987, Crustal structure of the Basin and Range-Sierra Nevada transition from COCORP deep seismic-reflection profiling: *Geological Society of America Bulletin*, **98**, 488-498.

Louie, John N., Weston Thelen, Shane B. Smith, Jim B. Scott, Matthew Clark, and Satish Pullammanappallil, 2004, The northern Walker Lane refraction experiment: Pn arrivals and the northern Sierra Nevada root: *Tectonophysics*, **388**, 253-269.

Pullammanappallil, S. K., and Louie, J. N., 1994, A generalized simulated-annealing optimization for inversion of first-arrival times: *Bulletin of the Seismological Society of America*, **84**, 1397-1409.